UNIVERSITÀ DEGLI STUDI DI PADOVA

Dipartimento di Fisica e Astronomia "Galileo Galilei"
Scuola di dottorato di ricerca in Astronomia
Ciclo XXV

Predictions for imaging and spectroscopic surveys of galaxies and Active Galactic Nuclei in the mid-/far-Infrared

Direttore della Scuola:	Ch.mo Prof. Giampaolo Piotto
Supervisori:	Prof. Gianfranco De Zotti Dr. Mattia Negrello Prof. Piero Benvenuti
Dottorando:	Matteo Bonato

Padova, 29 Gennaio 2015

To my little crying angel Aurora

Abstract

While continuum imaging data at far-infrared to sub-millimeter wavelengths have provided tight constraints on the population properties of dusty star-forming galaxies up to high redshifts, future space missions like the Space Infra-Red Telescope for Cosmology and Astrophysics (SPICA) and ground based facilities like the Atacama Large Millimeter/submillimeter Array (ALMA) and the Cerro Chajnantor Atacama Telescope (CCAT) will allow detailed investigations of their physical properties via their mid-/far-infrared line emission.

The goal of this thesis project was to carry out predictions for these spectroscopic surveys using both a phenomenological approach and physically grounded models. These predictions are useful to optimize the planning of the surveys.

In the first part of the work, I present updated predictions for the number counts and the redshift distributions of star-forming galaxies spectroscopically detectable by these future missions. These predictions exploit a recent upgrade of evolutionary models, that includes the effect of strong gravitational lensing, in the light of the most recent *Herschel* and South Pole Telescope (SPT) data. Moreover the relations between line and continuum infrared luminosity are re-assessed, considering also differences among source populations, with the support of extensive simulations that take into account dust obscuration. My reference model for the redshift dependent IR luminosity functions is the one worked out by Cai et al. (2013) based on a comprehensive hybrid approach combining a physical model for the progenitors of early-type galaxies with a phenomenological one for late-type galaxies. The derived line luminosity functions are found to be highly sensitive to the spread of the line to continuum luminosity ratios. Estimates of the expected numbers of detections per spectral line by the SpicA FAR infrared Instrument (SAFARI) and by CCAT surveys for different integration times per field of view at fixed total observing time are presented. Comparing with the earlier estimates by Spinoglio et al. (2012), I find, in the case of SPICA-SAFARI, differences within a factor of two in most cases, but occasionally much larger. More substantial differences are found for CCAT.

Thereafter I present new estimates of redshift-dependent luminosity functions of IR lines detectable by SPICA-SAFARI and excited both by star formation and by AGN activity. The new estimates improve over previous work by dealing in a self consistent way with the emission of galaxies as a whole, including both the starburst and the AGN component. While the galaxy–AGN co-evolution was already worked out by Cai et al. (2013) in the case of proto-spheroidal galaxies, the evolution of late-type galaxies was dealt with independently of that of AGNs associated with them. I upgraded the model to enable it to take into account in a coherent way the contributions of both starbursts and AGNs to the IR emission during the cosmic evolution also of late-type galaxies.

New relationships between line and AGN bolometric luminosity have been derived and those between line and IR luminosities of the starburst component have been updated. These ingredients were used to work out predictions for the source counts in 11 mid/far-IR emission lines partially or entirely excited by AGN activity. I find that the statistics of the emission line detection of galaxies as a whole is mainly determined by the star formation rate, because of the rarity of bright AGNs. I also find that the slope of the line integral number counts is flatter than 2 implying that the number of detections at fixed observing

time increases more by extending the survey area than by going deeper. I thus propose a spectroscopic survey of 1 hour integration per field-of-view over an area of 5 deg^2 to detect (at 5σ) $\sim$760 AGNs in [OIV]25.89μm – the brightest AGN mid-infrared line – out to $z \sim 2$. Pointed observations of strongly lensed or hyper-luminous galaxies previously detected by large area surveys such as those by *Herschel* and by SPT can provide key information on the galaxy-AGN co-evolution out to higher redshifts.

Finally, as third step of the work, I present predictions for number counts and redshift distributions of galaxies detectable in continuum and in emission lines with the Mid-infrared (MIR) Instrument (SMI) proposed for SPICA. I have considered 24 MIR emission fine-structure lines, four Polycyclic Aromatic Hydrocarbon (PAH) bands (at 6.2, 7.7, 8.6 and 11.3μm) and two silicate bands (in emission and in absorption) at 9.7μm and 18.0μm. Six of these lines are primarily associated with Active Galactic Nuclei (AGNs), the others primarily with star formation. Altogether, they allow us to study the interplay between star formation and super-massive black hole growth. A survey with the SMI spectrometers of 1 hour integration per field-of-view (FoV) over an area of 1 deg^2 will yield $5\,\sigma$ detections of $\simeq 140$ AGN lines, produced by $\simeq 110$ AGNs[1], and of $\simeq 5.2 \times 10^4$ star-forming galaxies, $\simeq 1.6 \times 10^4$ of which will be detected in at least two lines. The combination of a shallow (20.0 deg^2, 1.4×10^{-1} h integration per FoV) and a deep survey ($6.9 \times 10^{-3}\,\mathrm{deg}^2$, 635 h integration time), with the SMI camera, for a total of $\sim$1000 h, will accurately determine the MIR number counts of galaxies and of AGNs over five orders of magnitude in flux density, reaching values more than one order of magnitude fainter than the *Spitzer* 24 μm surveys. This will allow us to resolve almost completely the extragalactic background and to determine the cosmic star formation rate (SFR) function down to SFRs more than 100 times fainter than reached by the *Herschel* Observatory.

---

[1] the difference between the last two numbers is due to the fact that some sources are detectable simultaneously in multiple lines

These spectroscopic observations will allow us to probe all phases of the interstellar medium (ionized, atomic and molecular). Measurements of these lines will provide redshifts and key insight on physical conditions of dust obscured regions and on the energy sources controlling their temperature and pressure. This information is critically important for investigating the complex physics ruling the dust-enshrouded active star-forming phase of galaxy evolution and the relationship with nuclear activity. Observations of strongly gravitationally lensed galaxies will be of special interest, because strong lensing allows us to measure the gas/dust distribution in galaxies up to high-z and to gain information on sources too faint to be detected with current instrument sensitivities, thus testing models for galaxy formation and dark matter.

Riassunto

Mentre i dati fotometrici sulla luminosità del continuo, alle lunghezze d'onda che vanno dal lontano infrarosso al sub-millimetrico, hanno fornito vincoli stringenti sulle proprietà delle popolazioni di galassie polverose con alti tassi di formazione stellare fino a redshift elevati, future missioni spaziali, come lo *Space Infra-Red Telescope for Cosmology and Astrophysics* (SPICA) e telescopi da terra come l'*Atacama Large Millimeter/submillimeter Array* (ALMA) e il *Cerro Chajnantor Atacama Telescope* (CCAT), consentiranno indagini dettagliate sulle loro proprietà fisiche, tramite l'analisi della loro emissione in riga nel medio/lontano infrarosso.

L'obiettivo di questa tesi è stato di realizzare predizioni per queste indagini spettroscopiche, utilizzando sia un approccio fenomenologico che modelli fisici. Queste predizioni risultano particolarmente utili per ottimizzare la pianificazione delle *survey.*

Nella prima parte del lavoro, presento predizioni aggiornate per i conteggi e le distribuzioni in redshift di galassie con alti tassi di formazione stellare, rilevabili spettroscopicamente da queste future missioni. Queste predizioni si servono dei recenti aggiornamenti dei modelli evolutivi, che includono l'effetto di lente gravitazionale forte, alla luce dei più recenti dati di *Herschel* e del *South Pole Telescope* (SPT). Inoltre le relazioni tra la luminosità in riga e quella del continuo infrarosso sono state ricalcolate, considerando anche

differenze tra le popolazioni di sorgenti, con il supporto di estese simulazioni che tengono conto dell'oscuramento da polveri. Il mio modello di riferimento per le funzioni di luminosità IR dipendenti dal redshift è stato quello elaborato da Cai et al. (2013), basato su un esaustivo approccio ibrido, che combina un modello fisico per i progenitori delle galassie *early-type* con uno fenomenologico per le galassie *late-type.* Le funzioni di luminosità in riga derivate sono risultate essere molto sensibili alla dispersione dei rapporti tra la luminosità in riga e quella del continuo. Vengono presentate stime del numero atteso di detezioni per riga spettrale rilevabili da *survey* con lo *SpicA FAR infrared Instrument* (SAFARI) e con CCAT, per diversi tempi di integrazione per campo di vista, con un tempo totale di osservazione fissato. Confrontando queste stime con altre calcolate precedentemente da Spinoglio et al. (2012), ho trovato, nel caso di SPICA-SAFARI, nella maggior parte dei casi differenze all'interno di un fattore due, ma a volte molto maggiori. Per CCAT sono state trovate differenze più sostanziali.

Inoltre presento nuove stime di funzioni di luminosità in riga dipendenti dal redshift, per righe IR rilevabili da SPICA-SAFARI ed eccitate da attività sia di formazione stellare sia di AGN. Le nuove stime sono più accurate rispetto alle precedenti, poichè trattano in modo autoconsistente l'emissione complessiva delle galassie, comprendendo sia la componente *starburst* sia quella AGN. Mentre la coevoluzione galassia-AGN, nel caso delle galassie proto-sferoidali, era stata già elaborata da Cai et al. (2013), l'evoluzione delle galassie *late-type* veniva lì trattata in modo indipendente da quella degli AGN ad esse associati. Ho aggiornato il modello per far sì che trattasse in modo coerente i contributi all'emissione IR sia degli *starburst* che degli AGN, durante la loro evoluzione cosmica, anche per le galassie *late-type.*

Sono state ricavate nuove relazioni tra la luminosità in riga e la luminosità bolometrica dell'AGN e sono state aggiornate quelle tra la luminosità in riga e la luminosità IR della componente *starburst.* Questi ingredienti sono stati utilizzati per realizzare predizioni per i conteggi in 11 righe di emissione nel medio/lontano IR, parzialmente o interamente eccitate dall'attività di AGN. Ho trovato che la statistica delle detezioni nelle righe di emissione delle galassie (considerate nel loro complesso, cioè *starburst*+AGN) è determinata principalmente dal tasso di formazione stellare, a causa della rarità di AGN luminosi. Ho trovato anche che la pendenza dei conteggi integrali in riga è minore di 2, il che implica che il numero di detezioni, ad un tempo di osservazione totale fissato, aumenta maggiormente estendendo l'area della *survey* che andando più in profondità. Ho quindi proposto una *survey* spettroscopica di 1 h di tempo di integrazione per campo di vista, su un'area di 5 deg^2, per rilevare (a 5σ) $\sim$760 AGN nell'[OIV]25.89μm − la riga da AGN più brillante nel medio IR − fino a $z \sim 2$. Osservazioni puntate di galassie fortemente lensate o di galassie iper-luminose precedentemente rilevate da *survey* a grande area, come quelle realizzate con *Herschel* e con SPT, possono fornire informazioni chiave sulla coevoluzione galassia-AGN fino a redshift più elevati.

Infine, come terza pate del lavoro, presento predizioni per conteggi e distribuzioni in redshift di galassie rilevabili nel continuo e in righe di emissione dal *Mid-infrared* (MIR) *Instrument* (SMI) proposto per SPICA. Ho considerato 24 righe MIR di emissione, quattro bande di idrocarburi policiclici aromatici (PAH) (a 6.2, 7.7, 8.6 e 11.3μm) e due bande di silicati (in emissione e in assorbimento) a 9.7μm e a 18.0μm. Sei di queste righe sono associate principalmente ad AGN, le altre soprattutto alla formazione stellare. Complessivamente, ci permettono di studiare l'interazione tra la formazione stellare e l'accrescimento del buco nero super-massiccio. Una *survey* con gli spettrometri SMI di 1 h di tempo di integrazione per campo di vista, su un'area di 1 deg^2, permetterà la detezione (a $5\,\sigma$) di $\simeq 140$ righe AGN, prodotte da $\simeq 110$ AGN[2], e di $\simeq 5.2 \times 10^4$ galassie con alto tasso di formazione stellare, $\simeq 1.6 \times 10^4$ delle quali verranno rilevate in almeno due righe. La combinazione

---

[2] la differenza tra gli ultimi due numeri è dovuta al fatto che alcune sorgenti sono rilevabili contemporaneamente in più righe

di una *survey* superficiale (20.0 deg^2, 1.4×10^{-1} h di tempo di integrazione per campo di vista) e una *survey* profonda (6.9×10^{-3} deg^2, 635 h di tempo di integrazione per campo di vista), con la camera dello SMI, per un totale di ~ 1000 h, determinarà accuratamente i conteggi MIR di galassie e di AGN per oltre cinque ordini di grandezza in densità di flusso, raggiungendo valori più di un ordine di grandezza più deboli delle *survey Spitzer* a 24 μm. Questo ci permetterà di risolvere quasi completamente il fondo extragalattico e di determinare la funzione del tasso di formazione stellare cosmica fino a tassi di formazione stellare più di 100 volte più piccoli di quanto è possibile con *Herschel*.

Queste osservazioni spettroscopiche ci permetteranno di indagare tutte le fasi del mezzo interstellare (ionizzato, atomico e molecolare). Le misurazioni di queste righe forniranno redshift e importanti indicazioni sulle condizioni fisiche delle regioni oscurate da polveri e sulle sorgenti energetiche che controllano la loro temperatura e pressione. Queste informazioni sono di fondamentale importanza per lo studio dei complessi processi fisici che regolano la fase polverosa di attiva formazione stellare di evoluzione delle galassie e le relazioni con l'attività nucleare. Le osservazioni di galassie fortemente lensate saranno di particolare interesse, perchè ci permetteranno di misurare la distribuzione di gas/polvere in galassie fino ad alti z e di ottenere informazioni su sorgenti troppo deboli per essere rilevate con le sensibilità degli strumenti attuali, testando perció i modelli di formazione delle galassie e di materia oscura.

Publications

Most of the results presented in this Thesis are contained in the following papers:

- 'Exploring the early dust-obscured phase of galaxy formation with blind mid-/far-infrared spectroscopic surveys', **Bonato, M.**; Negrello, M.; Cai, Z.-Y.; De Zotti, G.; Bressan, A.; Lapi, A.; Gruppioni, C.; Spinoglio, L.; Danese, L.; 2014, MNRAS, 438, 2547.
- 'Exploring the relationship between black hole accretion and star formation with blind mid-/far-infrared spectroscopic surveys', **Bonato, M.**; Negrello, M.; Cai, Z.-Y.; De Zotti, G.; Bressan, A.; Lapi, A.; Pozzi, F.; Gruppioni, C.; Danese, L.; 2014, MNRAS, 444, 3446.
- 'Predictions for surveys with the SPICA Mid-infrared Instrument', **Bonato, M.**; Negrello, M.; Cai, Z.-Y.; De Zotti, G.; Bressan, A.; Wada, T.; Kohno, K.; Maiolino, R.; Gruppioni, C.; Lapi, A.; Pozzi, F.; 2015, MNRAS, submitted.

Contents

Chapter 1

Introduction

In recent years great progress in understanding the formation and evolution of galaxies has been achieved, the space telescopes ESA/Herschel and NASA/Spitzer being key players in this game. Now we know that the bulk of the galaxy star formation (SF) and supermassive black hole (SMBH) accretion in the Universe occurred in the redshift interval $1 \lesssim \mathrm{z} \lesssim 3$ (Fig. 1.2), and that the evolution of galaxies, at variance with dark matter structure formation, proceeded in a "top-down" fashion, most massive galaxies and AGNs forming first ("cosmic downsizing"). The ubiquitous presence of SMBHs at the galaxy centers and the tight relations between their masses and the properties of the spheroidal stellar components (see Ferrarese & Ford, 2005; Kormendy & Ho, 2013, for reviews) reveal a mutual interaction between the black hole growth and the build up of the mass in stars. The details of this interaction, its effect on cosmic downsizing and the mechanism behind the SF in massive galaxies are largely unknown. While massive spheroidal galaxies are observed to be in essentially passive evolution since $z \simeq 1$–1.5 galactic disks are seen to follow a different evolutionary track, with SF continuing to the present time. Thus fundamental questions remain unanswered[1]:

---

[1] See the SPICA Yellow Book http://research.uleth.ca/spica/documents/pdf/SPICAYellowBookV3.pdf

- What influences and determines the interaction between SF and AGN accretion during galaxy formation and evolution?
- What are the processes determining the different modes of SF?
- How did the SMBHs in the galaxy centers form and grow?
- What are the physical processes shaping the galaxy mass functions?

In order to answer these questions, a detailed investigation of the physical processes operating in large samples of cosmic sources is necessary. Only spectroscopic observations in the IR can achieve this goal. The most active SF phases of galaxies and the associated AGN growth are severely dust-obscured (Fig. 1.3) and can therefore be best, or only, studied at IR to sub-mm and mm wavelengths. This has motivated a growing interest for IR to mm-wave spectroscopy.

Spectroscopic observations in this wavelength range are being or will be carried out from the ground (by the Combined Array for Research in Millimeter-wave Astronomy (CARMA), the Caltech Sub-millimeter Observatory (CSO), the Institut de Radioastronomie Millimétrique (IRAM) telescopes, the Large Millimeter Telescope (LMT), the Cerro Chajnantor Atacama Telescope (CCAT) and the Atacama Large Millimeter/submillimeter Array (ALMA), among others). But a giant leap ahead is expected from the SPace IR telescope for Cosmology and Astrophysics (SPICA) and the James Webb Space Telescope (JWST).

As mentioned above, the luminosity functions (LFs) of galaxies deviate strongly from the mass functions (MFs) of dark matter (DM) halos, especially at low and high luminosity/mass values. While the evolution of DM structures is governed by gravity, baryons are subject to a much more complex physics, including electromagnetic and mechanical feedback. The deviations of galaxy LFs at low luminosity/mass values may be explained

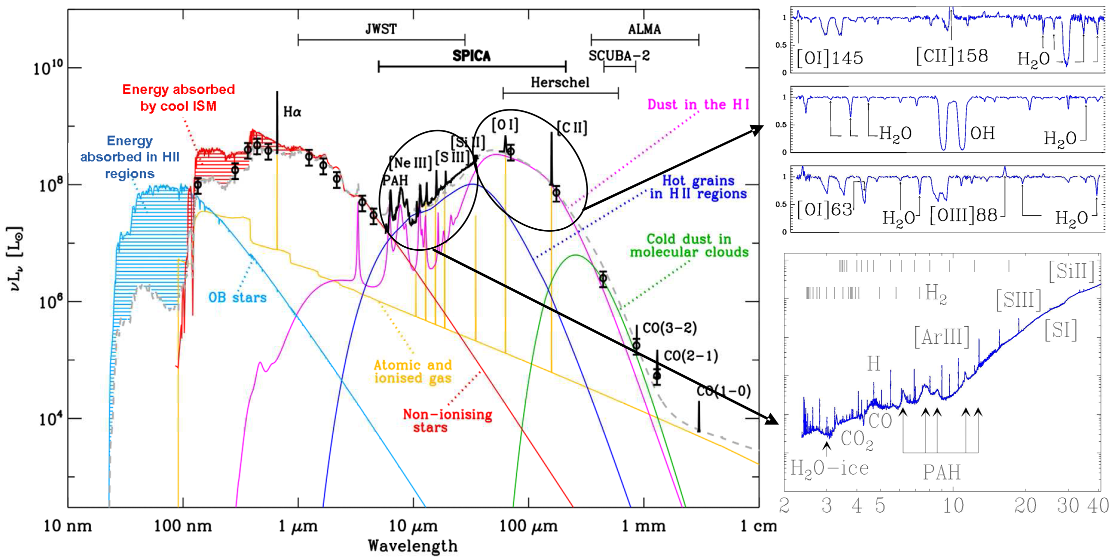

Figure 1.1: A synthetic rest-frame spectrum of a typical galaxy undergoing modest rates of star formation (with the indication of the wavelength ranges covered by SPICA and by some other facilities). On the right, detailed spectra in the mid-/far-IR region from ISO (Rosenthal et al. 2000; Goicoechea et al. 2004; Polehampton et al. 2007). From the SPICA Yellow Book (http://research.uleth.ca/spica/documents/pdf/SPICAYellowBookV3.pdf).

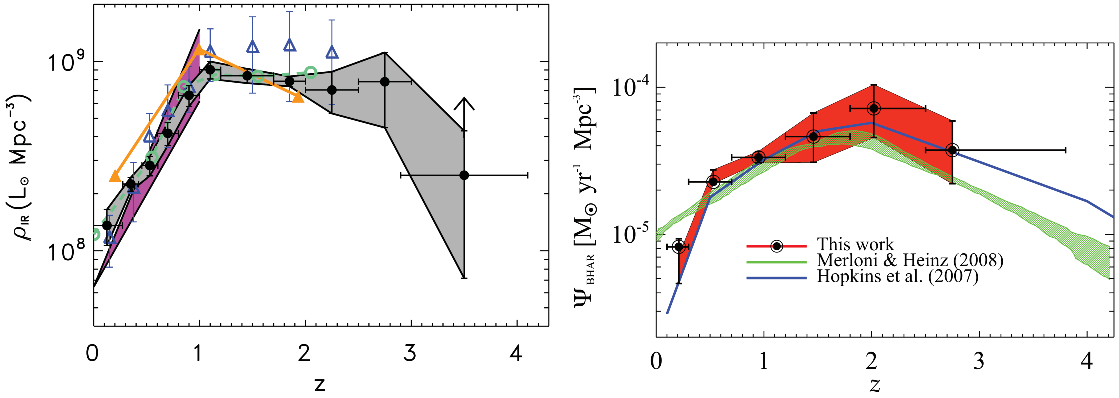

Figure 1.2: Left-panel: redshift evolution of the total IR luminosity density to $z = 4$ (from Gruppioni et al. 2013). Right-panel: redshift evolution of the black hole accretion rate density (from Delvecchio et al. 2014).

in terms of feedback processes of stellar origin (supernovae, stellar winds) and may depend on the environment. The bright/massive end of the LFs/MFs with their exponential cutoff may be understood in terms of a strong AGN feedback able to quench star formation of massive galaxies and the growth of the associated SMBHs. The recent discovery of massive gas outflows in luminous quasar hosts represents a preliminary observational evidence for a strong mutual interaction between the galaxy host and the AGN. The observation of a strong feedback has been made by *Herschel* through the detection of P Cygni profiles of far-IR OH transitions in local ULIRGS (Fischer et al. 2010a) and through interferometric detection of AGN driven outflows of molecular gas in luminous QSOs (Maiolino et al. 2012). Until now these observations have been possible only in few selected sources. The usefulness and the remarkable capabilities of spectroscopy in the mid- to far-IR have been extensively demonstrated by ISO, *Spitzer* and *Herschel*, but with modest sensitivities and on mainly local objects. Also the constraints provided so far by these instruments on AGNs are not stringent.

A much more systematic approach will be possible through IR spectroscopic observations performed by SPICA. SPICA will have a telescope of size similar to *Herschel*'s (3-m class) but a much better sensitivity thanks to cooling of the telescope assembly to very low temperatures ($\sim 6\,\mathrm{K}$). Its self-emission will then be strongly attenuated, allowing observations limited by the astronomical background. Moreover SPICA will extend the wavelength range down to the mid-IR. For the first time SPICA will be able to carry out blind spectroscopic surveys, wide and deep enough to measure the physical processes driving galaxy evolution out to $z \sim 4$. So, while *Herschel* has been able to detect spectroscopically only local galaxies and AGNs or rare, extremely bright and lensed galaxies at high z (Sturm et al. 2010; Ivison et al. 2010; George et al. 2013a), the spectroscopic capabilities of SPICA will allow us to perform deep spectroscopic surveys, up to high redshifts and with good statistics.

The $20{-}210\mu$m wavelength range covered by SPICA includes atomic and molecular lines over a wide interval of excitation levels for local and high redshift objects. The analysis of these lines will offer key information on physical processes operating during dust enshrouded phases of galaxy and AGN evolution.

Even with the deep and extended cosmological surveys recently performed by *Herschel* on areas of the sky where a wealth of multi-wavelength data are available (i.e., PEP, Lutz et al. 2011; HerMES, Oliver et al. 2012; GOODS-Herschel, Elbaz et al. 2011), disentangling the star formation and AGN contributions by means of photometric SED decomposition has proven to be very complicated (i.e. Berta et al. 2013; Delvecchio et al. 2014). Photometric data alone has demonstrated to be insufficient to clearly assess the nature of the detected objects. Instead the SPICA spectroscopy will make possible to measure the contributions from stellar and AGN activity to the bolometric luminosity. Consequently il will allow us to obtain separately the star formation and the black hole luminosity functions for large samples of sources and up to high redshifts. Furthermore, through the detection of massive molecular outflows by means of kinematics of mid- and far-IR lines, SPICA will be able to detect AGN and SF feedback during galaxy evolution. So it will be possible to understand the relation between the central black hole and its host spheroid establishing which process drives and regulates the other and through which physical mechanisms the two systems interact in their co-evolution. Finally, note also that only a small fraction of galaxies at $z \geq 2$ detected in the cited surveys have spectroscopic redshifts, but only photometric redshifts. These arguments show the necessity of mid- /far-IR spectroscopy to fill the gap in this wavelength range and to answer the many open questions related to the co-evolution.

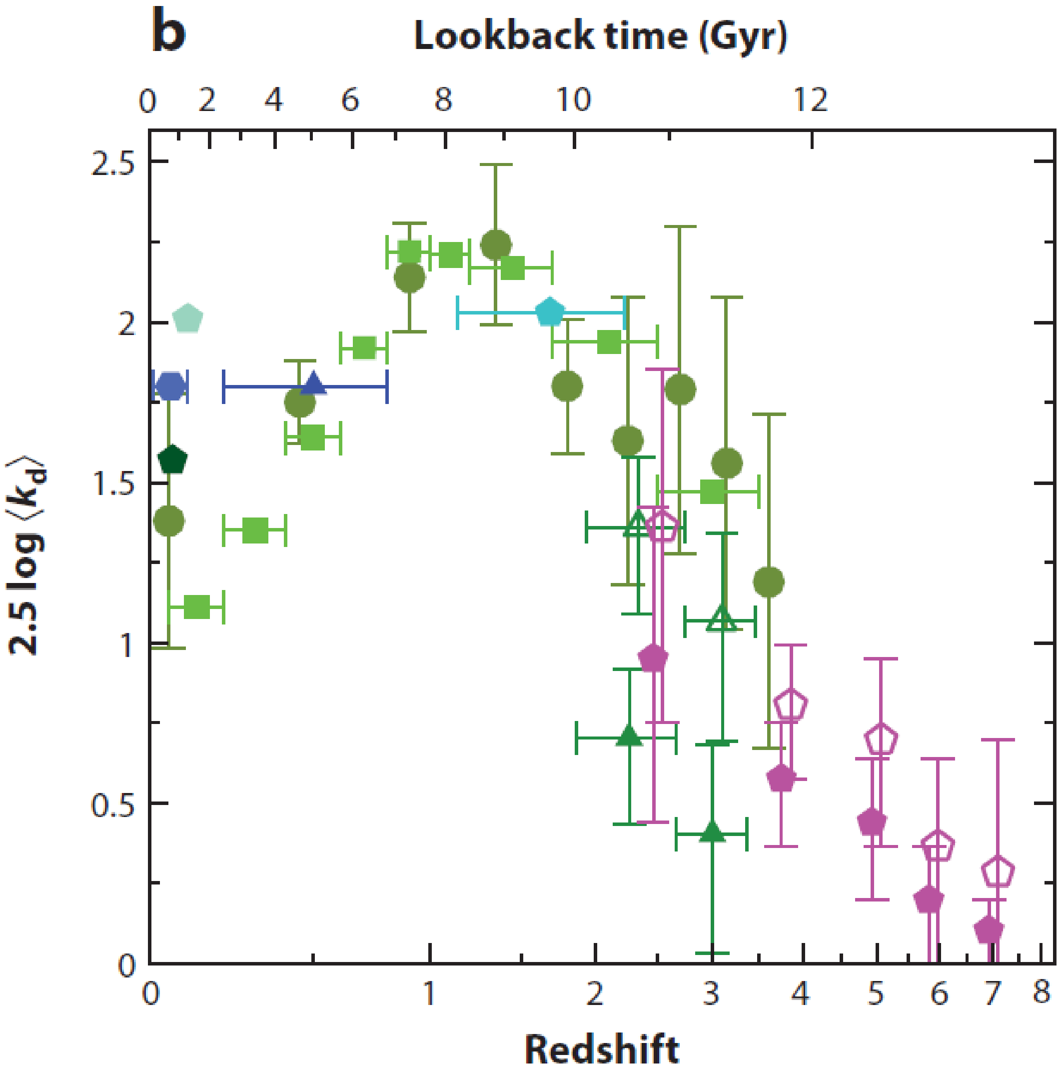

Figure 1.3: Mean dust attenuation in magnitudes as a function of redshift. Most of the data points shown are based on ultraviolet spectral slopes or stellar population model fitting. Data points from Burgarella et al. (2013) (olive green dots) are calculated by comparing the integrated FIR and FUV luminosity densities in redshift bins, rather than from the UV slopes or UV-optical spectral energy distributions. From Madau & Dickinson (2014).

Chapter 2

Galaxy formation and evolution

2.1 OAPD/SISSA "hybrid" galaxy evolution model

My reference model for the evolution of the IR luminosity functions is the one recently worked out by Cai et al. (2013) based on a comprehensive "hybrid" approach. The model starts from the consideration of the observed dichotomy in the ages of stellar populations of early-type galaxies on one side and late-type galaxies on the other (see Fig. 2.1, taken from Bernardi et al. 2010). Early-type galaxies and massive bulges of Sa galaxies are composed of relatively old stellar populations with mass-weighted ages $\gtrsim 8$–$9\,$Gyr (corresponding to formation redshifts $z \gtrsim 1$–1.5), while the disc components of spirals and the irregular galaxies are characterized by significantly younger stellar populations. Thus the progenitors of early-type galaxies, protospheroids, are the dominant star-forming population at $z \gtrsim 1.5$ (possible examples of such objects are the *Herschel* sources discussed in Ivison et al. 2013 and Fu et al. 2013), while IR galaxies at $z \lesssim 1.5$ are mostly late-type "cold" (normal) and "warm" (starburst) galaxies.

The physical model for proto-spheroidal galaxies is based on the approach by Granato et al. (2004, but see also Lapi et al. 2006, 2011 and Mao et al. 2007) which hinges upon high resolution numerical simulations showing that dark matter halos form in two stages

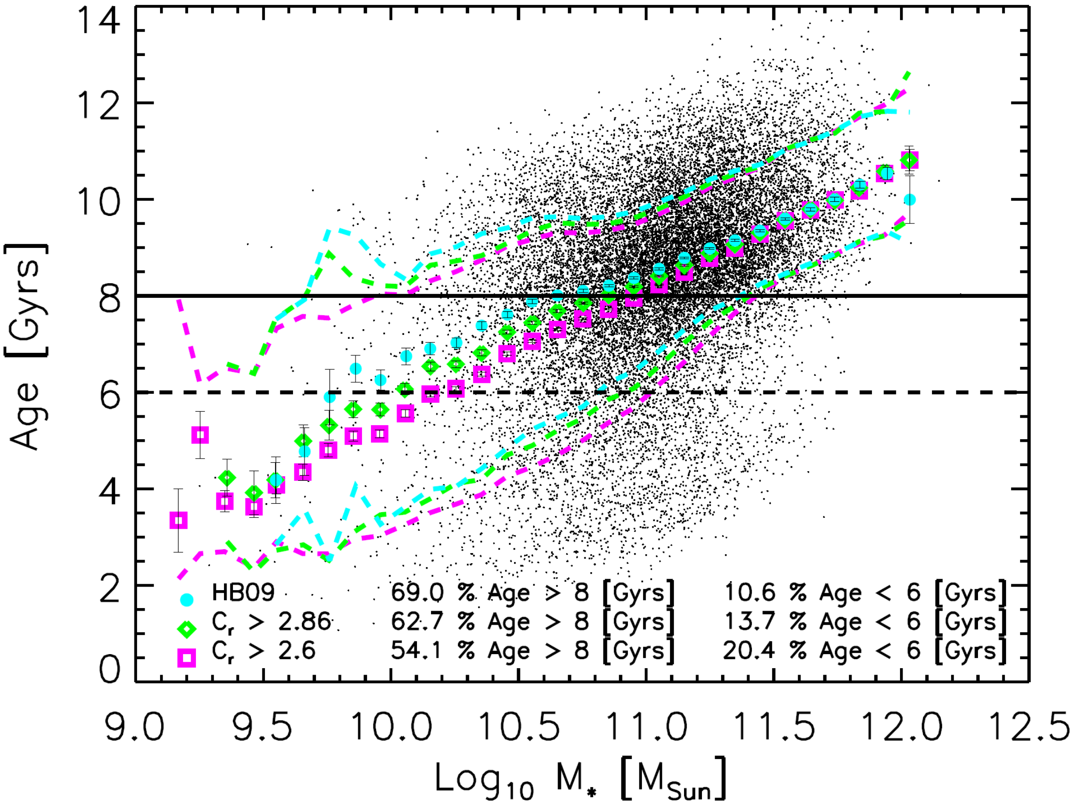

Figure 2.1: Joint distribution of age and stellar mass in the full sample of Bernardi et al. (2010). Small dots show a random subsample of the galaxies selected following Hyde & Bernardi (2009). Cyan filled circles, green diamonds and magenta squares show the median age at fixed stellar mass for a subsample selected following Hyde & Bernardi (2009), a subsample with $C_r > 2.86$ (two-thirds of the subsample comes from E+S0s), and a subsample with $C_r > 2.6$ (mix in which E+S0+Sa's account for about two-thirds of the objects), respectively. The dashed lines show the 1σ range around the median. The fraction of galaxies with luminosity weighted ages older than 8 Gyrs and younger than 6 Gyrs, for each of the selection methods, are shown. From Bernardi et al. (2010).

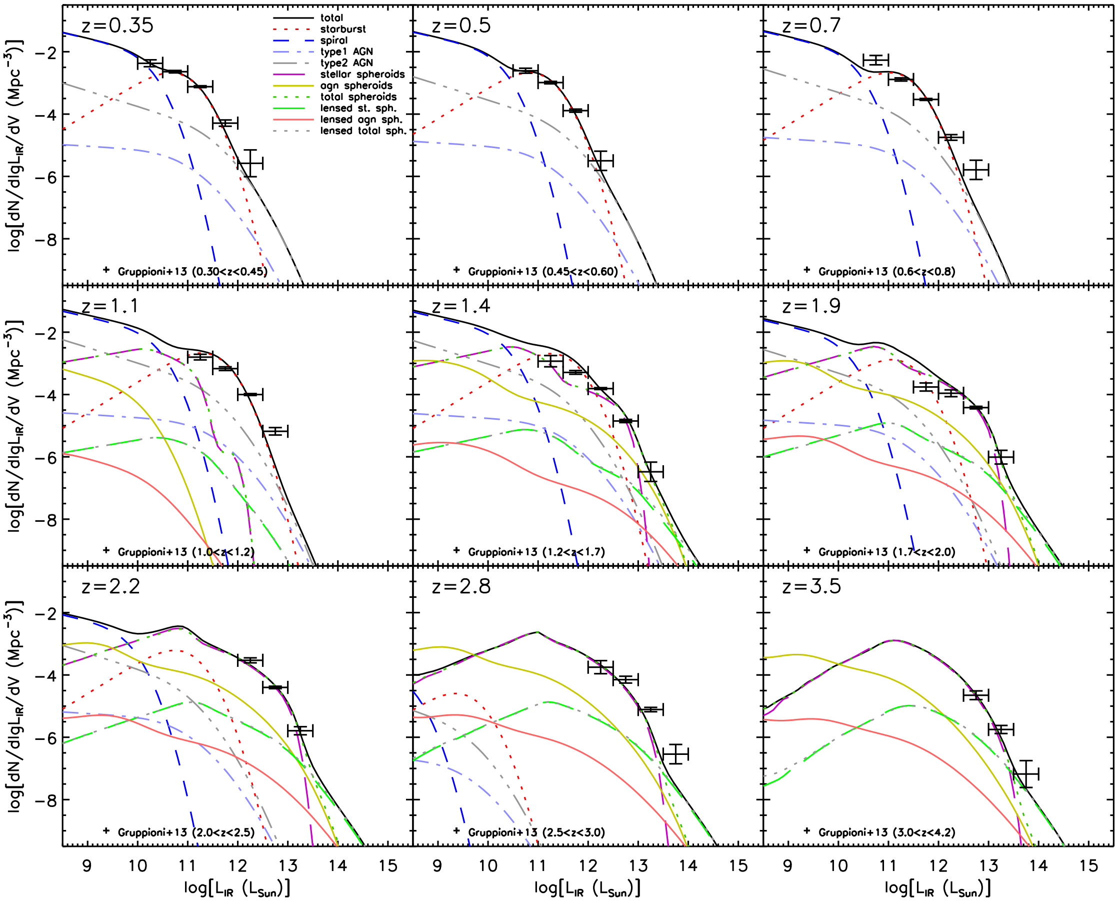

Figure 2.2: Comparison of the IR (8-1000 μm) luminosity functions at several redshifts yielded by the Cai et al. (2013) model with the observational determinations by Gruppioni et al. (2013), that became available only after the completion of the Cai et al. (2013) paper. At $z \leq 1.5$ the dominant contributions come from "warm" (dotted red lines) and "cold" (dashed blue lines) star-forming galaxies. Type-2 AGNs (dash-dot-dotted grey lines) dominate at the highest IR luminosities while type-1 AGNs (dash-dotted light blue lines) are always sub-dominant (in the IR). At $z > 1$ we have also contributions from proto-spheroidal galaxies (long dashed purple lines) and from the associated AGNs (both obscured and unobscured; solid yellow lines). The dotted dark green lines (that are generally superimposed to the long dashed purple lines) are the combination of the two components. The long dashed green lines show the contribution of the lensed stellar proto-spheroidal galaxies to the observed luminosity functions; the contribution of the associated AGNs is shown by the solid orange lines, while the dotted dark grey lines represent the combination of the two components. These lensed components are computed following Lapi et al. (2012).

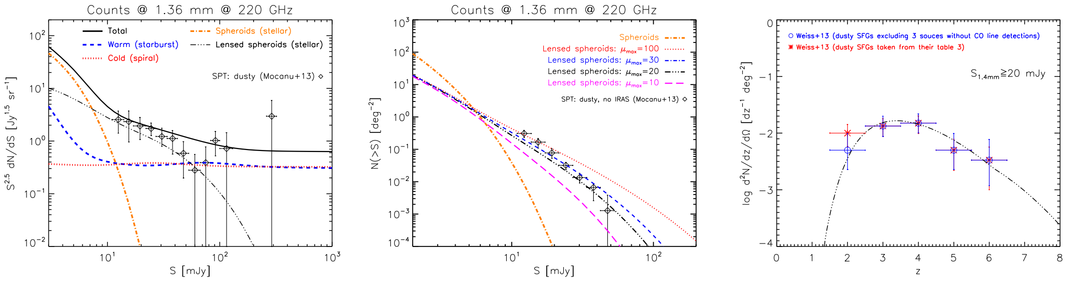

Figure 2.3: *Left panel*: Euclidean normalized differential SPT counts at 1.36 mm (220 GHz; Mocanu et al., 2013) of all dusty galaxies compared with the prediction of the Cai et al. (2013) model. The different lines correspond to the contributions of different source populations, as specified in the legend inside the panel. At variance with the counts presented in the Cai et al. (2013) paper, which do not allow for an upper limit to the gravitational amplification (i.e. implicitly assume point-like background sources), here a maximum amplification $\mu_{\max} = 20$ (corresponding to a source size of $\simeq 3$ kpc; Lapi et al., 2012) has been adopted for strongly lensed galaxies. A comparison between the model and the whole observed counts (not shown here to avoid over-crowding the figure) can be found in Cai et al. (2013). *Central panel*: integral counts of dusty galaxies without counterpart in the IRAS catalogue, interpreted as candidate strongly lensed galaxies, compared with the prediction of the Cai et al. (2013) model for different values of $\mu_{\max}$. The best match is obtained for $\mu_{\max}$ in the range 20–30. *Right panel*: comparison of the redshift distribution of strongly lensed SPT galaxies selected at 1.4 mm (Weiß et al., 2013) with predictions of the Cai et al. (2013) model. The photometric redshifts of the 3 galaxies without CO line detection are > 3.

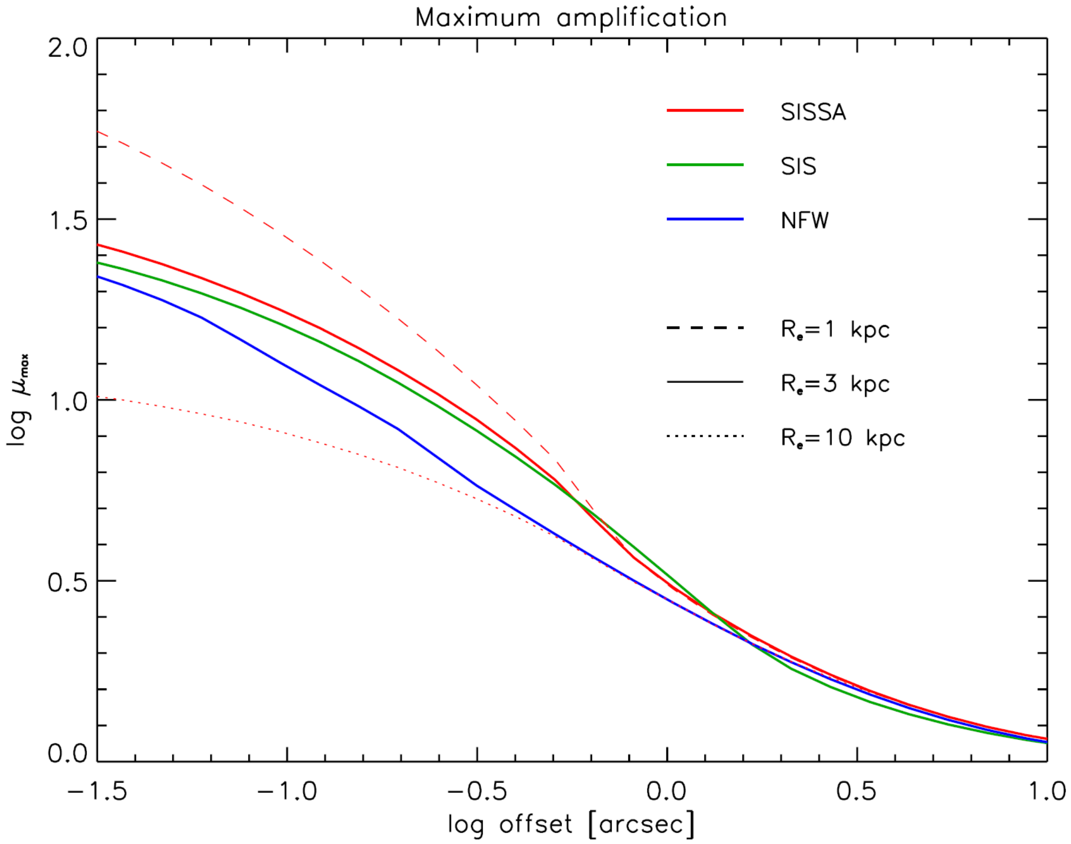

Figure 2.4: Maximum amplification for an extended source as a function of the offset between the center of the source and the optical axis, for the SISSA (red line), NFW (blue), and SIS (green) models. The source surface brightness profile is described by a Sérsic law with n=4 and effective radius R_e=3kpc (solid lines). For the SISSA model, are also shown the results with R_e=1kpc (dashed line) and R_e=10kpc (dotted line). (From Lapi et al. 2012).

(Zhao et al., 2003; Wang et al., 2011; Lapi & Cavaliere, 2011). An early fast collapse of the halo bulk, including a few major merger events, reshuffles the gravitational potential and causes the dark matter and stellar components to undergo (incomplete) dynamical relaxation. A slow growth of the halo outskirts in the form of many minor mergers and diffuse accretion follows. This second stage has little effect on the inner potential well where the visible galaxy resides.

The star formation and the growth of the central super-massive black hole are triggered by the fast collapse/merger phase of the halo and are controlled by self-regulated baryonic processes. They are driven by the rapid cooling of the gas and by the loss of angular momentum by radiation drag, are regulated by the energy feedback from supernovae (SNe) and from the active nucleus and are quenched by the AGN feedback. The latter is relevant especially in the most massive galaxies and is responsible for the shorter duration (0.5–0.7 Gyr) of their active star-forming phase. In less massive proto-spheroidal galaxies the star formation rate is mostly regulated by SN feedback and continues for a few Gyr. Only a minor fraction of the gas initially associated to the dark matter halo is converted into stars. The rest is ejected by feedback processes. The metal enrichment and the dust formation are rapid (timescales $\sim$ few $\times\, 10^7$ yr) so that most of the active star formation and black hole growth phase is dust enshrouded. The equations governing the evolution of the baryonic matter in dark matter halos and the adopted values for the parameters are given in the Appendix of the Cai et al. (2013) paper where some examples of the evolution with galactic age of quantities related to the stellar and to the AGN component are also shown. Since spheroidal galaxies are observed to be in passive evolution at $z \lesssim$ 1-1.5 (e.g., Renzini, 2006) they are bright at sub-mm wavelengths only at higher redshifts.

This scenario provides a physical explanation for the observed positive evolution of both galaxies and AGNs up to $z \approx 2.5$ and for the negative evolution at higher redshifts, for the sharp transition from Euclidean to extremely steep counts at (sub-)mm wavelengths, as well as for the (sub-)mm counts of strongly lensed galaxies, that are hard to account for by alternative, physical or phenomenological, approaches. The model successfully predicted (Negrello et al., 2007) the mm (Vieira et al., 2010) and sub-mm (Negrello et al., 2010) counts of strongly gravitationally lensed galaxies. Furthermore, as shown by Xia et al. (2012) and Cai et al. (2013), the halo masses inferred from both the angular correlation function of detected sub-mm galaxies (Cooray et al., 2010; Maddox et al., 2010) and from the power spectrum of fluctuations of the cosmic infrared background (Amblard et al., 2011; Planck Collaboration et al., 2011; Viero et al., 2013) are fully consistent with those implied by this scenario while are larger than those implied by the major mergers plus top-heavy initial stellar mass function (Baugh et al., 2005; Lacey et al., 2010) and smaller than those implied by cold flow models (Davé et al., 2010).

The evolution of late-type galaxies and of $z < 1.5$ AGNs is described using a parametric phenomenological approach. For the IR luminosity functions of both "warm" starburst galaxies and "cold" (normal) late-type galaxies the functional form:

$$\begin{aligned}&\Phi(L_{\rm IR}, z)\,\mathrm{d}\log L_{\rm IR} = \\ &\Phi^\star\left(\frac{L_{\rm IR}}{L^\star}\right)^{1-\alpha}\exp\left[-\frac{\log^2(1+L_{\rm IR}/L^\star)}{2\sigma^2}\,\mathrm{d}\log L_{\rm IR}\right]\end{aligned} \tag{2.1}$$

advocated by Saunders et al. (1990) was adopted. For the "warm" population power law density and luminosity evolution $[\Phi^\star(z) = \Phi^\star(z=0)\times(1+z)^{\alpha_\Phi}\ ;\ L^\star(z) = L^\star(z=0)\times(1+z)^{\alpha_L}]$ up to $z_{\rm break} = 1$ was assumed. The "cold" population, comprising normal disc galaxies, has only a mild luminosity evolution up to the same value of $z_{\rm break}$, as indicated by chemo/spectrophotometric evolution models. At $z > z_{\rm break}$ both $\Phi^\star(z)$ and $L^\star(z)$ are kept to the values at $z_{\rm break}$ multiplied by a smooth cut-off function. For further details and the values of the parameters, see Cai et al. (2013).

The model accurately fits a broad variety of data[1]: multi-frequency and multi-epoch

---

[1] See figures in http://people.sissa.it/∼zcai/galaxy_agn/.

luminosity functions of galaxies and AGNs, redshift distributions, number counts (total and per redshift bins). Figure 2.2 illustrates how the model predictions, without any adjustment to take into account the new data, compare to the multi-epoch IR (8-1000 μm) luminosity functions observationally estimated by Gruppioni et al. (2013), that became available only after the completion of the Cai et al. (2013) paper. Moreover, the model accurately accounts for the recently determined counts and redshift distribution of strongly lensed galaxies detected by the South Pole Telescope (SPT; Mocanu et al., 2013; Weiß et al., 2013), also published after the paper was completed (Fig. 2.3). The maximum gravitational amplification, $\mu_{\rm max}$, depends on the source size (see Fig. 2.4 taken from Lapi et al. 2012). The original Cai et al. (2013) estimates assumed point like sources. Figure 2.3 shows that SPT data constrain $\mu_{\rm max}$ to be $\simeq$ 20–30, corresponding to a half stellar mass radius of the source $R_e \simeq 3\,$kpc. A lower value of $\mu_{\rm max}$ ($\simeq 10$) is indicated by the counts of strongly lensed galaxies from 95 deg^2 of the *Herschel* Multi-tiered Extragalactic Survey (HerMES; Wardlow et al., 2013). On the other hand, estimated counts from the *Herschel* Astrophysical Terahertz Large Area Survey (H-ATLAS) Science Demonstration Phase (SDP) field (González-Nuevo et al., 2012) are consistent with the values of $\mu_{\rm max}$ implied by the SPT data. For completeness I also mention that the model over-predicts the 870 μm counts from the ALMA survey of submillimetre galaxies in the Extended Chandra Deep Field South (ECDFS; Karim et al., 2013). It should be noted, however, that sub-millimeter number counts in the ECDFS are significantly lower compared to any other deep fields observed at 850 μm, in line with results from optical/NIR surveys which revealed that several rest-frame optical populations are under-abundant in the CDFS compared to other deep fields (Weiß et al., 2009).

In Figs. 2.5 and 2.6 are illustrated comparisons between model and data, in redshift distributions (at several wavelengths and for several flux density limits) and in Euclidean normalized differential number counts (at wavelengths from 15 to 1380μm) respectively. Many

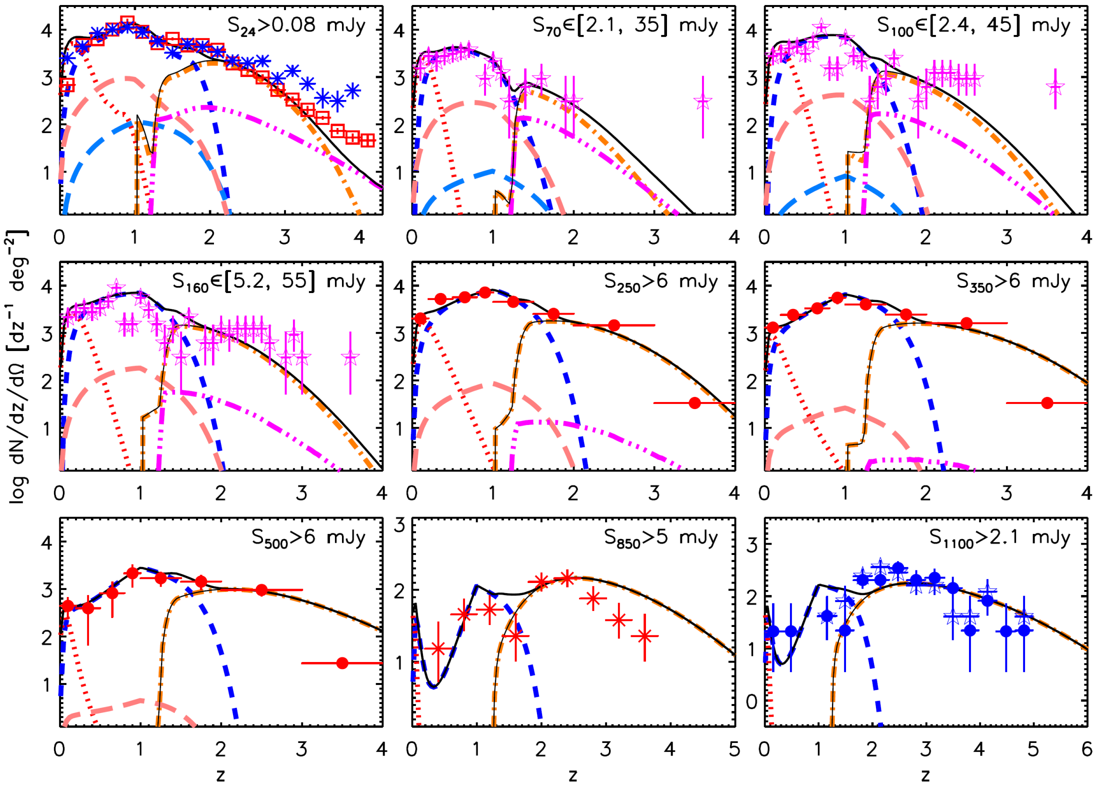

Figure 2.5: Comparison between Cai et al. (2013) model and observed redshift distributions at several wavelengths and for several flux density limits. Proto-spheroidal galaxies are represented by dot-dashed orange lines, the associated AGNs (both obscured and unobscured) by triple-dot-dashed magenta lines, the combination of the two components by thin solid black lines, "warm" star-forming galaxies by short-dashed blue lines, "cold" star-forming galaxies by dotted red lines, type-2 AGNs by long-dashed pink lines, type-3 AGNs (associated to dusty proto-spheroids) by triple-dot-dashed magenta lines, type-1 AGNs by long-dashed light-blue lines, the sum of all contributions by thick solid black lines. Data are from Le Floc'h et al. 2009 (red open squares, 24μm), Rodighiero et al. 2010 (blue stars, 24μm), Berta et al. 2011 (magenta open asterisks, 70, 100, and 160μm), Béthermin et al. 2012 (red filled circles, 250, 350, and 500μm), Chapman et al. 2005 (red stars, 850μm), and Yun et al. 2012 (blue open asterisks based on the optical photo-z and blue filled circles based on millimetric photo-z). (From Cai et al. 2013).

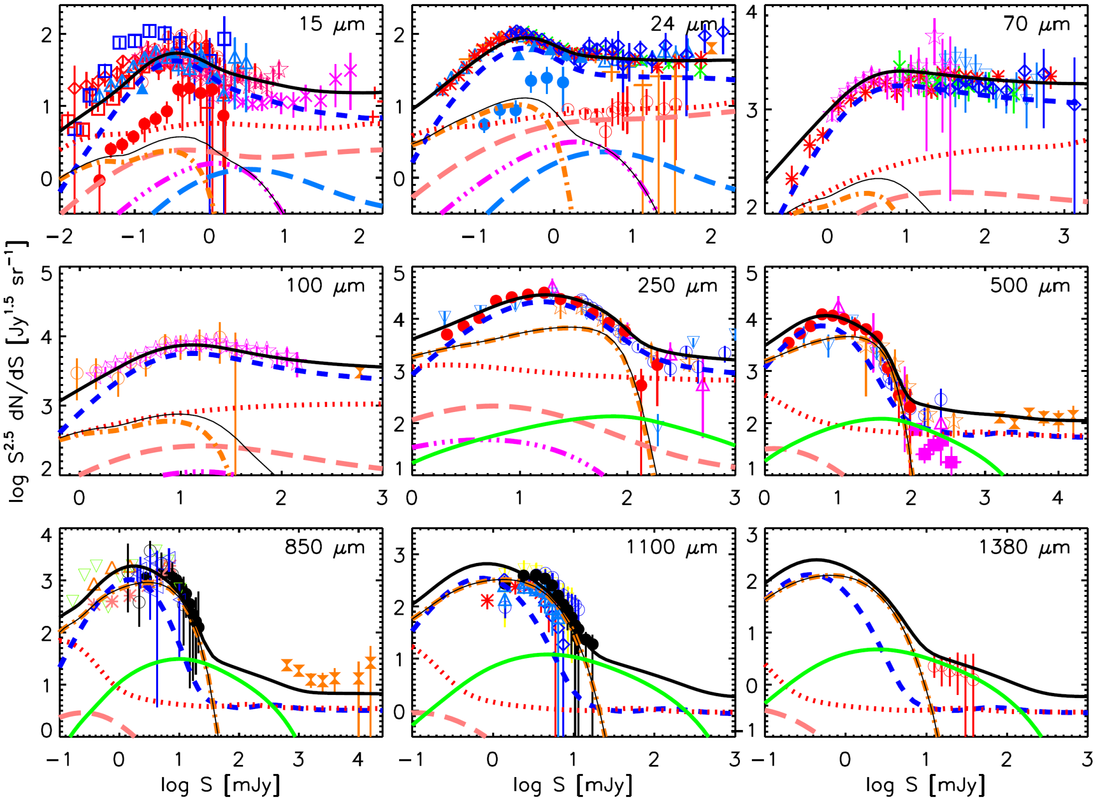

Figure 2.6: Euclidean normalized differential number counts at wavelengths from 15 to 1380μm. The thick solid lines are the sum of contributions from: "cold" late-type galaxies (dotted red lines), "warm" (starburst) late-type galaxies (dashed blue lines), type-1 AGNs (long-dashed light-blue lines), type-2 AGNs (long-dashed pink lines), stellar component of proto-spheroids (dot-dashed orange lines), AGN component of proto-spheroids (triple-dot-dashed magenta lines), strongly lensed ($\mu \geq 2$) proto-spheroids (solid green lines; only significant at $\lambda \geq 250\mu$m). The thin solid black lines show the counts of unlensed proto-spheroids, including both the stellar and the AGN components; $\lambda \geq 250\mu$m these counts essentially coincide with the counts of the stellar component only. The filled red circles in the 15μm panel refer to AGNs only. The filled blue circles and the open red circles in the 24μm panel refer to AGNs only and come from Treister et al. (2006) and from Brown et al. (2006), respectively. The purple filled squares in the 500μm panel show the estimated counts of strongly lensed galaxies (Lapi et al. 2012). The bright counts at 1.38mm are also generally interpreted as due to strongly lensed galaxies (Vieira et al. 2010; Greve et al. 2012). References for all the data points are given in Tab.3 of Cai et al. (2013). (From Cai et al. 2013).

other comparisons are shown by figures in the Web site http://people.sissa.it/∼zcai/galaxy_agn/.

2.2 Properties of emitting regions from infrared lines

The rest-frame mid- to far-infrared (IR) spectral region offers a rich suite of spectral lines that allow us to probe all phases of the interstellar medium (ISM): ionized, atomic and molecular (Spinoglio & Malkan, 1992).

Fig. 2.7 shows a broad sample of IR fine-structure lines, that covers a wide parameter space of the critical density vs. ionization potential diagram, tracing different astrophysical conditions: photodissociation regions, stellar/HII regions, AGN and coronal line regions (Spinoglio & Malkan 1992).

Emission line intensities and emission line ratios in the mid- and far-IR domain, that do not suffer as much from dust extinction as optical and UV emission lines, supply unique information on the physical conditions (electron density and temperature, degree of ionization and excitation, chemical composition) of the line emitting gas in the dominant dust-obscured regions of galaxies with intense star formation activity (Rubin et al., 1994; Panuzzo et al., 2003). For example, different IR fine-structure transitions of the same ion have different sensitivity to collisional de-excitation. This can be used to identify the typical electron density of the emitting gas. A typical line pair used for this purpose is [OIII]52/88 μm. Furthermore, the relative strengths of the fine-structure emission lines in different ionization stages of suitable elements may be used to probe the ionizing spectral energy distributions (SEDs) because different ionization stages are formed by significantly different photon energy ranges in the ionizing spectrum. Thus these line ratios are sensitive to the hardness of the stellar energy distribution, hence to the most massive stars present (e.g. Thornley et al., 2000). Therefore they provide information on the stellar initial mass

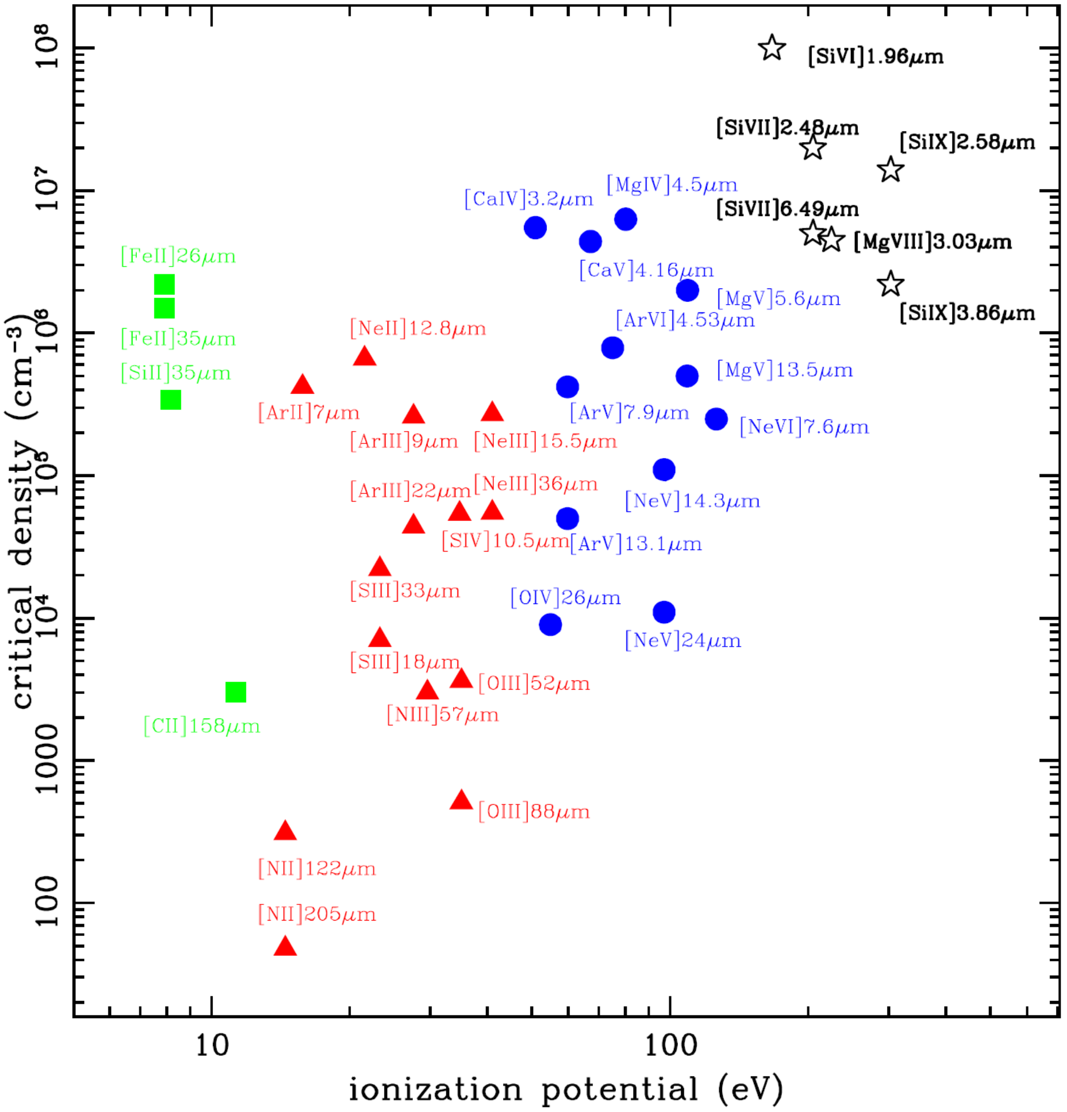

Figure 2.7: For a sample of IR fine-structure lines, critical density for collisional de-excitation as a function of ionization potential (From Spinoglio et al. 2012).

function (IMF), on the age of the ionizing stellar population and on the ionization parameter in single HII regions or in starbursts of short duration. Also measuring these ratios can constrain the emission from non-stellar sources of ionizing photons, such as AGNs. A typical ratio used for this purpose is [NeIII]15.55μm/[NeII]12.81μm.

Some of the FIR lines are important cooling lines, like the [CII]157.7μm, that is the primary coolant of the warm, neutral ISM, and the [OI]63.18μm and [OIII]88.36μm lines that become more important than [CII]157.7μm at high densities and temperatures.

The Polycyclic Aromatic Hydrocarbons (PAH) mid-IR emission lines are presumably originated in very large carbon-rich ring molecules or in very small amorphous carbon dust grains (Puget & Leger, 1989). Analyzing galactic IR spectra associated to different physical stages (photo-dissociation regions, HII regions, planetary nebulae and quiescent spirals), Galliano (2006) found that PAH line ratios are a powerful diagnostic tool of the physical conditions inside the region where the emission is originating. The PAH content is remarkably correlated with the rate of carbon dust production by AGB stars, consistent with the notion that PAHs form in the envelopes of these stars. AGB stars have a lifetime of several hundred million years and inject their material into the ISM when the system is already evolved. Thus PAH lines are a sort of chronometer constraining the age of the stellar populations. Since they are excited by absorption of single UV photons they are good tracers of the UV field and so of star formation.

H_2, the most abundant molecule in the Universe, is very useful to study the interstellar medium and the star formation processes. In fact the formation of H_2 on grains starts the chemistry of interstellar gas and then this molecule gives an important contribution to the cooling of astrophysical media, in particular in low-metallicity and low-temperature environments.

Moreover, we note that line profiles can be used to study the dynamics of the ionized gas.

The rest-frame mid-/far-IR wavelenght range contains several emission lines and spectral features useful to evaluate the contributions from AGN and star formation to the overall energy budget, hence to study the galaxy-AGN co-evolution these features provide an almost unique insight into highly obscured regions. ISO demonstrated that the ratios of emission lines tracing the hard UV field found in narrow line regions of AGNs (e.g., [NeV], [OIV], [NeVI]) to those tracing stellar HII regions (e.g., [SIII], [NeII]) versus the strength of the PAH emission features (indicators of star formation) define a diagram which separates star-forming from AGN-dominated galaxies (e.g., Genzel et al. 1998). *Spitzer* observations have expanded these results (Armus et al. 2007; Smith et al. 2007). They have further enabled the calibration of the (luminosity-corrected) line widths to the masses of black holes (Dasyra et al. 2011) and the calibration of the bolometric luminosity to the luminosities of lines that can be used as star formation tracers, e.g., the [NeII]12.8 μm, [SIII]34 μm, and [SiII]35 μm lines, several PAH features (e.g., 6.2, 7.7, 8.6 and 11.3 μm) and the H_2 pure rotational lines (Wu et al. 2010). ISO observations have also shown that far-IR fine structure lines (e.g. the line ratios of [CII]/[OI] vs. [OIII]/[OI]) can be used to discriminate between starbursts and AGNs (Spinoglio et al. 2003).

The combination of IR and X-ray survey data has revealed that the number density of accreting black holes is significantly lower than that of star-forming galaxies throughout cosmic history (Marconi et al. 2004; Merloni et al. 2010). This result suggests the presence of a missing population of obscured AGNs if black holes and galaxies co-evolve. The most extreme population of obscured AGN may be missed by X-ray surveys, even in hard X-ray bands. Observations at mid-IR wavelengths often provide the only means to reliably identify such AGNs. A key AGN signature at those wavelengths is the emission of fine structure lines from ions of high ionization potential. For example, the [NeV]14.3 μm line, with its ionization potential of 97 eV, is a reliable tracer of gas clouds photoionized by an AGN. Also the [OIV]25.89 μm line can be used for the same purpose (a negligible contribution to its luminosity can come from star-forming complexes). In addition to a tracer of AGN activity, a tracer of high column density can be used for the efficient identification of obscured AGNs in the mid-IR. This role can be played, for example, by the broad $9.7\,\mu$m silicate absorption feature, typically detected in absorption in type-2 AGN (Shi et al. 2006).

Fine-structure lines from ions of high ionization potential can be utilized not only to reveal previously unknown AGN populations (Goulding & Alexander 2009), but also to evaluate various properties of the black holes driving their activity. The luminosities of such lines (e.g., [OIV]) correlate with the AGN X-ray luminosity, showing that they are good tracers of the rate of accretion onto the black hole (Meléndez et al. 2008). The luminosity functions in such high ionization lines (Tommasin et al. 2010) can be used to study the accretion rate history of the Universe in alternative to X-rays. The widths of the same lines depend on the kinematics of the emitting clouds, determined by either the gravitational potential or by AGN feedback effects. They can be used to weigh the mass of black holes (Dasyra et al. 2008), permitting the creation of black hole mass functions.

Chapter 3

Exploring the early dust-obscured phase of galaxy formation with SPICA-SAFARI and CCAT

The star formation history in galaxies is one of the key processes we have to understand in order to reconstruct how the Universe evolved from small matter perturbations at the recombination epoch to the present richness of structures. While on large scales the evolution is driven by gravity, and numerical simulations in the framework of the current consensus cosmology have been remarkably successful in reproducing the galaxy distribution, on galaxy scales the complex baryon physics comes into play and current theories are still not up to the challenge of accurately modeling it. The only way to probe the physical processes at work in galaxies is by means of spectroscopy. While spectroscopic observations are routinely carried out at optical and near-IR wavelengths, the same observations are limited to small (and sometimes biased) samples of galaxies at longer wavelengths, where several key probes of the atomic, ionized and molecular phase of the interstellar medium are present (as discussed in par. 2.2).

A major progress in this field is expected with planned or forthcoming projects specifically devoted to mid- to far-IR spectroscopy such as the proposed SAFARI spectrometer (Roelfsema et al. 2012) for SPICA[1] and CCAT[2] (Woody et al. 2012). SAFARI is an imaging spectrometer designed to fully exploit the extremely low far-IR background environment provided by the SPICA observatory, whose telescope will be actively cooled at 6K. In each integration it will take complete 34–210 μm spectra with three bands ($34 - 60\,\mu$m, $60-110\,\mu$m, $110-210\,\mu$m), spatially resolving the full $2'\times2'$ field of view (FoV). CCAT is a 25 meter diameter Ritchey-Chretien (RC) telescope, that supports cameras and spectrometers operating in the 0.2–2.1 mm wavelength range with a goal FoV of $1\,\mathrm{deg}^2$ (requirement: $20'\times20'$).

Predictions for SPICA-SAFARI and CCAT spectroscopic surveys have been worked out by Spinoglio et al. (2012) using phenomenological models for the cosmological evolution of the IR luminosity of galaxies and Active Galactic Nuclei (AGNs) and empirical correlations between line and continuum luminosities.

Their calculations were based on the phenomenological evolutionary models by Franceschini et al. (2010), Gruppioni et al. (2011) and Valiante et al. (2009). The Franceschini et al. (2010) and the Gruppioni et al. (2011) models, like most classical backward evolution models, evolve the star-forming galaxies and the AGNs independently. This class of models have been quite successful in reproducing far-IR to sub-millimeter source counts but are clearly unable to predict the composite line spectra of galaxies in which star formation and AGN activity co-exist.

Valiante et al. (2009) have carried out a first attempt to deal in a coherent way with the cosmic evolution of IR emissions of both the starburst and the AGN components.

---

[1] http://www.ir.isas.jaxa.jp/SPICA/SPICA_HP/index-en.html; SPICA should compete for the next ESA/M5 call

[2] http://www.ccatobservatory.org; during 2014, the telescope design was successfully reviewed, the first CCAT instruments were identified, and land access was granted by the Chilean government for the telescope and access road, actually CCAT is ready to commence construction (http://www.ccatobservatory.org/docs/ccat-newsletters/CCAT%20Newsletter_2-Apr-14.pdf)

This was done by first estimating the distribution of the ratios between the 6 μm AGN continuum luminosity, $\nu L_{6\mu\mathrm{m}}$, and the total IR luminosity, $L_{\mathrm{IR}} = L_{8-1000\mu\mathrm{m}}$, for a sample of local galaxies in five IR luminosity bins. The luminosity dependent distributions of $\nu L_{6\mu\mathrm{m}}/L_{\mathrm{IR}}$ were derived subtracting the estimated starburst contribution from the *Spitzer* Infrared Spectrograph (IRS) mid-IR data for a complete sample of IRAS galaxies. A check on the evolution with redshift of the mean $\nu L_{6\mu\mathrm{m}}$ vs L_{IR} relation was made using IRS measurements for a sample of galaxies at $0.37 < z < 3.35$. The mean ratio $\nu L_{6\mu\mathrm{m}}/L_{\mathrm{IR}}$ was found to increase with luminosity as $\nu L_{6\mu\mathrm{m}}/L_{\mathrm{IR}} \propto L_{\mathrm{IR}}^{1.4\pm0.6}$. The increase was assumed to stop at $L_{\mathrm{IR,f}} = 10^{12.8}\,L_\odot$ for $z < 0.5$ and at $L_{\mathrm{IR,f}} = 10^{12}\,L_\odot$ for $z \geq 0.5$. Then an evolutionary law for L_{IR} was chosen and a value of $\nu L_{6\mu\mathrm{m}}/L_{\mathrm{IR}}$ drawn at random from the appropriate distribution was assigned to each source.

The strong increase of the average AGN luminosity fraction with increasing L_{IR} up to $L_{\mathrm{IR,f}}$ derived by Valiante et al. (2009) is however not supported by many other analyses, although the relationship between these two quantities is still matter of debate with studies showing either strong or marginal correlations between AGN and starburst luminosities (Lutz et al. 2008; Serjeant & Hatziminaoglou 2009; Alexander & Hickox 2012; Diamond-Stanic & Rieke 2012; Rosario et al. 2012; Mullaney et al. 2012, 2012a; Chen et al. 2013; Chen & Hickox 2014; Hickox et al. 2014). The apparently contradictory results of different analyses may be understood taking into account on one side that the characteristic timescale of black hole accretion is very different from that of star formation and on the other side that any relation between star formation rate (SFR) and accretion rate must break down as the AGN luminosity is at the Eddington limit.

The different timescales imply that accretion and star formation are not necessarily on at the same time. Hence the relation among the two quantities may have a large dispersion when individual objects are considered, still being strong when averaging over the whole population of star-forming galaxies (Chen et al., 2013). A coherent scenario for the interpretation of the various pieces of evidence on the connection between star formation and AGN activity has been elaborated by Lapi et al. (2014).

Although Spinoglio et al. (2012) study is quite recent, it is now possible to substantially improve the analysis taking advantage of the many data on the redshift dependent IR luminosity functions of different populations of extragalactic sources that were not available when the evolutionary models used by Spinoglio et al. (2012) were built, but are accounted for by the more recent Cai et al. (2013) model adopted in this work. Moreover, I have carefully revisited the correlations between line and continuum emissions. Major updates include:

- An assessment of the effect of the dispersion of line/continuum luminosity ratios, $\sigma_{\ell,c}$. As shown by Spinoglio et al. (2012), at high redshifts SAFARI and CCAT surveys are expected to detect sources in the high luminosity tail of the IR luminosity function. Since the latter is declining very steeply the derived line luminosity functions are strongly sensitive to $\sigma_{\ell,c}$.

- An analysis of the effect of dust obscuration. Molecular clouds inside which new stars are formed typically have very high optical depths (Silva et al., 1998; Vega et al., 2008) implying strong attenuation also at mid-IR wavelengths of lines produced within them. This may bias observations of line/continuum luminosity ratios if, e.g., they preferentially refer to objects with relatively low attenuations.

- The consideration of the observational evidences that different galaxy populations have different line/continuum luminosity ratios. For example, some IR lines of low-z Ultra-Luminous IR Galaxies (ULIRGs) are found to have much lower equivalent widths than observed for both less luminous galaxies at similar redshifts and for galaxies of similar luminosity at high-z.

Spectral line	$\langle \log(\frac{L_\ell}{L_{\rm IR}}) \rangle$ (σ)	$\langle \log(L_\ell)_{\rm UL} \rangle$ (σ)
PAH11.25μm	-2.29 (0.36)	9.01 (0.28)
[NeII]12.81μm	-3.11 (0.45)	-
[NeIII]15.55μm	-3.69 (0.47)	-
$H_2$17.03μm	-4.04 (0.46)	8.07 (0.34)
[SIII]18.71μm	-3.49 (0.48)	-
[SIII]33.48μm	-3.05 (0.31)	-
[SiII]34.82μm	-2.91 (0.28)	-
[OIII]51.81μm	-2.84 (0.44)	-
[NIII]57.32μm	-3.26 (0.16)	-
[OI]63.18μm	-2.99 (0.24)	8.97 (0.32)
[OIII]88.36μm	-2.87 (0.47)	-
[NII]121.9μm	-3.49 (0.36)	-
[OI]145.5μm	-3.80 (0.43)	-
[CII]157.7μm	-2.74 (0.37)	8.85 (0.29)

Table 3.1: Mean values of the log of line to IR (8-1000 μm) continuum luminosities, $\langle \log(L_\ell/L_{\rm IR}) \rangle$, and associated dispersions σ. For the PAH 11.25 μm, H_2 17.03 μm, [OI] 63.18 μm and [CII] 157.7 μm lines, $\langle \log(L_\ell/L_{\rm IR}) \rangle$ has been computed excluding local ULIRGs, for which the luminosity in these lines appears to be uncorrelated with $L_{\rm IR}$. For the latter objects the last column gives the mean values of $\log(L_\ell)$ in these lines and their dispersions (the luminosities are in solar units).

- The explicit predictions for the counts of strongly lensed galaxies (e.g. Negrello et al., 2007, 2010), that allow us to pierce the properties of galaxies that would otherwise be beyond the detection limits.

The plan of this chapter is the following. In par. 3.1 I discuss the line to IR luminosity ratios for the main mid/far-IR lines. In par. 3.2 I work out our predictions for line luminosity functions, number counts and redshift distributions in the SPICA/SAFARI and CCAT bands. In par. 3.3 I discuss possible SPICA/SAFARI and CCAT survey strategies, considering different integration times per FoV and areal coverages.

I adopt a flat ΛCDM cosmology with matter density $\Omega_{\rm m} = 0.32$, dark energy density $\Omega_\Lambda = 0.68$ and Hubble constant $h = H_0/100\,{\rm km\,s^{-1}\,Mpc^{-1}} = 0.67$ (Planck Collaboration et al., 2014).

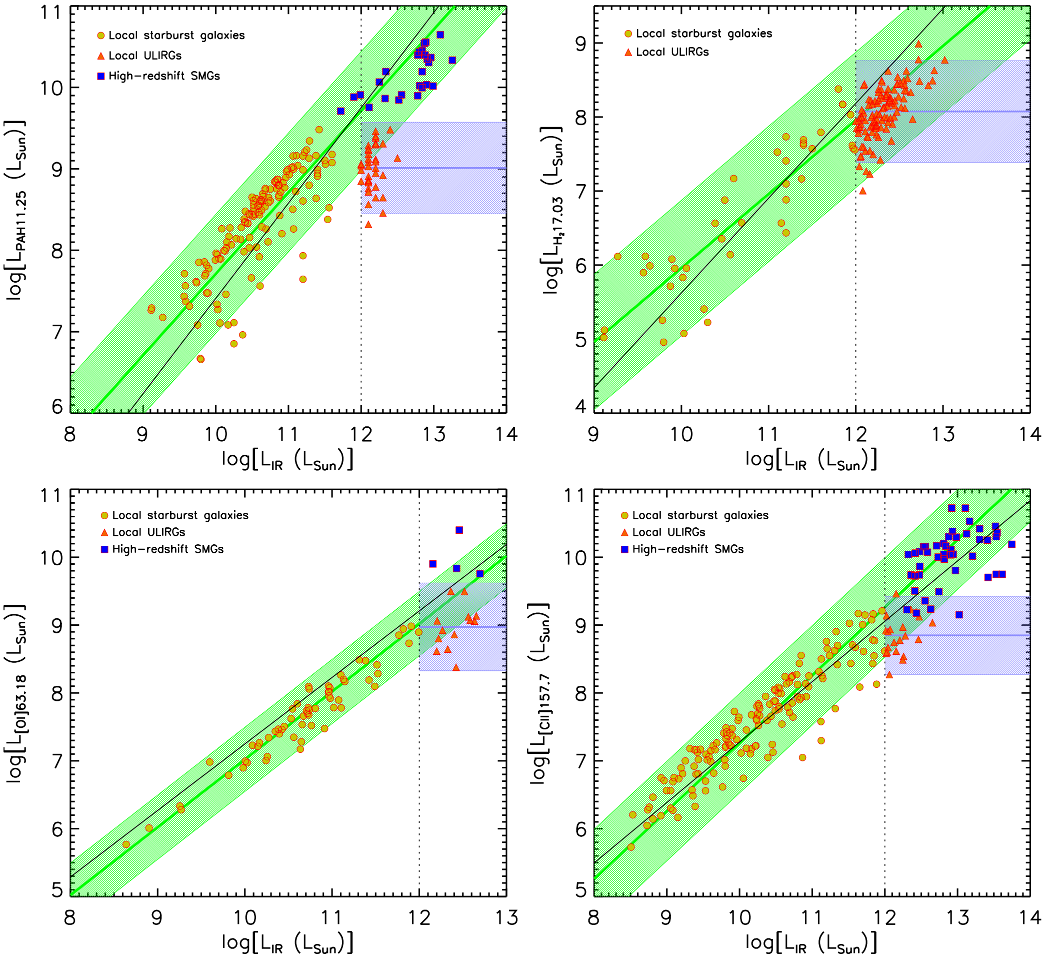

Figure 3.1: Luminosity of the PAH 11.25 μm (top-left panel), H_2 17.03μm (top-right panel), [OI] 63.18μm (bottom-left panel) and [CII] 157.7μm (bottom-right panel) lines, versus continuum IR luminosity. The green band shows the 2 σ range around the mean linear relation $\log(L_\ell) = \log(L_{\rm IR}) + c$ for local star-forming galaxies with $L_{\rm IR} < 10^{12}\, L_\odot$ (circles) and high-redshift SMGs (squares); the values of $c \equiv \langle \log(L_\ell/L_{\rm IR}) \rangle$ are given in Table 3.1. The black lines show the best-fit relations derived by Spinoglio et al. (2012). The azure band shows the 2 σ spread around the mean line luminosity for the sample of local ULIRGs (triangles) whose line luminosities appear to be uncorrelated with $L_{\rm IR}$ and are generally lower than expected from the linear relation holding for the other sources. The mean line luminosities $\langle \log L_\ell \rangle$ of these objects are given in Table 3.1. The vertical dotted black line at $L_{\rm IR} = 10^{12}\, L_\odot$ marks the lower boundary of ULIRG luminosities (Sanders & Mirabel, 1996).

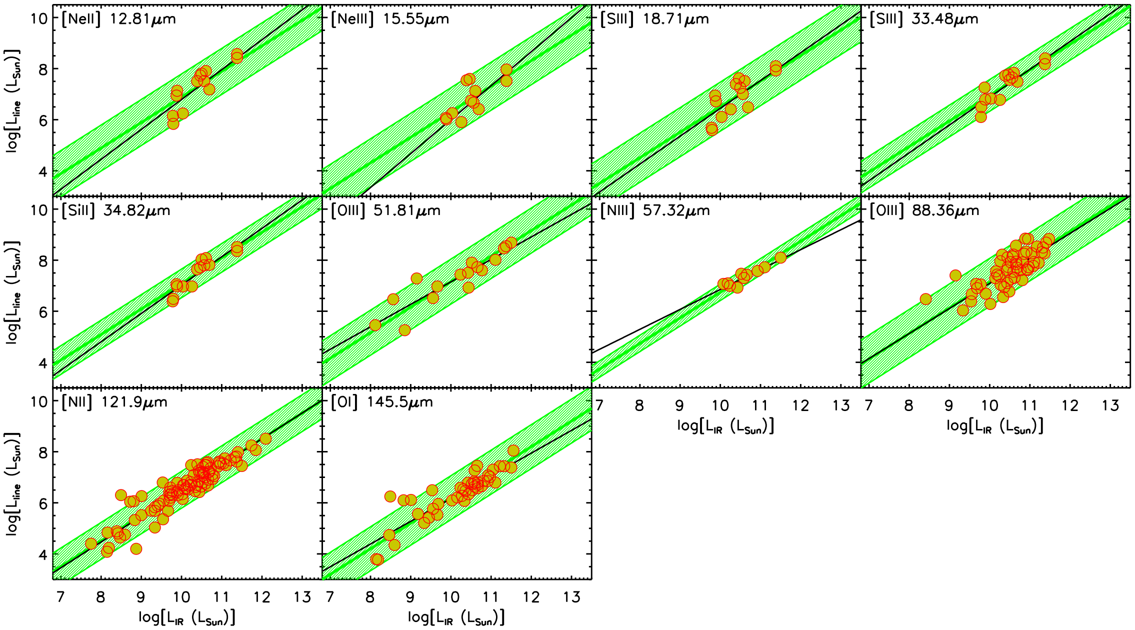

Figure 3.2: Log of the line luminosity as a function of $\log(L_{\rm IR})$, in solar units, for all the IR lines studied in the present work, except for the four lines (PAH $11.25\,\mu$m, H_2 $17.03\,\mu$m, [OI] $63.18\,\mu$m and [CII] $157.7\,\mu$m) considered separately (see Fig. 3.1). Data for $\lambda \leq 34.82\,\mu$m refer to the local starburst galaxies from the Bernard-Salas et al. (2009) catalogue. Data at longer wavelengths are from the heterogeneous sample of Brauher et al. (2008). The green band shows the $2\,\sigma$ spread around the mean linear relation $\log(L_\ell) = \log(L_{\rm IR}) + c$ (represented by the green line). The black lines show the best-fit relations derived by Spinoglio et al. (2012). My simulations (see subparagraph 3.1.1) favour a direct proportionality between line and continuum luminosity.

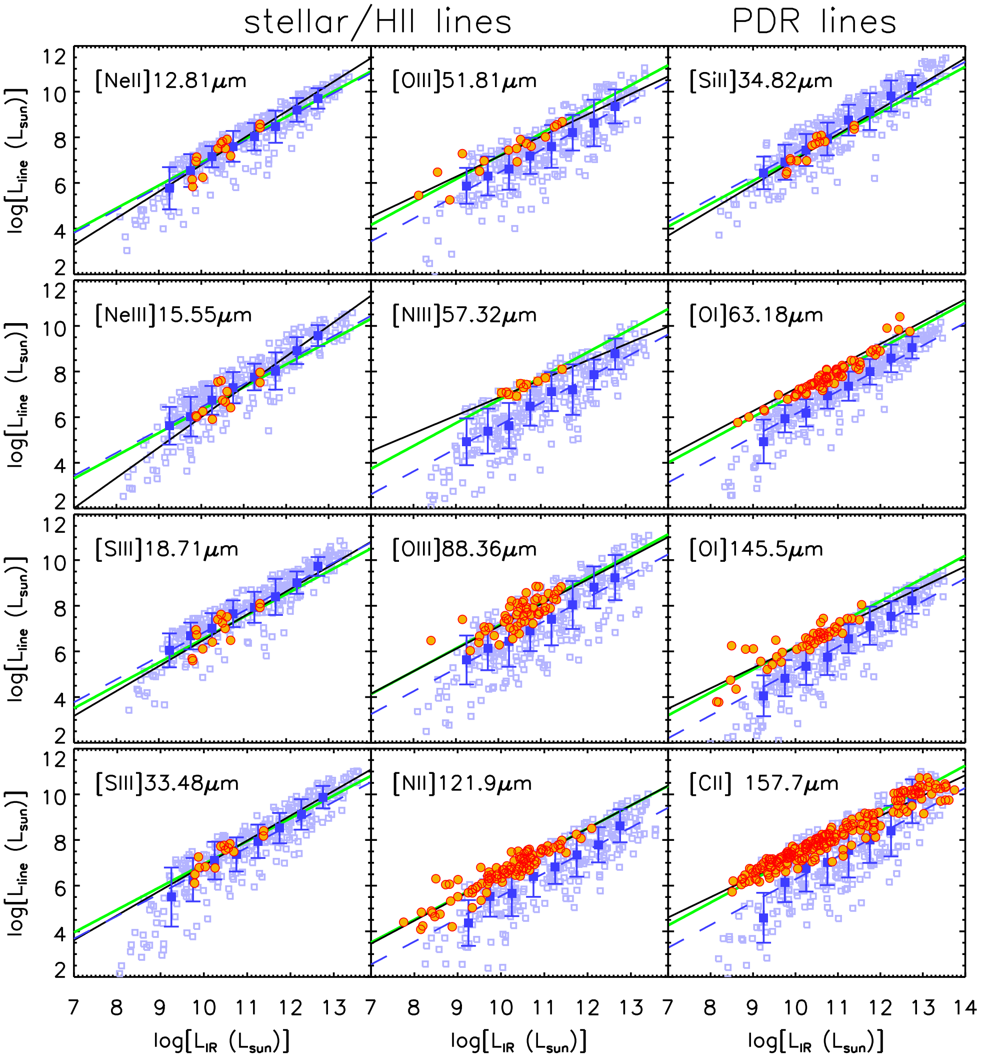

Figure 3.3: Simulated line versus IR luminosity (open squares) for some fine-structure lines produced in stellar/HII regions (left and central panels) and in PDRs (right panels). Only purely star-forming galaxies (no AGN contributions) are considered in the simulations. The dashed blue lines correspond to the average ratios $c = \langle \log(L_\ell/L_{\rm IR})\rangle$, i.e. to a direct proportionality between $\log(L_\ell)$ and $\log(L_{\rm IR})$, for the simulated data points after binning them in steps of 0.25 in $\log L_{\rm dust}$ (filled squares with error bars). The solid green lines correspond to the average ratios for the real data points, the solid black lines show the best-fit relations derived by Spinoglio et al. (2012). The data points (local star-forming galaxies and high-z SMGs) are the same as in Figs. 3.1 and 3.2. The simulations are systematically low for longer wavelength lines ($\lambda > 50\,\mu$m) as expected since they do not include the emission from outside HII regions.

3.1 Line versus IR luminosity

I have updated the relations between line and IR luminosities in several respects. First I have found and collected from the literature additional measurements for the PAH 11.25 μm, H_2 17.03 μm, [OI] 63.18 μm and [CII] 157.7 μm lines.

For the PAH 11.25 μm line I have used data on: local star-forming galaxies from Bernard-Salas et al. (2009); Brandl et al. (2006, 2009); O'Dowd et al. (2009, 2011) and Pereira-Santaella et al. (2010); local ULIRGs from Imanishi et al. (2007); Imanishi (2009); Imanishi et al. (2010); high-z SMGs from Sajina et al. (2007); Yan et al. (2005, 2007); Pope et al. (2008); Fiolet et al. (2010).

For the H_2 17.03 μm line, data on: local star-forming galaxies from Devost et al. (2004); Roussel et al. (2006); Farrah et al. (2007); Bernard-Salas et al. (2009); Brandl et al. (2009); Veilleux et al. (2009); Pereira-Santaella et al. (2010); Cormier et al. (2012); local ULIRGs from Higdon et al. (2006); Farrah et al. (2007); Veilleux et al. (2009).

For the [OI] 63.18 μm line, data on: local star-forming galaxies from Colbert et al. (1999); Malhotra et al. (2001); Negishi et al. (2001); Graciá-Carpio et al. (2011); Cormier et al. (2012); local ULIRGs from Luhman et al. (2003); Fischer et al. (2010b); Graciá-Carpio et al. (2011); high-z SMGs from Coppin et al. (2012).

Finally for the [CII] 157.7 μm line, data on: local star-forming galaxies from Carral et al. (1994); Colbert et al. (1999); Unger et al. (2000); Malhotra et al. (2001); Negishi et al. (2001); Graciá-Carpio et al. (2011); Cormier et al. (2012) and Swinbank et al. (2012); local ULIRGs from Luhman et al. (1998, 2003); Graciá-Carpio et al. (2011) and Swinbank et al. (2012); high-z SMGs from Colbert et al. (1999); Maiolino et al. (2009); Hailey-Dunsheath et al. (2010); Ivison et al. (2010); Stacey et al. (2010); Wagg et al. (2010); Cox et al. (2011); De Breuck et al. (2011); Graciá-Carpio et al. (2011); Swinbank et al. (2012); Walter et al. (2012); Riechers et al. (2013) and Carilli & Walter (2013).

From these samples I have excluded all objects for which there is evidence for a substantial AGN effect on the strength of the lines.

When far-IR luminosities over rest-frame wavelength ranges different from the one (8–1000 μm) adopted here were given, I applied the following conversions, from Stacey et al. (2010) and Graciá-Carpio et al. (2008), respectively

$$\begin{aligned} L_{\rm FIR}(40 - 500\,\mu m) &= 1.5 \times L_{\rm FIR}(42 - 122\,\mu m), \qquad (3.1) \\ L_{\rm IR}(8 - 1000\,\mu m) &= 1.3 \times L_{\rm FIR}(40 - 500\,\mu m). \qquad (3.2) \end{aligned}$$

The correlations between line luminosities and $L_{\rm IR}$ are shown in Fig. 3.1.

A common property of these four lines is that they are not (or not only) produced in HII regions but in (or also in) neutral and ionized interstellar medium and in photodissociation regions (PDRs). In fact, as pointed out by Panuzzo et al. (2003), because carbon has an ionization potential (11.26 eV) lower than that of H, the CII ion is present in PDRs and in the neutral medium illuminated by far-UV stellar radiation. Indeed, the [CII] 157.7 μm line is the most important coolant of the warm neutral medium. The excitation temperature of the [OI] 63.2 μm line is of 228 K (Kaufman et al., 1999) so that it can be easily produced in the neutral medium. The H_2 17.03 μm line is the strongest molecular hydrogen line used to give information on the conditions of the warm component in the PDRs. Polycyclic aromatic hydrocarbon (PAH) molecules are found to be ubiquitous in the interstellar medium (ISM) but apparently do not survive in the ionized gas (Tielens, 2008). An important consequence is that these lines suffer from much less extinction than those produced inside the dense, dust enshrouded stellar birth clouds.

Moreover, these lines are less directly linked to the SFR (and therefore to $L_{\rm IR}$) than lines originated deep in stellar birth clouds. This difference may have to do with the steep drop in the $L_{\rm [CII]}/L_{\rm IR}$ ratio observed in local ULIRGs (Luhman et al., 2003; Graciá-Carpio et al., 2011) while measurements of this ratio in high-redshift galaxies of similar luminosity is in the range observed for local galaxies with $L_{\rm IR} \lesssim 10^{11}\,L_\odot$ (Maiolino et al., 2009; Stacey et al., 2010; George et al., 2013b), although this finding may result from a selection effect. The estimated duration of the star formation episode in local ULIRGs, generally triggered by interactions/mergers, is $\sim 0.1\,$Gyr, i.e. of the same order as the typical time (as estimated by Silva et al., 1998) for hot stars to leave the dense birth clouds, where UV photons capable of ionizing C atoms have a short mean free path for absorption. Thus PDRs are necessarily small and $L_{\rm [CII]}$ correspondingly low. When the birth clouds begin to dissolve and larger PDRs can be produced the SFR is declining, in many cases below the threshold for the classification as ULIRGs.

In massive high-z galaxies the star formation is galaxy-wide and, as shown by Lapi et al. (2011), the data on luminosity functions indicate a longer duration (~ 0.5–$0.7\,$Gyr) of the intense star formation phase. Thus a significant fraction of hot stars have the time to leave the birth clouds and to migrate to less dense regions where they can generate extended PDRs while the SFR is still very high. This can explain their larger $L_{\rm [CII]}/L_{\rm IR}$ ratios. The same argument holds for non-ULIRG low-z galaxies whose star formation is long lived. Alternative explanations are discussed by Carilli & Walter (2013).

Anyway, the luminosity of low-z ULIRGs in these lines appears to be essentially uncorrelated with $L_{\rm IR}$. For these objects I have adopted Gaussian distributions of the logarithm of the line luminosity, $\log(L_\ell)$, around a mean value, $\langle\log(L_\ell)\rangle$, independent of $L_{\rm IR}$. On the contrary, the mean line luminosities for the other low- and high-z galaxies, and for all galaxies in the cases of the other lines considered here, are found to be tightly correlated with, and essentially proportional to $L_{\rm IR}$ (Figs. 3.1 and 3.2). Again I have adopted Gaussian distributions around $\langle\log(L_\ell/L_{\rm IR})\rangle$. The different relationships between line and continuum luminosities for low-z ULIRGs have however only a marginal impact on the predicted number of line detections. If I apply also to these galaxies the relationships found for the other populations the results change by less than 2%.

3.1.1 Simulations

The data on line and continuum luminosities refer to heterogeneous samples of galaxies, affected by unknown selection effects and unknown and variable amounts of dust extinction. They may therefore not be representative of the true distributions of line-to-IR luminosity ratios. In other words, the available measurements do not provide an unambiguous determination of the line-IR luminosity relationship. Also in some cases the statistics is plainly insufficient. To get some guidance on the choice of the slope of the relationship in the light of the relevant astrophysics I have carried out simulations taking into account the expected emission line intensities for different properties (density, metallicity, filling factor) of the emitting gas, different ages of the stellar populations, and the range of dust obscuration.

I have used the public library[3] of line luminosities compiled by Panuzzo et al. (2003). This library provides luminosities for 60 nebular emission lines, at wavelengths from the UV to the far-IR, and for 54 H and He recombination lines. There are 12 lines in common with those considered by Spinoglio et al. (2012). Eight of them are generated in star formation/HII regions while the others may be associated with PDRs. The library was produced interfacing version 94 of the photo-ionization code CLOUDY (Ferland, 2001) with the single stellar population (SSP) model of Bressan et al. (1994) which provides the spectrum of the ionizing sources. The analysis by Panuzzo et al. (2003) showed that the emission line spectrum of an HII region with fixed gas properties (metallicity, density and geometry) is described with reasonable precision by only three quantities: the production rates of photons capable of ionizing HI, HeI and OII:

$$Q_{\rm H} = \int_{\nu_{\rm H}}^{\infty} \frac{L_\nu}{h\nu} d\nu,\ Q_{\rm He} = \int_{\nu_{\rm H}e}^{\infty} \frac{L_\nu}{h\nu} d\nu,\ Q_{\rm O} = \int_{\nu_{\rm O}}^{\infty} \frac{L_\nu}{h\nu} d\nu, \tag{3.3}$$

where L_ν is monochromatic luminosity of the SSP (in units of $\mathrm{erg\,s^{-1}\,Hz^{-1}}$) and $\lambda_{\rm H} = c/\nu_{\rm H} = 911.76\,\mathrm{\AA}$, $\lambda_{\rm He} = c/\nu_{\rm He} = 504.1\,\mathrm{\AA}$ and $\lambda_{\rm O} = c/\nu_{\rm O} = 350.7\,\mathrm{\AA}$ are the photo-ionization

---

[3] http://pasquale.panuzzo.free.fr/hii/

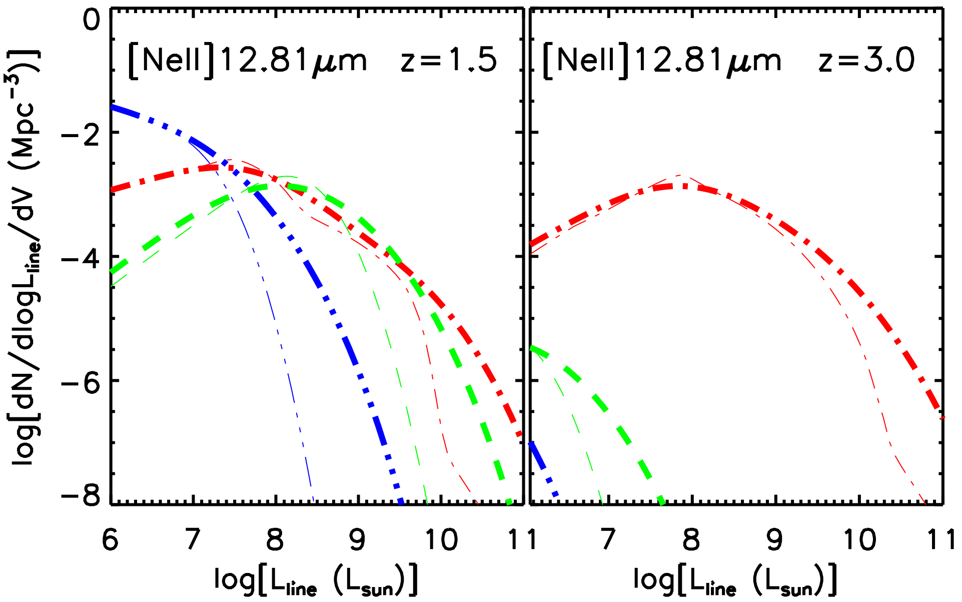

Figure 3.4: Effect of the dispersion in the line-to-IR luminosity ratio on the predicted luminosity function of the [NeII]12.81μm line. Thick lines: including dispersion; thin lines: no dispersion. Contributions of the different source populations: dash-dot-dotted blue lines for cold late-type galaxies, green dashed lines for warm late-type galaxies and dash-dotted red lines for proto-spheroids.

threshold wavelengths for HI, HeI and OII, respectively. Therefore, different ionizing sources that provide the same values of $Q_{\rm H}$, $Q_{\rm He}$ and $Q_{\rm O}$ produce the same emission line spectra, with reasonable accuracy.

The Panuzzo et al. (2003) library provides line luminosities for a grid of values of $Q_{\rm H}$, $Q_{\rm He}$ and $Q_{\rm O}$, and a range of values of the gas density, $\rho_{\rm gas}$, inside the star birth clouds, the gas metallicity, $Z_{\rm gas}$, and the gas filling factor, $\epsilon_{\rm gas}$. According to the authors the range of parameters covered by their library is fully adequate to describe the emission properties of the majority of star-forming galaxies. They do not consider line emission from PDRs and from diffuse warm neutral/low ionized medium, although some fine-structure IR lines are efficiently produced in these media. As a consequence their luminosities for these lines should be taken as lower limits.

To estimate the distribution of the line-to-IR luminosity ratios I simulated the SED of star-forming galaxies in the absence of dust extinction and derived both the line luminosities, using the Panuzzo et al. (2003) library, and the continuum IR luminosity, assuming an extinction law. The SED was generated using GALAXEV, the library of evolutionary stellar population synthesis of Bruzual & Charlot (2003). The continuum emission at the time $t_{\rm obs}$ of a stellar population characterized by a star formation rate SFR(t), assuming that the dust absorption only depends on the stellar age, is written as (e.g. Charlot & Fall, 2000):

$$L_\lambda^{\rm SED}(t_{\rm obs}) = \int_0^{t_{\rm obs}} {\rm SFR}(t_{\rm obs}-t) L_\lambda^{\rm SSP}(t) T_\lambda(t) dt, \tag{3.4}$$

where $L_\lambda^{\rm SSP}(t)$ is the power radiated per unit interval of frequency and of initial mass by the SSP of age t, $T_\lambda(t)$ is the "transmission function" defined as the fraction of the radiation, produced at wavelength λ and at the time t, that escapes from the galaxy. The fraction absorbed by dust in the galaxy is therefore $1 - T_\lambda(t)$. The transmission function is written as $T_\lambda(t) = \exp[-\tau_\lambda(t)]$, $\tau_\lambda(t)$ being the effective absorption optical depth at wavelength λ seen by stars at age t. Stars are born in dense molecular clouds, which dissipate typically on a time-scale $t_{\rm BC}$. This implies that the emission from stars younger than $t_{\rm BC}$ is more attenuated than that from older stars. Charlot & Fall (2000) write the transmission function as

$$T_\lambda(t) = \begin{cases} T_\lambda^{\rm BC} \times T_\lambda^{\rm ISM} & \text{for } t \leq t_{\rm BC}, \\ \\ T_\lambda^{\rm ISM} & \text{for } t > t_{\rm BC} \end{cases} \tag{3.5}$$

where $T_\lambda^{\rm BC}$ and $T_\lambda^{\rm ISM}$ are the fractions of radiation transmitted by the birth clouds and by the ambient inter-stellar medium (ISM), respectively, here assumed (for simplicity) to be independent of time. I model the effective optical depths of the birth clouds and of the

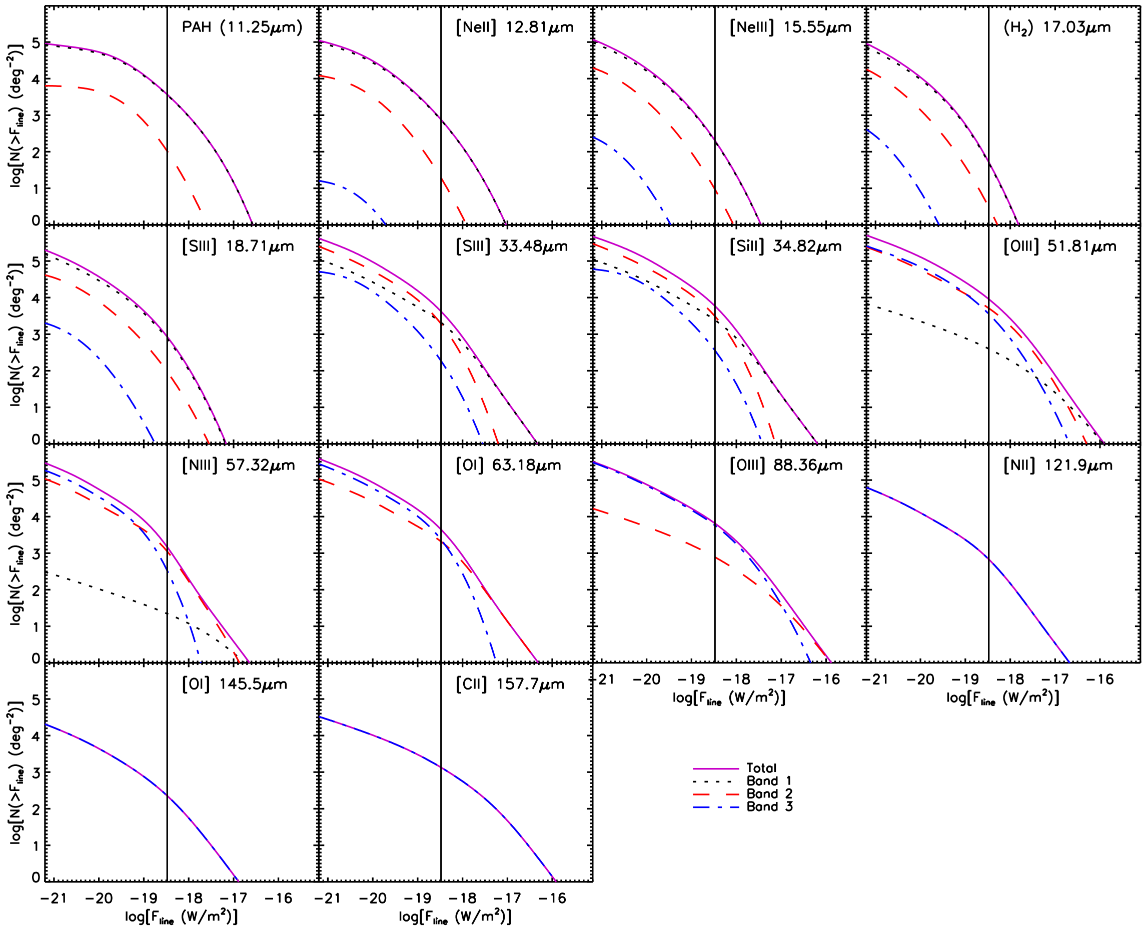

Figure 3.5: Integral counts of star-forming galaxies as a function of line fluxes over the full SPICA-SAFARI wavelength range (violet solid line) and in each of its three bands. The vertical lines correspond to the average detection limit in the 3 bands for the reference survey.

ISM, $\tau_\lambda^{\mathrm{BC}}$ and $\tau_\lambda^{\mathrm{ISM}}$, respectively, as in da Cunha et al. (2008):

$$\tau_\lambda^{\mathrm{BC}} = (1-\mu)\tau_V \left(\frac{\lambda}{5500}\right)^{-1.3} \tag{3.6}$$

$$\tau_\lambda^{\mathrm{ISM}} = \mu\tau_V \left(\frac{\lambda}{5500}\right)^{-0.7}, \tag{3.7}$$

τ_V being the total effective V-band absorption optical depth of the dust seen by young stars inside the birth clouds and $\mu = \tau_V^{\mathrm{ISM}}/(\tau_V^{\mathrm{BC}} + \tau_V^{\mathrm{ISM}})$ the fraction of this contributed by dust in the ambient ISM.

The total luminosity absorbed by dust in the birth clouds and reradiated at far-IR/submillimeter wavelengths is (da Cunha et al., 2008)

$$L_{\mathrm{dust}}^{\mathrm{BC}}(t_{\mathrm{obs}}) = \int_0^\infty \mathrm{d}\lambda (1 - T_\lambda^{\mathrm{BC}}) \int_0^{t_{\mathrm{BC}}} \mathrm{d}t \, \mathrm{SFR}(t_{\mathrm{obs}} - t) L_\lambda^{\mathrm{SSP}}(t), \tag{3.8}$$

while the total luminosity absorbed by the *ambient ISM* is

$$L_{\mathrm{dust}}^{\mathrm{ISM}}(t_{\mathrm{obs}}) = \int_0^\infty \mathrm{d}\lambda (1 - T_\lambda^{\mathrm{ISM}}) \int_{t_{\mathrm{BC}}}^{t_{\mathrm{obs}}} \mathrm{d}t \, \mathrm{SFR}(t_{\mathrm{obs}} - t) L_\lambda^{\mathrm{SSP}}(t). \tag{3.9}$$

Therefore the total luminosity absorbed and re-radiated by dust is

$$L_{\mathrm{dust}}(t_{\mathrm{obs}}) = L_{\mathrm{dust}}^{\mathrm{BC}}(t_{\mathrm{obs}}) + L_{\mathrm{dust}}^{\mathrm{ISM}}(t_{\mathrm{obs}}). \tag{3.10}$$

I take this as the total infrared luminosity L_{IR}.

The luminosity of a nebular line of wavelength λ_ℓ is given by

$$L_\ell(t_{\mathrm{obs}}) = \int_0^{t_{\mathrm{BC}}} \mathrm{SFR}(t_{\mathrm{obs}} - t) L_\ell^{\mathrm{SSP}}(t) T_{\lambda_\ell}(t) \, \mathrm{d}t, \tag{3.11}$$

where $L_\ell^{\mathrm{SSP}}(t)$ is the luminosity of the line produced in the HII regions by a stellar generation of age t. GALAXEV was used to compute the SSP continuum luminosity, $L_\lambda^{\mathrm{SSP}}(t)$, from which the Q-values are derived as a function of the SSP age and used to get the line luminosities from Panuzzo's library. Within GALAXEV I adopt the SSP model computed with the evolutionary tracks and isochrones by Bertelli et al. (1994), with solar metallicity (i.e. $Z = Z_\odot = 0.02$) and a Chabrier (2003) IMF. I assume an exponentially declining star formation rate, $\mathrm{SFR}(t) = (A_{\mathrm{SFR}}/\tau)\exp(-t/\tau)$, with $\tau = 10^7\,\mathrm{yr}$ ($=t_{\mathrm{BC}}$). The normalization, A_{SFR}, corresponds to the stellar mass assembled by the time $t >> \tau$. Line luminosities were simulated for different values of t_{obs}, A_{SFR}, ρ_{gas}, ϵ_{gas}, τ_V and μ within the range specify below, assuming uniform distributions,

- $\log(t_{\mathrm{obs}}/\mathrm{yr}) \in [5.0 - 8.0]$,
- $\log(A_{\mathrm{SFR}}/M_\odot) \in [7.0 - 11.0]$,
- $\rho_{\mathrm{gas}} \in [10 - 10000]$ and $\epsilon_{\mathrm{gas}} \in [0.001 - 1.0]$, as these are the intervals considered by Panuzzo et al. (2003),
- $\log(\tau_V) \in [\log 2 - 2]$ as in da Cunha et al. (2010),
- $\mu\tau_V \in [0 - 2]$ as in da Cunha et al. (2010).

I made 300 simulations for each line. The derived line luminosities are shown in Fig. 3.3 as a function of the continuum IR luminosity and compared with the available data. The solid green lines and the dashed blue lines correspond to a direct proportionality between $\log(L_\ell)$ and $\log(L_{\mathrm{IR}})$ i.e. to the average ratios $c = \langle\log(L_\ell/L_{\mathrm{IR}})\rangle$ for real and simulated data, respectively. For simulated data the ratios were computed after binning them in steps of 0.25 in $\log L_{\mathrm{dust}}$.

Overall, I find a good agreement between observed and simulated distributions of luminosities for lines with $\lambda < 50\,\mu\mathrm{m}$. For these lines the simulations are consistent with a direct proportionality between L_ℓ and L_{IR} and the derived values of $c = \langle\log(L_\ell/L_{\mathrm{IR}})\rangle$

are consistent with the determinations directly based on the data. On the other hand, the luminosities of longer wavelength lines found from simulations fall systematically below the observed luminosities as expected, since, as mentioned above, the Panuzzo et al. (2003) library refers to the emission line spectrum of HII regions only.

Based on these results, I have adopted the mean $\log(L_\ell/L_{\rm IR})$, or the mean $\log(L_\ell)$ in the case of low-z ULIRGs, and the associated dispersions derived from observations, buying from simulations the indication of a direct proportionality between line and IR luminosity. As illustrated by Fig. 3.3 the relationships obtained in this way differ from those derived by Spinoglio et al. (2012) from direct fits of the data. Differences are small whenever the data points are numerous and span a broad range of $L_{\rm IR}$ but may be substantial in other cases (up to a factor of 10 at the highest and lowest luminosities). This illustrates the benefit of exploiting astrophysical inferences, as per my simulations.

3.2 Line luminosity functions and number counts

The line luminosity functions can be easily computed from the IR ones by convolving the latter with the distribution of the IR-to-line luminosity ratios, $p[\log(L_{\rm IR}/L_\ell)]$, i.e.

$$\frac{{\rm d}\mathcal{N}^3(L_\ell,z)}{{\rm d}\log L_\ell\,{\rm d}z\,{\rm d}V}=\int_{-\infty}^{+\infty}\Phi(L_\ell,z)p[\log(L_{\rm IR}/L_\ell)]\log L_{\rm IR}, \tag{3.12}$$

where $\Phi(L_{\rm IR},z)$ is the comoving luminosity function per unit ${\rm d}\log L_{\rm IR}$, and p is assumed to be a Gaussian with mean value and dispersion given in Table 3.1. However I do not use this formalism but adopt instead a Monte Carlo approach in which simulated catalogues are constructed from the theoretical IR luminosity functions. This approach has the advantage of providing information on the luminosity (and flux) of *all* the lines, at the same time, for each simulated object and therefore allows me to predict the number of galaxies detectable in two or more lines in future spectroscopic surveys.

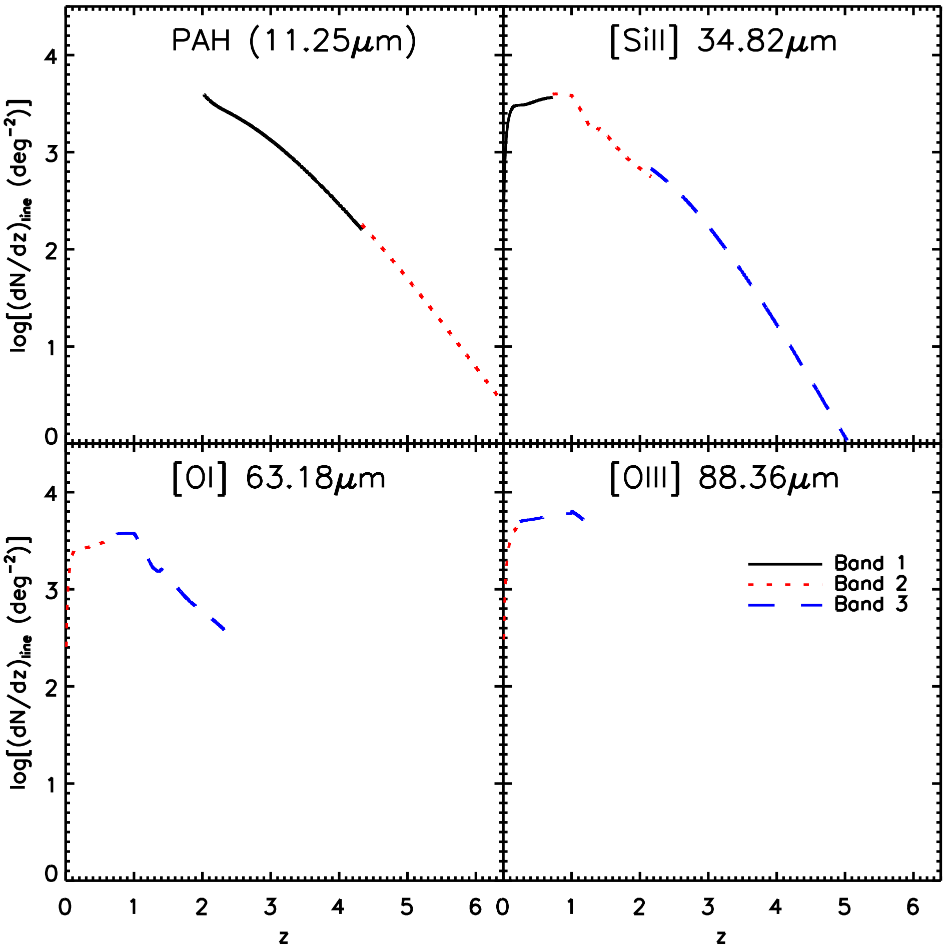

Figure 3.6: Examples of the predicted redshift distributions of sources detected by SPICA-SAFARI for 1 hr exposure per FoV. The different colours correspond to the 3 spectral bands.

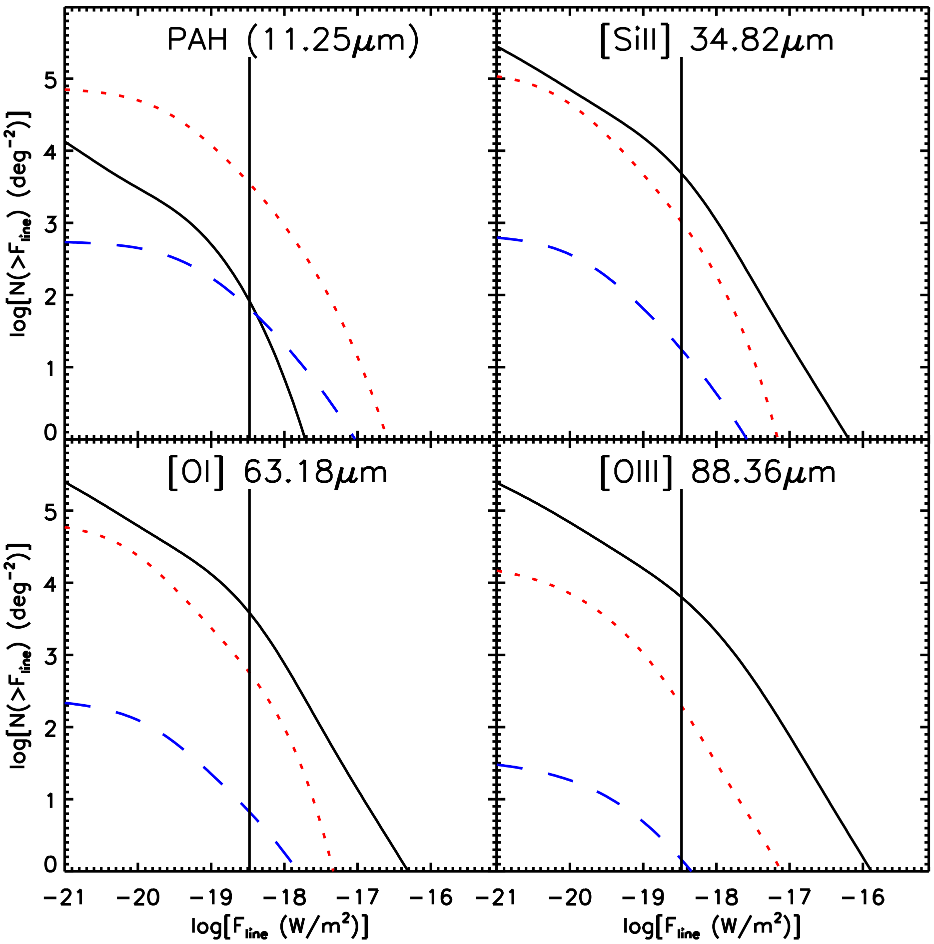

Figure 3.7: Contributions of different galaxy populations (solid black line: late-type – starburst and spiral – galaxies; dotted red line: unlensed proto-spheroids; dashed blue line: gravitationally lensed proto-spheroids) to the integral counts as a function of fluxes in the PAH 11.25μm, [SiII] 34.82μm, [OI] 63.18μm and [OIII] 88.36μm lines, within the SPICA-SAFARI wavelength range. The vertical lines correspond to the average value of the detection limits (3.7×10^{-19} W/m^2, 3.4×10^{-19} W/m^2, 2.9×10^{-19} W/m^2) for the three bands ($34 - 60\,\mu$m, $60 - 110\,\mu$m, $110 - 210\,\mu$m) for 1-hr exposure per FoV.

The simulation is performed as follows. For a given galaxy population and a given redshift bin, Δz, I draw from the corresponding IR luminosity function a number of IR luminosities equal to that of the objects expected over a (reference) area $\Omega = 0.5\,\mathrm{deg}^2$, and with IR luminosity greater than a minimum value that I set[4] to $\log(L_{\mathrm{IR,min}}/L_\odot) = 7.0$, i.e.

$$\mathcal{N}(z,\Omega) = \int_{\log L_{\mathrm{IR,min}}}^{+\infty} \Phi(L_\ell, z)\, \mathrm{d}\log L_{\mathrm{IR}}\, \frac{\mathrm{d}^2 V_c(z)}{\mathrm{d}z\,\mathrm{d}\Omega}\, \Delta z\, \Omega, \tag{3.13}$$

where $\mathrm{d}V_c(z)$ is the comoving volume element.

I then associate to each simulated IR source a line luminosity by sampling, at random, the distribution of values of $\log(L_\ell/L_{\mathrm{IR}})$ or of $\log(L_\ell)_{\mathrm{UL}}$, assumed to be Gaussian with mean value and dispersion given in Table 3.1. Similarly I associate a redshift to each object, assuming a uniform probability distribution within $z \pm (\Delta z/2)$. Finally the line flux, F_ℓ, is computed from the simulated redshift, z_{simul}, and the simulated line luminosity, $L_{\ell,\mathrm{simul}}$, as $F_{\ell,\mathrm{simul}} = L_{\ell,\mathrm{simul}}/4\pi d_{\mathrm{L}}^2(z_{\mathrm{simul}})$, $d_L(z)$ being the luminosity distance. The wavelength range covered by the instrument, $[\lambda_{\mathrm{min}}, \lambda_{\mathrm{max}}]$, and the line rest-frame wavelength, λ_ℓ, define the minimum and maximum redshift within which the line is detectable, $z_{\ell,\mathrm{min/max}} = \lambda_{\mathrm{min/max}}/\lambda_\ell - 1$. When z_{simul} falls outside the range defined by $z_{\ell,\mathrm{min}}$ and $z_{\ell,\mathrm{max}}$, the corresponding line luminosity and line flux are set to 0.

The simulated line luminosities are binned to produce the line luminosity functions at a given redshift. In order to reduce the effect of fluctuations in the highest luminosity bins, where the statistic is poorest, the whole procedure is repeated 300 times and the simulated luminosity functions are averaged together. The predicted number counts and redshift distributions are also derived by averaging over the 300 simulated catalogues.

In Fig. 3.4 I show, as an example, the effect of the dispersion on the predicted luminosity function for the [NeII]12.81μm line. Since dispersions are substantial, they result in a vast

---

[4] This value is chosen to ensure that all the galaxies detectable by SAFARI and CCAT are represented in the simulation while keeping the computing time, that depends on the total number of simulated sources, to an acceptable level.

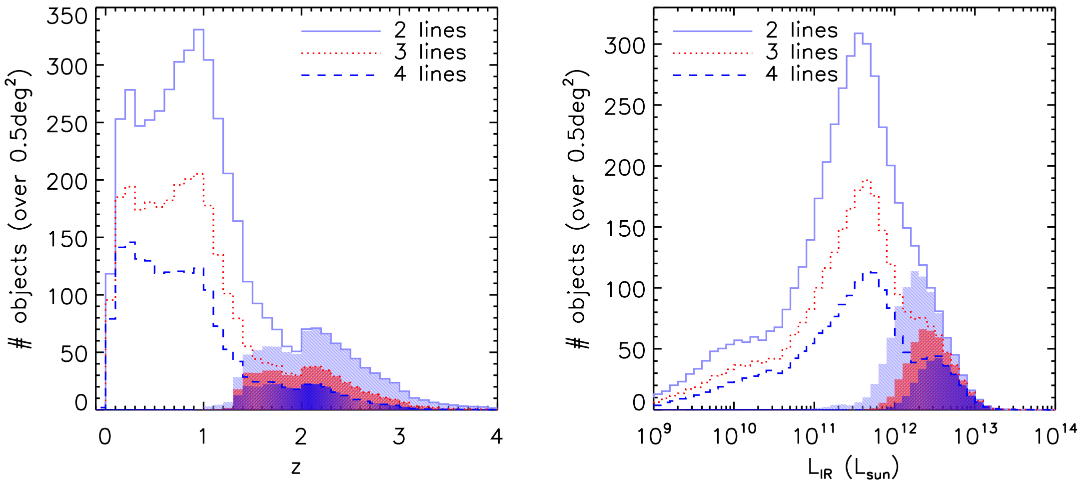

Figure 3.8: Predicted redshift (left) and luminosity (right) distributions of star-forming galaxies detectable in at least two (cyan solid histogram), three (red dotted) and four (blue dashed) spectral lines, by the reference survey with SPICA-SAFARI. The shaded areas represent the contributions of proto-spheroids.

Spectral line	0.00 – 0.75	0.75 – 1.25	1.25 – 1.75	1.75 – 2.25	2.25 – 2.75	2.75 – 4.00	4.00 – 6.00	All z
PAH11.25μm	0	0	0	378	597	548	83	1606
[NeII]12.81μm	0	0	47	146	75	49	4	321
[NeIII]15.55μm	0	8	46	21	9	5	0	89
$H_2$17.03μm	0	9	10	4	2	0	0	25
[SIII]18.71μm	0	195	108	48	26	12	1	390
[SIII]33.48μm	919	661	285	125	78	41	2	2111
[SiII]34.82μm	1222	957	436	191	117	64	2	2989
[OIII]51.81μm	1735	1490	1071	423	230	78	0	5027
[NIII]57.32μm	498	218	91	51	22	0	0	880
[OI]63.18μm	1082	879	378	163	17	0	0	2519
[OIII]88.36μm	1907	1611	325	0	0	0	0	3843
[NII]121.9μm	415	0	0	0	0	0	0	415
[OI]145.5μm	140	0	0	0	0	0	0	140
[CII]157.7μm	807	0	0	0	0	0	0	807

Table 3.2: Predicted redshift distributions of star-forming galaxies detectable by the SPICA-SAFARI reference survey (0.5 deg^2, 1 hr integration per FoV) in each of the 14 emission lines considered.

Spectral line	**Cai et al. (2013)**	Franceschini et al. (2010)	Gruppioni et al. (2011)	Valiante et al. (2009)
PAH11.25μm	**1606**	160	173	418
[NeII]12.81μm	**321**	333	203	42
[NeIII]15.55μm	**89**	129	122	179
$H_2$17.03μm	**25**	13	17	6
[SIII]18.71μm	**390**	74	67	6
[SIII]33.48μm	**2111**	1377	1059	1103
[SiII]34.82μm	**2989**	2535	2241	3037
[OIII]51.81μm	**5027**	1723	2081	3883
[NIII]57.32μm	**880**	276	665	973
[OI]63.18μm	**2519**	4171	5421	8897
[OIII]88.36μm	**3843**	2286	3027	5121

Table 3.3: Comparison of the number of $5\,\sigma$ detections in each line by SPICA-SAFARI according to the present model (second column, in boldface) with those for the 3 models used by Spinoglio et al. (2012). The predictions for the Franceschini et al. (2010) model (3^{rd} column) refer (as mine) to star-forming galaxies only, while those for the Gruppioni et al. (2011, 4^{th} column) and for the Valiante et al. (2009, 5^{th} column) model include also AGNs.

Spectral line	$0.75-1.25$	$1.25-1.75$	$1.75-2.25$	$2.25-2.75$	$2.75-4.00$	$4.00-6.00$	$6.00-8.00$	All z
[OIII]51.81μm	0	0	0	0	0	14	2	16 (1)
[OI]63.18μm	0	0	0	0	2	12	0	14 (0)
[OIII]88.36μm	0	0	0	328	701	197	2	1228 (0)
[NII]121.9μm	0	137	172	126	75	11	6	527 (0)
[OI]145.5μm	61	160	140	43	15	47	2	468 (2)
[CII]157.7μm	3379	3099	2865	50	679	2243	0	12315 (12)

Table 3.4: Predicted redshift distributions of star-forming galaxies detectable by CCAT over $1.0\,\mathrm{deg}^2$ with 1 hr integration per FoV in each of the emission lines within the CCAT wavelength range. In parenthesis I give the number of detections of strongly lensed galaxies at $z > 5$. No detections in the [NIII] 57.32 μm line are expected at the flux limits of this survey.

Spectral line	**Cai et al. (2013)**	Franceschini et al. (2010)	Gruppioni et al. (2011)	Valiante et al. (2009)
[OI]63.18μm	**7 (1)**	0	2	0
[OIII]88.36μm	**614 (515)**	133	182	278
[NII]121.9μm	**264 (255)**	29	54	92
[OI]145.5μm	**234 (210)**	1	5	2
[CII]157.7μm	**6158 (5036)**	4421	4683	6612

Table 3.5: Numbers of $5\,\sigma$ detections by CCAT for the survey considered by Spinoglio et al. (2012) (1 h integration per FoV over an area of $0.5\,\mathrm{deg}^2$) as predicted by the present model (second column, in boldface) compared with those given (only for 5 lines) by Spinoglio et al. (2012) for the 3 models used by them. The latter predictions include the contributions of AGNs and are limited to $z \leq 4$. For a fairer comparison I also give, in parenthesis, my predictions for the same redshift range.

Spectral line	$t = 6\,$min $5.00\,$deg^2	$t = 30\,$min $1.00\,$deg^2	$\boldsymbol{t = 1}\,$**h** **0.50** deg$^\mathbf{2}$	$t = 2\,$h $0.25\,$deg^2	$t = 3\,$h $0.17\,$deg^2	$t = 5\,$h $0.10\,$deg^2	$t = 10\,$h $0.05\,$deg^2
PAH11.25μm	3721 (709)	2124 (525)	**1606 (441)**	1180 (356)	977 (307)	765 (251)	536 (184)
[NeII]12.81μm	500 (31)	389 (34)	**321 (31)**	262 (31)	231 (30)	191 (26)	145 (22)
[NeIII]15.55μm	82 (0)	98 (2)	**89 (2)**	81 (3)	76 (3)	70 (3)	59 (3)
$H_2$17.03μm	19 (0)	19 (0)	**25 (0)**	24 (1)	23 (0)	24 (1)	22 (1)
[SIII]18.71μm	497 (9)	453 (8)	**390 (9)**	334 (9)	297 (10)	248 (8)	191 (7)
[SIII]33.48μm	3773 (11)	2634 (27)	**2111 (24)**	1617 (28)	1355 (25)	1066 (24)	748 (22)
[SiII]34.82μm	5862 (30)	3863 (36)	**2989 (39)**	2232 (39)	1842 (38)	1422 (35)	978 (31)
[OIII]51.81μm	14003 (12)	7054 (14)	**5027 (12)**	3488 (9)	2785 (7)	2072 (6)	1378 (5)
[NIII]57.32μm	971 (0)	953 (0)	**880 (0)**	754 (0)	678 (0)	572 (0)	434 (0)
[OI]63.18μm	4376 (0)	3181 (0)	**2519 (0)**	1891 (0)	1568 (0)	1209 (0)	826 (0)
[OIII]88.36μm	12391 (0)	5661 (0)	**3843 (0)**	2554 (0)	1996 (0)	1452 (0)	930 (0)
[NII]121.9μm	886 (0)	548 (0)	**415 (0)**	308 (0)	252 (0)	195 (0)	132 (0)
[OI]145.5μm	322 (0)	187 (0)	**140 (0)**	102 (0)	83 (0)	64 (0)	44 (0)
[CII]157.7μm	3276 (0)	1247 (0)	**807 (0)**	515 (0)	397 (0)	280 (0)	175 (0)

Table 3.6: Number of star-forming galaxies detectable by a SPICA-SAFARI survey of 450 hours covering different areas, with correspondingly different integration times (t) per FoV. In parenthesis I give the number of detections at $z > 3$.

increase, compared to the case without dispersion, of the density of the most luminous sources and, correspondingly, of the bright portion of source counts.

The integral counts predicted by my reference model in the SPICA-SAFARI wavelength range, for all the 14 lines considered, are shown in Fig. 3.5.

According to B. Sibthorpe (private communication), the SPICA-SAFARI reference 5σ detection limits for an integration of 1 hr per FoV are $3.7 \times 10^{-19}\,$W/m^2 for the first band ($34 - 60\,\mu$m), $3.4 \times 10^{-19}\,$W/m^2 for the second band ($60 - 110\,\mu$m) and $2.9 \times 10^{-19}\,$W/m^2 for the third band ($110 - 210\,\mu$m). The predicted numbers of sources brighter than these limits in each line, detected by the survey considered by Spinoglio et al. (2012), covering $0.5\,$deg^2 (hereafter in chap. 3 the 'reference survey') are given in the last column of Table 3.2. The other columns detail the redshift distributions of detected sources. Examples of such redshift distributions are displayed, for 4 lines, in Fig. 3.6, where the redshift ranges covered by the different bands are identified by different colours. Obviously, only the shortest wavelength lines can be detected up to very high redshifts. According to my model, the reference survey can detect the PAH 11.25 μm line in some galaxies at redshifts up to $\simeq 6$. With the exception of 3 lines ([NeIII] 15.55 μm, H_2 17.03 μm, [SIII] 18.71 μm) out of 14 the slope of the SPICA-SAFARI integral counts, just below the mean of the detection limits of the three bands, of the reference survey is < 2 so that the number of detections for given observing time increases more with the surveyed area than with survey depth. And also for these three lines, the slope flattens below 2 not far from these limit.

Figure 3.7 shows the contributions to the counts for the 4 lines in Fig. 3.6 of late-type (spiral plus starburst) galaxies and of proto-spheroids, lensed and unlensed. At the 5σ SPICA-SAFARI limits for 1 hr exposure I expect the detection of the PAH 11.25 μm of ~ 60 strongly lensed proto-spheroids per square degree. Figure 3.8 illustrates the luminosity and redshift distributions of sources for which the SPICA-SAFARI reference survey will detect at least 2, 3 or 4 lines. From my reference model I expect about 4600 sources detected by the SPICA-SAFARI reference survey in at least 2 lines, about 2800 in at least 3 lines and about 1800 in at least 4 lines. The numbers of proto-spheroids among these are about 900, 460 and 270, respectively.

Figure 3.9 compares the present predictions for the redshift distributions of sources detected by the SPICA-SAFARI reference survey in 11 lines with those from the 3 models used by Spinoglio et al. (2012). The main differences concern the PAH 11.25 μm and [SIII] 18.71 μm lines, for which my predictions are substantially higher than those from all the other models, the [NeII] 12.81 μm line, for which my predictions are considerably lower in the redshift bin $1.25 < z < 1.75$ and higher at larger redshifts, and the [NeIII] 15.55 μm and H_2 17.03 μm lines in some redshift bins. Apart from these cases, most differences are within a factor ~ 2.

In Table 3.3 the comparison with Spinoglio et al. (2012) is made in terms of the total number of $\geq 5\,\sigma$ detections. Again, differences are generally within a factor of 2, but can be much larger, in particular, again, for the PAH 11.25 μm and [SIII] 18.71 μm lines.

In the case of CCAT, the 5σ detection limits for an integration of 1 hour per FoV (reference detection limits) are (Glenn, 2012) $1.6\times10^{-19}\,\mathrm{W/m^2}$ for the first band ($312.3-380.9\,\mu$m), $9.5\times10^{-20}\,\mathrm{W/m^2}$ for the second band ($416.4-499.7\,\mu$m), $1.1\times10^{-19}\,\mathrm{W/m^2}$ for the third band ($587.8-648.9\,\mu$m) and $1.6\times10^{-20}\,\mathrm{W/m^2}$ for the fourth band ($803.7-1102.2\,\mu$m). The integral counts in the CCAT wavelength range for the 7 lines within the SPICA-SAFARI range, are shown in Fig. 3.12.

The slopes of the CCAT integral counts just below the detection limits of the reference detection limits for the bands giving the largest contributions are <2 for 5 out of 7 of the considered lines (the 2 exceptions are the [NIII] $57.32\,\mu$m and [OI] $63.18\,\mu$m lines), implying that the number of detections for given observing time increases more with the surveyed area than with survey depth. The predicted redshift distributions of galaxies detectable over $1\,\mathrm{deg}^2$ with 1 h integration per FoV in each of the 7 emission lines are presented in Table 3.4. The predictions range from 14 to more than $12,000$ (in the [CII]157.7μm line) sources. In the latter line, such CCAT survey will be able to detect, in the redshift interval $5<z<6$, about 490 unlensed and 12 strongly lensed proto-spheroidal galaxies. Some 12 galaxies in the range $6<z<8$ should be detected in other lines. Thus a CCAT survey of a few hours will provide a good grasp of the early dust-obscured phase of galaxy formation up to the re-ionization epoch.

Figure 3.13 shows that the redshift distributions predicted by my reference model for the CCAT survey considered by Spinoglio et al. (2012, exposure time: 1 h per FoV; area: $0.5\,\mathrm{deg}^2$) in the 5 lines for which results are also presented by Spinoglio et al. (2012) are widely different from those implied by the 3 models used in the latter paper. The differences, arising from those in the model luminosity functions at $z\geq3$ and in the relationships between line and IR luminosities, are much larger than found for the SPICA-SAFARI reference survey, except for the [CII]157.7μm line. These large differences are reflected in the comparison in terms of the total number of detections by the reference survey (Table 3.5).

3.3 Observing strategy

Table 3.6 shows how the number of SPICA-SAFARI detections is maximized at fixed observing time (450 hours). The number of detections steadily decreases with increasing integration time per FoV (and correspondingly decreasing the surveyed area), except for a couple of lines ([NeIII]15.55 μm and $H_2$17.03 μm) for which however the number of detections is only weakly varying. This is because, as noted above, the slope of the counts below the detection limits of the reference survey is relatively flat. Going deeper is only marginally advantageous even for the detection of the highest z galaxies (see, for example, the variation with survey depth of the number of objects at $z > 3$, given in parenthesis).

The number of galaxies detected in two or more lines by the reference survey is reported at the bottom of Tab. 3.7 for late-type galaxies (second column) and proto-spheroids (third column; with the number of $z > 3$ detections indicated in parenthesis). Also shown in the table is the number of detections in each spectral line for objects detected in at least two lines (i.e. each of the thousands of galaxies seen in e.g. [OIII]51.81μm is also detected in one or more of the lines listed in the same table). The brightest lines, which provide the highest number of detections, are [SIII]33.48μm, [SiII]34.82μm, [OIII]51.81μm, [OI]63.18μm, [OIII]88.36μm and [NII]121.9μm. These lines will represent the most useful redshift indicators and the most easily available probes of the physical conditions in star-forming galaxies detected by SAFARI. The redshift distribution of galaxies detected in at least two lines in the reference spectroscopic survey is shown by the blue histogram in Fig. 3.10. The majority of galaxies have $z \lesssim 2$ with only ~ 70 detections above $z = 3$. The way to increase the statistics of high redshift galaxies is to improve the line sensitiviy by means of longer integration time per FoV. The effect is illustrated by the black dashed

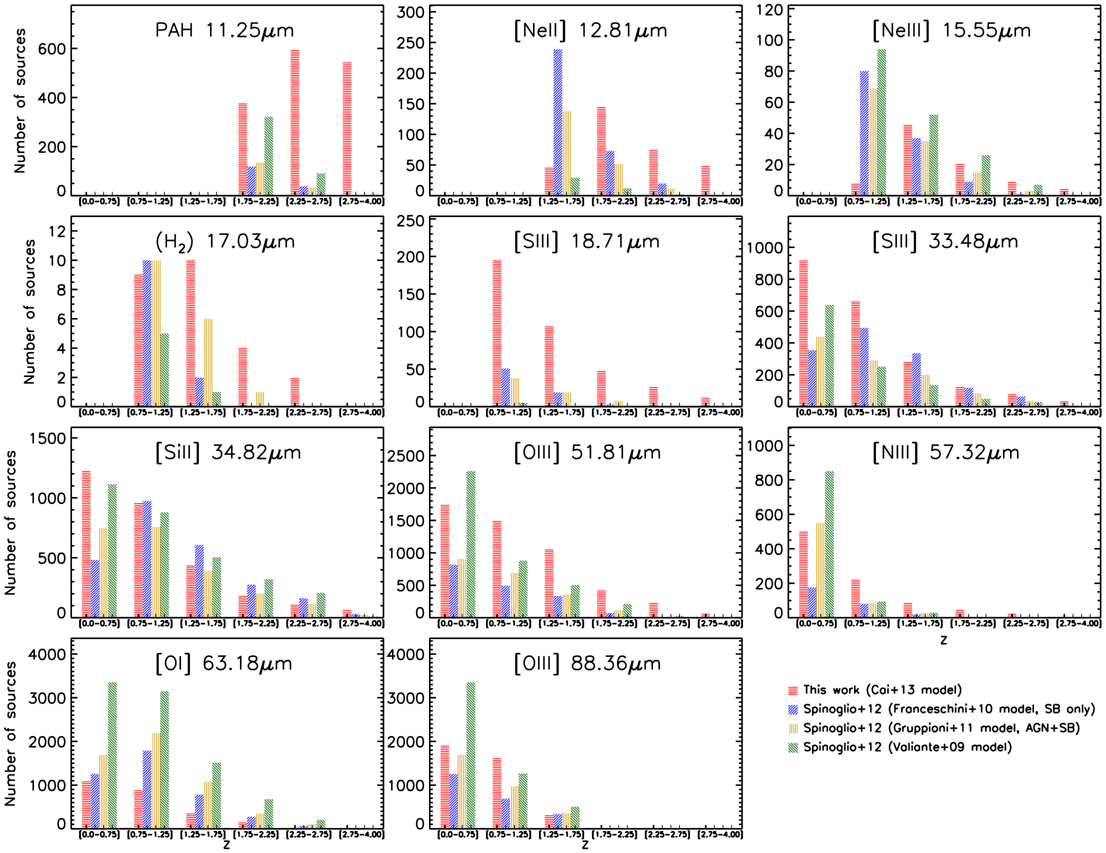

Figure 3.9: Redshift distributions of galaxies detectable in 11 lines by the SPICA-SAFARI reference survey. The predictions of my reference model (bars with red horizontal dashes) are compared with those of the 3 models used by Spinoglio et al. (2012); see the legend on the bottom right.

Spectral line	1 hour per FoV		4 hours per FoV		9 hours per FoV	
	late-type	proto-sph.	late-type	proto-sph.	late-type	proto-sph.
PAH 11.25μm	1	508	15	1207	39	1922
[NeII]12.81μm	12	242	60	612	148	1000
[NeIII]15.55μm	25	60	102	176	214	314
(H_2)17.03μm	11	11	45	48	102	95
[SIII]18.71μm	220	125	647	340	1101	583
[SIII]33.48μm	1591	334	3571	885	5253	1462
[SiII]34.82μm	2187	479	4615	1198	6623	1969
[OIII]51.81μm	2638	610	5238	1395	7370	2186
[NIII]57.32μm	728	139	2086	383	3437	650
[OI]63.18μm	2010	307	4403	714	6363	1117
[OIII]88.36μm	2545	27	4755	108	6404	238
[NII]121.9μm	410	0	860	0	1252	0
[OI]145.5μm	137	0	281	0	412	0
[CII]157.7μm	625	0	1032	0	1361	0
≥ 2 lines	3649	899 (66)	6932	2094 (225)	9489	3332 (434)

Table 3.7: Number of late-type galaxies and of proto-spheroids *detected in two or more lines* (i.e. the line considered plus at least another one) by a SPICA-SAFARI survey covering 0.5 deg^2 in 1 hr integration per FoV (2nd and 3rd columns), in 4 hr integration per FoV (4th and 5th columns) and in 9 hr integration per FoV (6th and 7th columns). The total number of objects detected in at least two lines (regardless of which lines are actually detected) is shown in the last line, while the value in parentheses represents the subsample of proto-spheroids with redshift $z > 3$.

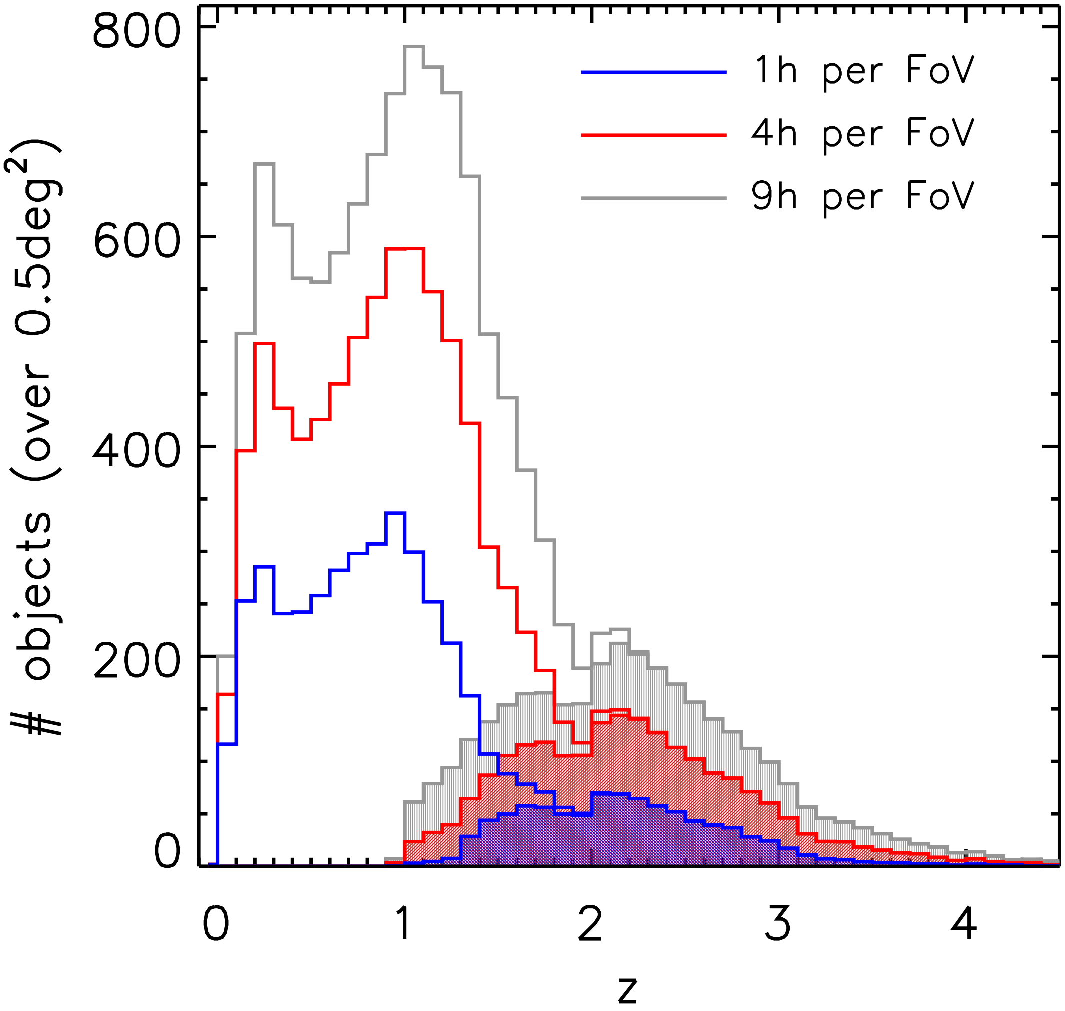

Figure 3.10: Number of star-forming galaxies detected in 2 or more lines in a spectroscopic survey of 0.5 deg^2 with SPICA-SAFARI for 1 hr integration per FoV (blue line), 4 hr integration per FoV (red line) and 9 hr integration per FoV (green line). The shaded histograms show the contribution of proto-spheroids.

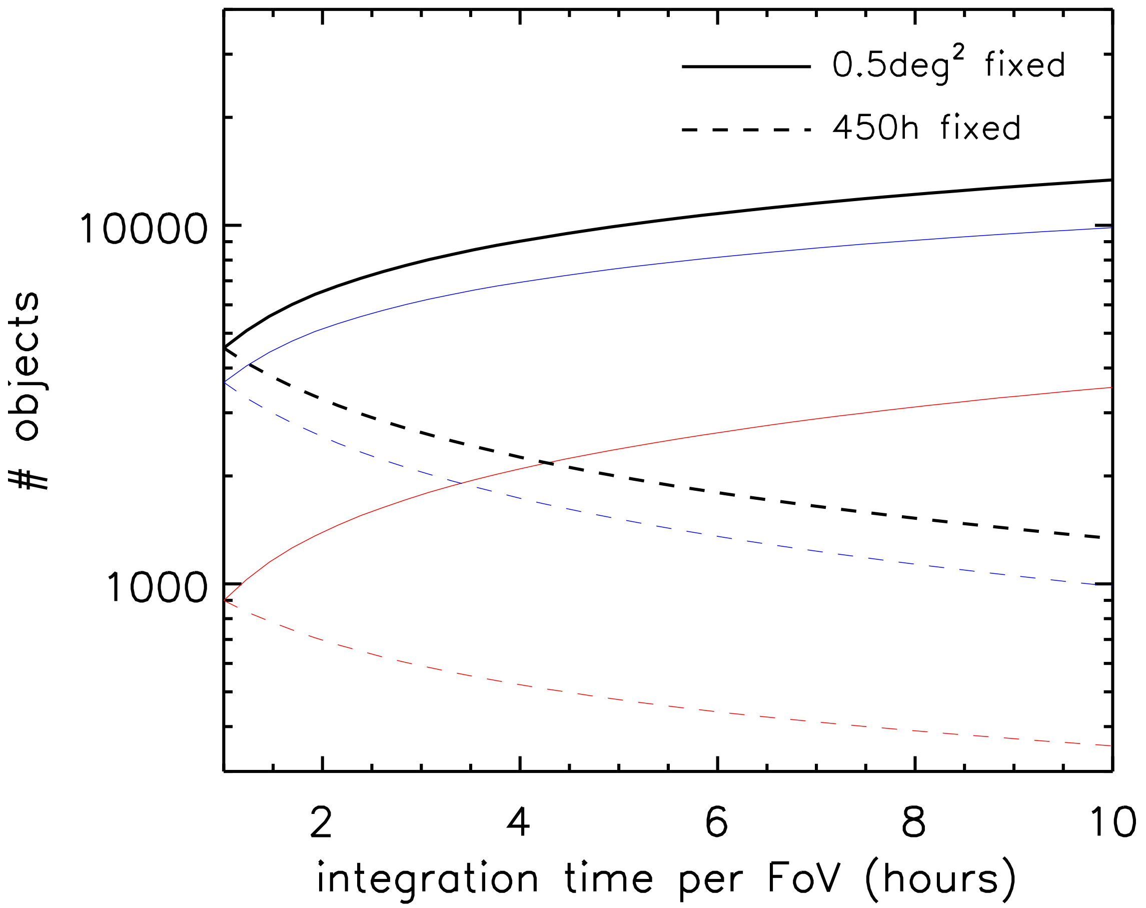

Figure 3.11: Number of star-forming galaxies (black curves) detected in 2 or more lines as a function of the integration time per FoV for a SPICA-SAFARI spectroscopic survey of 0.5 deg^2 (solid curves) and of 450 hours (dashed curves). The contributions of late-type galaxies and of proto-spheroids are shown in blue and in red, respectively.

line in Fig. 3.11, where the number of galaxies detected in two or more lines is shown as a function of $t_{\rm FoV}$. As the integration time per FoV increases, the line sensitivy decreases by a factor $\sqrt{t_{\rm FoV}}$ while the area is scaled down by a factor $1/t_{\rm FoV}$. The net effect is the loss of statistics as the decreasing number of detections due to the smaller areal coverage is not overcame by the increasing number density of galaxies. In fact, around the faintest line fluxes probed by SAFARI, the line integral number counts have slope $\gamma \sim 1$ (with $N(> F_\ell) \propto F_\ell^{-\gamma}$, where F_ℓ is the line flux).

Alternatively, one can keep the area to $0.5\,\mathrm{deg}^2$ and just increase the amount of time invested in the survey. The result of this approach is shown by the solid lines in Fig. 3.11, and also reported in Tab. 3.7 for an $t_{\rm FoV} = 4\,$hours and $t_{\rm FoV} = 9\,$hours per FoV. The corresponding redshift distributions are shown in Fig. 3.10. I find that improving the line sensitivity by a factor of 3 (i.e. $t_{\rm FoV} = 9\,$hours) will gain about ×6 more galaxies detected in at least two lines at $z > 3$ compared to what expected for the reference survey. However this would require an investment of 4050 hours for the entire survey.

The statistics of objects at $z \geq 3$ detected by the SPICA-SAFARI reference survey is quite poor. So, in order to investigate the star formation activity at high-z, it is expedient to complement the blind spectroscopic survey with follow-up observations of the high-z galaxies already discovered at (sub-)mm wavelengths over much larger areas. Figure 3.14 shows, as an example, the SPICA-SAFARI exposure time per FoV necessary for a 5σ detection of lines detectable at $z = 3$ and $z = 4$ as a function of the IR luminosity. At these redshifts an exposure time of 10 h will allow the detection in two lines of all the galaxies detected in the *Herschel*/PACS and SPIRE surveys used by Gruppioni et al. (2013) to derive the IR luminosity functions. A similar conclusion also holds at $z = 2$. Note that only a small fraction of galaxies at $z \geq 2$ detected in these surveys have spectroscopic redshifts. Moreover, when SPT and *Herschel* survey data will be fully available we will have samples of many hundreds of bright strongly lensed galaxies (apparent luminosities

Spectral line	$t = 1\,\mathrm{h}$ $1000\,\mathrm{deg}^2$	$t = 10\,\mathrm{h}$ $100\,\mathrm{deg}^2$	$t = 100\,\mathrm{h}$ $10\,\mathrm{deg}^2$	$t = 1000\,\mathrm{h}$ $1\,\mathrm{deg}^2$
[OIII]51.81μm	1.63×10^4 (1.63×10^4)	1.18×10^4 (1.18×10^4)	4819(4819)	1140(1140)
[NIII]57.32μm	76(76)	992(992)	1541(1541)	1063(1063)
[OI]63.18μm	1.45×10^4 (1.45×10^4)	2.04×10^4 (2.04×10^4)	1.26×10^4 (1.26×10^4)	4011 (4011)
[OIII]88.36μm	1.23×10^6 (6.26×10^5)	4.20×10^5 (2.29×10^5)	1.08×10^5 (5.98×10^4)	2.01×10^4 (1.10×10^4)
[NII]121.9μm	5.27×10^5 (3.29×10^4)	2.57×10^5 (2.57×10^4)	9.16×10^4 (1.13×10^4)	2.41×10^4 (3054)
[OI]145.5μm	4.68×10^5 (6.55×10^4)	2.56×10^5 (4.33×10^4)	9.16×10^4 (1.66×10^4)	2.40×10^4 (4270)
[CII]157.7μm	1.23×10^7 (2.42×10^6)	3.04×10^6 (5.39×10^5)	6.09×10^5 (8.19×10^4)	1.09×10^5 (1.00×10^4)

Table 3.8: Numbers of star-forming galaxies detectable by CCAT surveys of 1000 h covering areas from $1000\,\mathrm{deg}^2$ to $1\,\mathrm{deg}^2$ with integration times per FoV correspondingly ranging from 1 to 1000 h, assuming the goal FoV of $1\,\mathrm{deg}^2$. The numbers of galaxies at $z > 3$ are given in parenthesis.

$L_{\rm IR} > 10^{13}\,L_\odot$; Negrello et al., 2010; Vieira et al., 2013), that can be detected in few minutes in several lines by SPICA-SAFARI.

Also for CCAT, at fixed observing time, it is generally more advantageous to cover larger areas than to go deeper, even to detect high-z galaxies, as shown by Table 3.8. The exception is the [NIII]57.32 μm line, whose counts keep a slope larger than 2 down to fluxes corresponding to exposure times of a few hundred hours.

A CCAT survey of 1000 hours, covering $1000\,\mathrm{deg}^2$ in 1 hour integration, will be able to detect 1.3×10^7 (2.9×10^6 at $z > 3$) star-forming galaxies in at least one spectral line, 9.1×10^5 (2.6×10^5 at $z > 3$) in at least two lines and 8.8×10^4 (2.6×10^4 at $z > 3$) in at least three lines. The number of strongly lensed proto-spheroidal galaxies detectable by the same CCAT survey in at least one line is 1.1×10^5 (6.7×10^4 at $z > 3$), in at least two lines 2.0×10^4 (1.3×10^4 at $z > 3$) and in at least three lines 4110 (2750 at $z > 3$).

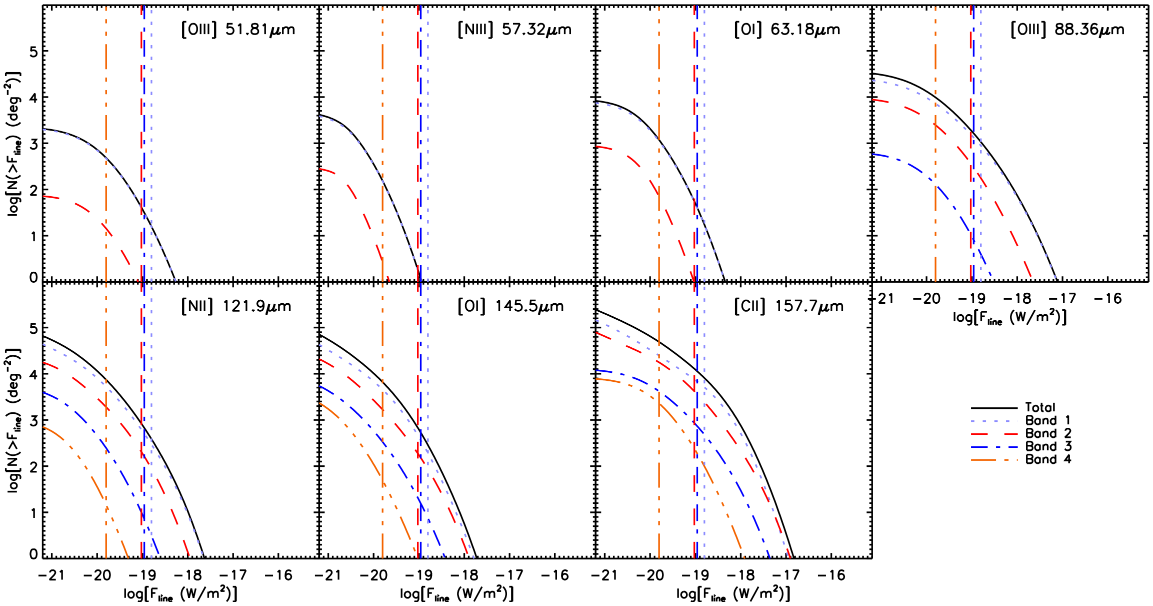

Figure 3.12: Integral counts of star-forming galaxies as a function of line fluxes over the full CCAT wavelength range (black solid line) and in each of its four bands. The vertical lines correspond to the detection limits in the four bands for 1 hour integration per FoV.

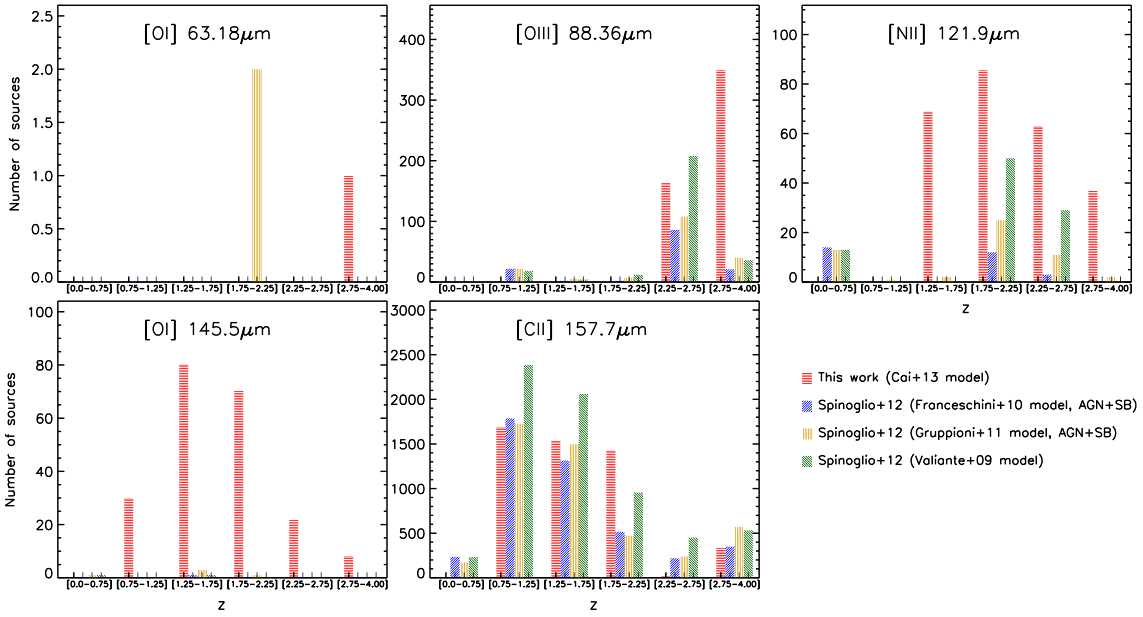

Figure 3.13: Redshift distributions of galaxies detectable in 5 lines by the CCAT survey considered by Spinoglio et al. (2012, exposure time: 1 h per FoV; area: $0.5\,\mathrm{deg}^2$). The predictions of my reference model (bars with red horizontal dashes) are compared with those of the 3 models used by Spinoglio et al. (2012); see the legend on the bottom right.

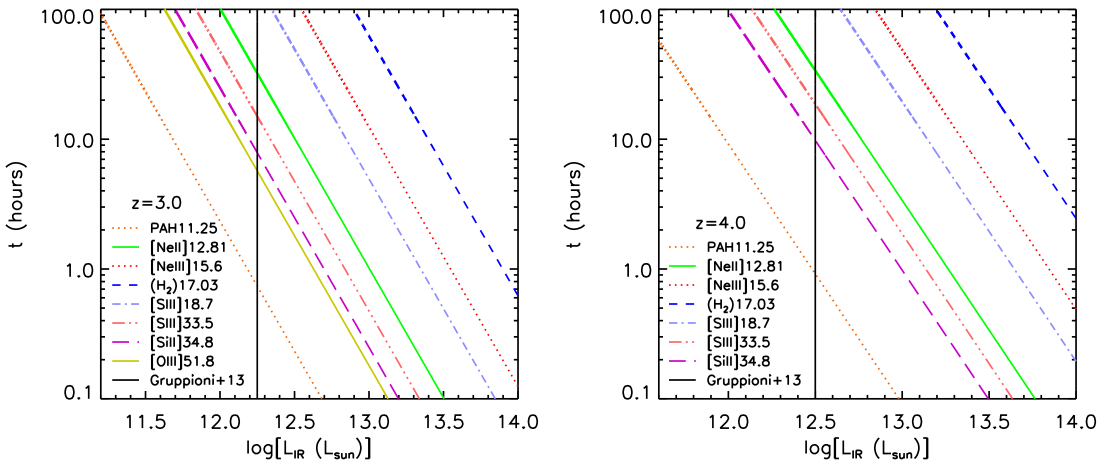

Figure 3.14: SPICA-SAFARI exposure time per FoV required for a 5σ line detection (see legend inside each panel) as a function of IR luminosity for galaxies at $z = 3$ (left) and $z = 4$ (right). The vertical solid lines correspond to the minimum luminosities represented in the IR luminosity functions determined by Gruppioni et al. (2013) on the basis of *Herschel*/PACS and SPIRE surveys.

Chapter 4

Exploring the relationship between black hole accretion and star formation with SPICA-SAFARI

The MIR lines that will be detected can come either from star-forming regions or from nuclear activity or from both. Distinguishing the two contributions is not easy. However a key diagnostic relies on the fact that AGNs produce harder radiation and therefore excite metals to higher ionization states than starbursts. Thus lines with high-ionization potential are a powerful tool for identifying AGN activity (Sturm et al., 2002; Meléndez et al., 2008; Satyapal et al., 2008, 2009; Goulding & Alexander, 2009; Dudik et al., 2009; Weaver et al., 2010) that is easily missed by optical spectroscopic observations in the case of dusty objects, as galaxies with intense star formation are.

So far these studies have been limited to local objects. Substantial progress in this area will be made possible by spectroscopy with SAFARI that will exploit for the first time the rich suite of mid- and far-IR diagnostic lines to trace the star formation and the accretion onto the super-massive black holes up to high redshifts through both blind spectroscopic surveys and pointed observations.

I present a new approach to the problem of the connection between star formation and AGN activity, taking advantage of the physical model for the co-evolution of super-massive black holes and massive proto-spheroidal galaxies at high redshift ($z \geq 1.5$) worked out by Cai et al. (2013) who presented the evolving luminosity functions of these objects as a whole (starburst plus AGN), taking into account in a self-consistent way the variation with galactic age of the global spectral energy distribution.

The physical model was complemented by a phenomenological model for lower z AGNs and star-forming galaxies, mostly late-type since massive spheroidal galaxies are observed to be in essentially passive evolution at $z \lesssim 1$–1.5. In this case galaxies and AGNs were evolved separately. I combined the two components exploiting the average accretion rate as a function of the SFR derived by Chen et al. (2013), taking into account its dispersion. Bright optically selected QSOs, that do not obey such correlation, were taken into account adopting the best fit evolutionary model by Croom et al. (2009) up to $z = 2$.

The plan of this chapter is the following. In par. 4.1 I present the adopted model for the evolution with cosmic time of the IR (8-1000 μm) luminosity function. In par. 4.2 I discuss the relations between line and continuum luminosity for the main mid/far-IR lines. In par. 4.3 I work out our predictions for line luminosity functions, number counts and redshift distributions in the SPICA/SAFARI bands. In par. 4.4 I compare our results with previous estimates. In par. 4.5 I discuss possible SPICA/SAFARI observation strategies, considering different integration times per FoV.

4.1 Evolution of the IR luminosity functions

As explained in par. 2.1 my reference model for the redshift-dependent IR luminosity functions is the one worked out by Cai et al. (2013) based on a comprehensive “hybrid” approach combining a physical model for the progenitors of early-type galaxies with a

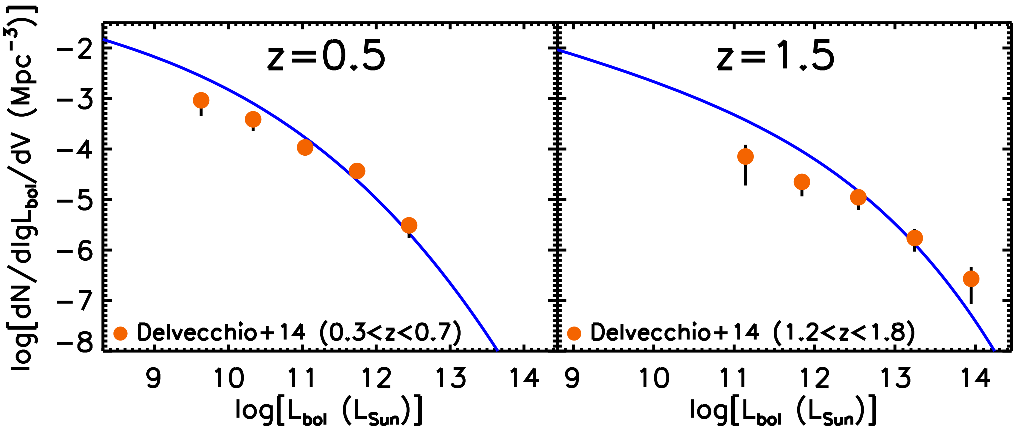

Figure 4.1: Comparison of the AGN bolometric luminosity functions at $z = 0.5$ and $z = 1.5$ yielded by my approach (solid lines) with the observational estimates by Delvecchio et al. (2014). The dotted red curve in the right-hand panel shows the contribution of strongly lensed (amplification $\mu \geq 2$) sources; at $z = 0.5$ such contribution is negligible. The vertical lines correspond to the minimum bolometric luminosity yielding a detection by SAFARI of the strongest AGN line ([OIV] 25.89μm) with exposures of 1 and 10 hr/FoV (solid and dotted, respectively), for the mean line to bolometric luminosity ratios.

phenomenological one for late-types.

According to Cai et al. (2013) the redshift dependent luminosity functions of proto-spheroids as a whole, $\Phi(L_{\rm tot}, z)$, writes:

$$\begin{aligned}\Phi(L_{\rm tot}, z) &= \int_{M{\rm min}}^{M_{\rm max}} dM_{\rm vir} \int_{z}^{z_{\rm max}} dz_{\rm vir} \left|\frac{dt_{\rm vir}}{dz_{\rm vir}}\right| \\ &\times \frac{dN_{ST}}{dt_{\rm vir}}(M_{\rm vir}, z_{\rm vir}) \int_{-\infty}^{\log L_{\rm tot}} \frac{dx}{2\pi\sigma_*\sigma_\bullet} \\ &\times \frac{L_{\rm tot}}{L_{\rm tot} - 10^x} \exp\left[-(x - \log \bar{L_*})^2/2\sigma_*^2\right] \\ &\times \exp\left[-[\log(L_{\rm tot} - 10^x) - \bar{L_\bullet}]^2/2\sigma_\bullet^2\right] \qquad (4.1)\end{aligned}$$

where $\bar{L_*} = \bar{L_*}(z|M_{\rm vir}, z_{\rm vir})$ and $\bar{L_\bullet} = \bar{L_\bullet}(z|M_{\rm vir}, z_{\rm vir})$ are the redshift-dependent mean starburst and AGN luminosities at given halo mass, $M_{\rm vir}$, and virialization redshift, $z_{\rm vir}$, respectively, and σ_* and $\sigma_\bullet$ are the corresponding dispersions. dN_{ST}/dt is the dark matter halo mass function (Sheth & Tormen, 1999).

The conditional luminosity function of the starburst component, $\Phi_*(L_*|L_{\rm tot}, z)$, i.e. the number density of sources at redshift z with starburst luminosity L_* given that the total luminosity is $L_{\rm tot}$, writes

$$\begin{aligned}
&\Phi_*(L_*|L_{\rm tot}, z) d\log L_* = \int_{M{\rm min}}^{M_{\rm max}} dM_{\rm vir} \\
&\times \int_z^{z_{\rm max}} dz_{\rm vir} \left|\frac{dt_{\rm vir}}{dz_{\rm vir}}\right| \frac{dN_{ST}}{dt_{\rm vir}}(M_{\rm vir}, z_{\rm vir}) \frac{d\log L_*}{2\pi\sigma_*\sigma_\bullet} \\
&\times \frac{L_{\rm tot}}{L_{\rm tot} - L_*} \exp\left[-(\log L_* - \log \bar{L_*})^2/2\sigma_*^2\right] \\
&\times \exp\left[-[\log(L_{\rm tot} - L_*) - \log \bar{L_\bullet}]^2/2\sigma_\bullet^2\right],
\end{aligned} \tag{4.2}$$

while the conditional luminosity function of the AGN component writes

$$\begin{aligned}
&\Phi_\bullet(L_\bullet|L_{\rm tot}, z) d\log L_\bullet = \int_{M{\rm min}}^{M_{\rm max}} dM_{\rm vir} \\
&\times \int_z^{z_{\rm max}} dz_{\rm vir} \left|\frac{dt_{\rm vir}}{dz_{\rm vir}}\right| \frac{dN_{ST}}{dt_{\rm vir}}(M_{\rm vir}, z_{\rm vir}) \frac{d\log L_\bullet}{2\pi\sigma_*\sigma_\bullet} \\
&\times \frac{L_{\rm tot}}{L_{\rm tot} - L_\bullet} \exp\left[-[\log(L_{\rm tot} - L_\bullet) - \log \bar{L_*}]^2/2\sigma_*^2\right] \\
&\times \exp\left[-[\log(L_\bullet - \log \bar{L_\bullet}]^2/2\sigma_\bullet^2\right].
\end{aligned} \tag{4.3}$$

The probability that an object at redshift z has a starburst luminosity L_* or an AGN luminosity $L_\bullet$ given the total luminosity of $L_{\rm tot} = L_* + L_\bullet$ is then:

$$P_*(L_*|L_{\rm tot}, z) d\log L_* \equiv \frac{\Phi_*(L_*|L_{\rm tot}, z) d\log L_*}{\Phi(L_{\rm tot}, z)}, \tag{4.4}$$

or

$$P_\bullet(L_\bullet|L_{\rm tot}, z) d\log L_\bullet \equiv \frac{\Phi_\bullet(L_\bullet|L_{\rm tot}, z) d\log L_\bullet}{\Phi(L_{\rm tot}, z)}. \tag{4.5}$$

The two probabilities have unit integral over the luminosity range 0–$L_{\rm tot}$ and are linked by the condition that, at fixed $L_{\rm tot}$, $P_*(L_*|L_{\rm tot}) = -P_\bullet(L_\bullet|L_{\rm tot})\,(d\log L_\bullet/d\log L_*)$ with $d\log L_\bullet/d\log L_* = d\log(L_{\rm tot} - L_*)/d\log L_* = -L_*/(L_{\rm tot} - L_*)$. Then

$$P_\bullet(L_\bullet|L_{\rm tot}) = \frac{L_\bullet}{L_{\rm tot} - L_\bullet} P_*(L_{\rm tot} - L_\bullet|L_{\rm tot}) \tag{4.6}$$

or

$$P_*(L_*|L_{\rm tot}) = \frac{L_*}{L_{\rm tot} - L_*} P_\bullet(L_{\rm tot} - L_*|L_{\rm tot}). \tag{4.7}$$

Each proto-spheroid of luminosity $L_{\rm tot}$ was assigned bolometric luminosities of the starburst and of the AGN components drawn at random from the above probability distributions, with the parameter values given by Cai et al. (2013). Note that for the starburst component the bolometric luminosity is very close to the IR (8–1000 μm) luminosity, but this is not the case for AGNs, especially for type-1's. For example, adopting the AGN SEDs used by Cai et al. (2013) I get $L_{\rm IR}/L_{\rm bol} = 0.189$ and 0.776 for type-1's, type-2's, respectively. This should be taken into account when comparing my results with those by Spinoglio et al. (2012) which rely on correlations between line and IR luminosity rather than between line and bolometric luminosity, as done here.

The model makes detailed predictions also for strongly gravitationally lensed galaxies. These objects are of special interest because strong lensing allows us to measure their total mass distribution up to very large distances and to gain information on sources too faint to be detected with current instrument sensitivities, thus testing models for galaxy formation and dark matter. To deal with them the probability distributions have been applied to the de-lensed luminosities. The de-lensing was made attributing to each lensed source an amplification factor randomly extracted from the amplification probability distributions by Negrello et al. (2007) and Lapi et al. (2012). After having done that, the luminosities of both component were re-amplified by the same factor.

As mentioned above, the evolution of late-type galaxies, the dominant star-forming population at $z \lesssim 1.5$, is described by a phenomenological, parametric model, distinguishing two sub-populations, “cold” (normal) and “warm” (starburst) galaxies. The AGNs associated to these populations are evolved independently, again with a phenomenological recipe. To combine galaxies and AGNs into sources including both components I have exploited the correlation between SFR and average black hole accretion rate derived by Chen et al. (2013) on the basis of a sample of 1767 far-IR selected galaxies in the redshift range $0.25 < z < 0.8$. Using their eq. (5), their bolometric correction for the AGN X-ray emission $L_{\rm bol}/L_{\rm X} = 22.4$, and their relationship between the IR luminosity of the starburst, $L_{\rm IR}$, and the SFR I got $\langle L_{\rm bol}/L_{\rm IR}\rangle = 0.054(L_{\rm IR}/10^{12}\,L_\odot)^{0.05}$.

It is also necessary to properly take into account the large dispersion around the mean relation. Such dispersion is difficult to evaluate because of the large fraction of galaxies in the Chen et al. (2013) sample for which only upper limits to the nuclear emission are available. I have estimated it by trial and error, looking for a value that yields redshift-dependent AGN luminosity functions consistent with the observational estimates by Delvecchio et al. (2014). In practice, I have carried out simulations associating to galaxies with a given $L_{\rm IR}$ an AGN with bolometric luminosity drawn at random from a Gaussian distribution with mean given by the average $L_{\rm bol}/L_{\rm IR}$ relation and several values of the dispersion. The contribution of optically selected AGNs (see below) was then added to the derived luminosity functions. I get consistency with the data (see a couple of examples in Fig. 4.1) with a dispersion of 0.69 dex, in agreement with the distribution of data points in Figs. 4.2 and 4.3 (taken from Chen et al. 2013). The fact that the model appears to over-estimate the low-luminosity tail of the AGN bolometric luminosity function is not worrisome for the present purposes since these sources are anyway too weak to be detectable by SPICA-SAFARI. It should also be noticed that the observational errors are purely statistical, i.e. do not include uncertainties on the decomposition of the observed spectral energy distribution to disentangle the AGN contribution from that of the host galaxy, on the bolometric correction, on the correction for incompleteness. These systematic errors increase with decreasing AGN luminosity. The evolution of sources as a whole is then driven by that of the SFR, as modeled by Cai et al. (2013).

Not all AGNs obey the accretion rate – SFR correlation. In particular, hosts of bright

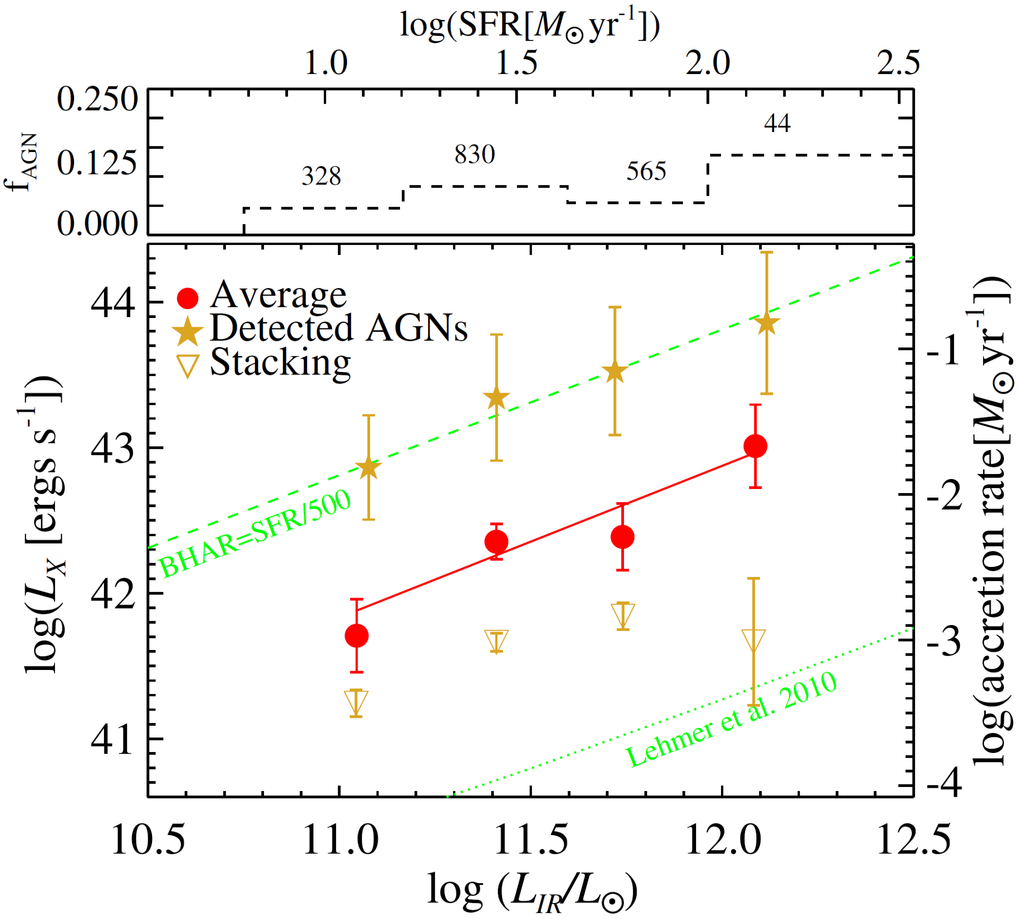

Figure 4.2: Relation between SFR and average supermassive black hole accretion rate (BHAR), calculated from the 8-1000μm L_{IR} and the 2-10keV L_X by Chen et al. (2013) (with their Equations 2 and 3) for their entire 250μm sample of 1767 galaxies (red circles). The X-ray stacking luminosity for the X-ray non-detections are shown as downward triangles and the X-ray/IRAC-selected AGNs are shown as stars. The sources are binned in approximately equal size SFR bins, with the vertical bars showing the errors from bootstrap re-sampling in each bin. The data points are plotted on the average LIR of each bin. The dashed green line on the top is $\dot{M}_{BH} = SFR/500$ and the dotted green line in the bottom is the Lehmer et al. (2010) SFR-L_X relation. In the top panel, are also presented the AGN detection fraction (f_{AGN}) with the total number of galaxies in each bin. The width of each bin in the histogram covers the SFR range in the bin. This figure shows that the average BHAR is strongly correlated with the SFR in all rapidly star-forming galaxies. (From Chen et al. 2013).

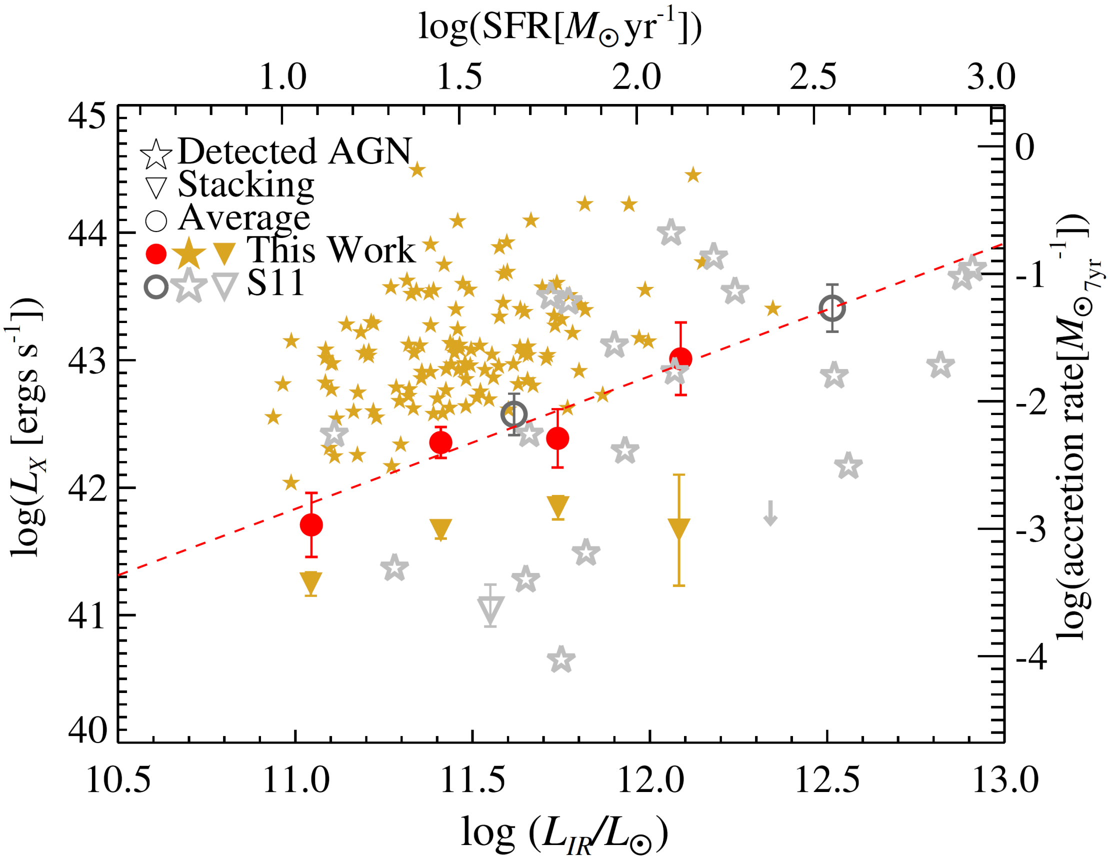

Figure 4.3: Comparison of Chen et al. (2013) result (filled symbols) to the SPIRE-selected, $z \sim 1$ sample in the CDF-N field (Symeonidis et al. 2011, open symbols), which is covered by a much deeper, pencil-beam-sized field. The L_{IR}-L_X correlation obtained by Chen et al. (2013) is shown as the dashed line. This comparison shows that even though the correlation between the L_X and L_{IR} for identified AGNs. (From Chen et al. 2013).

optically selected QSOs, with high accretion rates, are found to have SFRs ranging from very low to moderate, particularly at relatively low redshifts (Schweitzer et al., 2006; Netzer et al., 2007). These objects were taken into account adopting the best fit evolutionary model by Croom et al. (2009) up to $z = 2$ since at higher redshifts the abundance of AGNs associated to late-type galaxies is negligible compared to that of AGNs associated to proto-spheroids whose evolution up to the optically bright phase is described by the Cai et al. (2013) physical model.

The consistency between the model and the observed bolometric luminosity functions, illustrated by Fig. 4.1 for $z \leq 1.5$ and demostrated by Cai et al. (2013) at higher z, is crucial for the reliability of the derived line luminosity functions because they are calculated coupling the bolometric luminosity functions with the relations between line and bolometric luminosities (see par. 4.2).

In summary, the different IR galaxy populations considered here are:

- proto-spheroidal galaxies (unlensed and lensed), the progenitors of early-type galaxies and the dominant star-forming population at $z \gtrsim 1.5$, whose evolution is described by the physical model by Cai et al. (2013);
- AGNs associated to proto-spheroids whose co-evolution with the host galaxies is self-consistently built in the Cai et al. (2013) physical model;
- late-type galaxies, the dominant star-forming population at $z \lesssim 1.5$, divided into two sub-populations (spiral and starburst galaxies), whose evolution is described by the Cai et al. (2013) phenomenological model;
- type-1 and type-2 AGNs associated to late-type galaxies, whose evolution is linked to that of host galaxies via the Chen et al. (2013) accretion rate – SFR correlation;

- optical AGNs, whose evolution is described by the Croom et al. (2009) best-fit model up to $z = 2$ and included in the Cai et al. (2013) physical model at higher z.

While referring to the Cai et al. (2013) paper for full details, I summarize here, for the sake of clarity, a few points. Proto-spheroidal galaxies and massive bulges of disk galaxies are assumed to *virialize* at $z \geq 1.5$ but their evolution is followed down to $z = 0$. Their lifetimes in the star formation phase increase with decreasing halo mass, consistent with the observed "downsizing", from $\simeq 0.7\,$Gyr for the most massive ones to a few Gyr for the least massive. Hence they are contributing to the IR luminosity functions also at $z < 1.5$, but their contribution decreases with decreasing z. At $z < 1.5$ late-type galaxies take over them as the dominant contributors. The phenomenological model describing their evolution includes a smooth decline of their space density above $z \simeq 1.5$ but their contribution to the global IR luminosity function is still significant up to $z \simeq 2$.

The evolution of supermassive black holes associated to proto-spheroidal galaxies is followed by the physical model *only* during their active star formation phase when black holes acquire most of their mass. In other words the present implementation of the physical model is unable to follow the later AGN evolution when spheroids are in essentially passive evolution and nuclei can be reactivated by, e.g., interactions, mergers, or dynamical instabilities, especially if they acquire a disk, i.e. become the bulges of later-type galaxies. These later phases are dealt with by the phenomenological model, as described above.

4.2 Line versus IR luminosity

IR lines excited by star formation activity have been dealt with in chap. 3, with an analysis of the relations between line and starburst IR luminosities that considered differences among source populations and that was supported by extensive simulations taking into account dust obscuration. Here I complement the study considering the brightest lines that

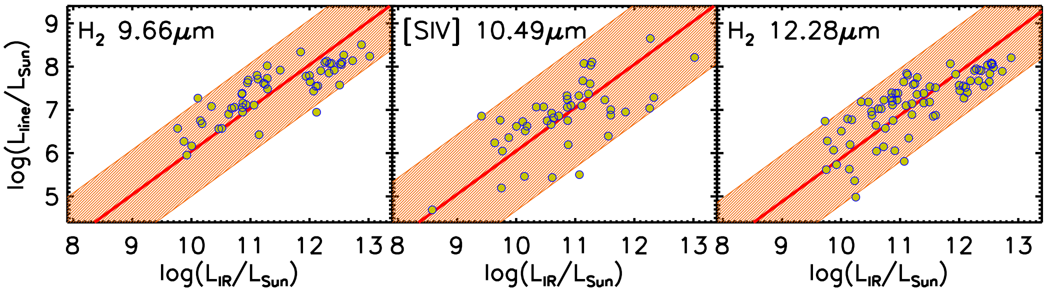

Figure 4.4: Line luminosity as a function of the IR luminosity of the starburst component for the $(H_2)9.66\mu$m, [SIV]10.49μm and $(H_2)12.28\mu$m lines. Luminosities are in solar units. Data from Roussel et al. (2006); Farrah et al. (2007); Bernard-Salas et al. (2009); Hao et al. (2009); O'Dowd et al. (2009, 2011); Pereira-Santaella et al. (2010); Cormier et al. (2012), excluding all objects for which there is evidence of a substantial AGN contribution. The orange bands show the $2\,\sigma$ spread around the mean linear relations (red lines) in the log–log plane. The mean ratios $\langle\log(L_\ell/L_{\rm IR})\rangle$ and the dispersions around them are given in Table 4.1.

Spectral line	$\langle \log\left(\frac{L_\ell}{L_{\rm IR}}\right)\rangle$ (σ)
PAH6.2μm	-2.20 (0.36)
PAH7.7μm	-1.64 (0.36)
PAH8.6μm	-2.16 (0.36)
$H_2$9.66μm	-3.96 (0.52)
[SIV]10.49μm	-3.95 (0.69)
$H_2$12.28μm	-4.12 (0.54)
[NeII]12.81μm	-3.11 (0.45)
[NeIII]15.55μm	-3.69 (0.47)
$H_2$17.03μm	-4.04 (0.46)
[SIII]18.71μm	-3.49 (0.48)
[SIII]33.48μm	-3.05 (0.31)

Table 4.1: Mean values of the log of line to IR (8-1000 μm) continuum luminosities for star-forming galaxies, $\langle\log(L_\ell/L_{\rm IR})\rangle$, and associated dispersions σ.

are excited by, or also by, AGNs. These include 3 typical AGN lines ([NeV]14.32 μm, [NeV]24.31 μm and [OIV]25.89 μm) and 8 lines that can also be produced in star formation regions (the 5 HII region lines: [SIV]10.49 μm, [NeII]12.81 μm, [NeIII]15.55 μm, [SIII]18.71 μm and [SIII]33.48 μm; three molecular hydrogen lines, H_2 9.66 μm, H_2 12.28 μm and H_2 17.03 μm). The other IR lines considered in chap. 3 have negligible AGN contributions so that I adopt directly the luminosity functions derived there. In addition I present results for the 6.2, 7.7 and 8.6μm Polycyclic Aromatic Hydrocarbons (PAH) lines. Of course, to detect the broad PAH lines the SAFARI ($R = 2000$) spectral resolution needs to be degraded without loss of signal, using appropriate algorithms. All the lines have been taken into account to compute the number of sources detected in more than one line.

The line luminosities are derived from the continuum ones exploiting the relations between line and IR (or bolometric in the AGN case) luminosities, taking into account the dispersions around the mean values. Again for the starburst component I have collected from the literature data on 3 additional lines (H_2 9.66 μm, [SIV]10.49 μm and H_2 12.28 μm), excluding objects for which there is evidence of a substantial AGN contribution. These data are shown in Fig. 4.4 together with the best fit linear relations. I have neglected the starburst contribution to the 3 typical AGN lines.

The mean ratios $\langle\log(L_\ell/L_{\rm IR})\rangle$ for star-forming galaxies and the dispersions around them are given in Table 4.1. The values for the 6.2, 7.7 and 8.6μm PAH lines (also given in Table 4.1) were inferred from that for the PAH 11.25 μm line, given in chap. 3, using the average ratios $L_{PAH_{6.2}}/L_{PAH_{11.25}} = 1.22$, $L_{PAH_{7.7}}/L_{PAH_{11.25}} = 4.5$ and $L_{PAH_{8.6}}/L_{PAH_{11.25}} = 1.36$ given by Fiolet et al. (2010).

The relationships between line and bolometric luminosities of AGNs were determined using the data on the QSO samples by Veilleux et al. (2009), on the local Seyfert galaxies whose mid-IR emission was found to be 100% AGN dominated by Sturm et al. (2002) and, only for the three pure AGN lines ([NeV]14.32 μm, [NeV]24.31 μm and [OIV]25.89 μm), on the local Seyfert galaxies by Tommasin et al. (2008, 2010) coupled with the continuum nuclear emission measurements by Gorjian et al. (2004), Gandhi et al. (2009) and Hönig et al. (2010).

The IR luminosities given in Veilleux et al. (2009) and Sturm et al. (2002) are defined as in Sanders & Mirabel (1996), but this definition applies to starburst not to AGN SEDs. Therefore to convert them to AGN bolometric luminosities I cannot use the correction factors given in par. 4.1. The AGN bolometric luminosities were then estimated using the appropriate Cai et al. (2013) SEDs (i.e. for QSOs and Seyfert 1 galaxies the mean QSO SED of Richards et al. 2006 extended to millimeter wavelengths as described in Cai et al. 2013; for Seyfert 2 galaxies the SED of the local AGN-dominated ULIRG Mrk 231 taken from the SWIRE library) normalized to the observed $12\,\mu$m luminosities which are expected to be modestly affected by contamination from the host galaxy. Normalizing instead to the AGN $6\,\mu$m fluxes of Sani et al. (2010), I obtain, for a sub-sample containing 65% of the objects, an average decrease of the estimated AGN bolometric luminosity by about 17%. On the other hand I caution that the Mrk 231 SED might have a non-negligible host galaxy contamination. In fact its far-IR emission peaks at $\sim 100\,\mu$m. At such relatively long wavelength the contribution from dust heated by young stellar populations can be substantial or even dominant (Mullaney et al. 2011). Therefore my approach likely overestimates the bolometric luminosities of Seyfert 2 galaxies. This however has little impact on my conclusions since these AGNs are minor contributors to line counts at the SPICA-SAFARI detection limits.

At variance with star-forming galaxies for which data and extensive simulations are consistent with a constant line-to-continuum IR luminosity ratio (see chap. 3), for AGNs observational data indicate luminosity dependent ratios (Hill et al., 2014). I adopt a relation of the form $\log(L_\ell) = a \cdot \log(L_{\rm bol}) + b$. The best fit coefficients for the 11 lines of my sample and the dispersions, σ, are listed in Table 4.2. There are no significant differences among

Spectral line	a	b	disp (1σ)
$H_2 9.66\mu m$	1.07	-5.32	0.34
[SIV]$10.49\mu m$	0.90	-2.96	0.24
$H_2 12.28\mu m$	0.94	-3.88	0.24
[NeII]$12.81\mu m$	0.98	-4.06	0.37
[NeV]$14.32\mu m$	0.78	-1.61	0.39
[NeIII]$15.55\mu m$	0.78	-1.44	0.31
$H_2 17.03\mu m$	1.05	-5.10	0.42
[SIII]$18.71\mu m$	0.96	-3.75	0.31
[NeV]$24.31\mu m$	0.69	-0.50	0.39
[OIV]$25.89\mu m$	0.70	-0.04	0.42
[SIII]$33.48\mu m$	0.62	0.35	0.30

Table 4.2: Coefficients of the best-fit linear relations between line and AGN bolometric luminosities, $\log(L_\ell) = a \cdot \log(L_{\rm bol}) + b$, and 1σ dispersions associated to the relations.

the line–bolometric luminosity correlations for the different AGN types (see Fig. 4.5).

4.3 Line luminosity functions and number counts

To compute the line luminosity functions and the number counts I adopted a Monte Carlo approach, starting from the redshift-dependent luminosity functions of the source populations described in par. 4.1, including both the starburst and the AGN component. Each source was assigned luminosities of each component drawn at random from the appropriate probability distributions (see par. 4.1). Then I associated to each component line luminosities drawn at random from Gaussian distributions with the mean values and the dispersions given in Tables 4.1 and 4.2. This procedure gives the line luminosity functions of the objects as a whole, as well as of their starburst and AGN components. Examples are shown in Figs. 4.6 and 4.7.

The counts are then straightforwardly computed. The wavelength range covered by each SPICA-SAFARI band, $[\lambda_{\rm min}, \lambda_{\rm max}]$, and the line rest-frame wavelength, λ_ℓ, define the minimum and the maximum redshift within which the line is detectable in that band, $z_{\ell,{\rm min/max}} = \lambda_{\rm min/max}/\lambda_\ell - 1$. The integral counts predicted by my model in the SPICA-

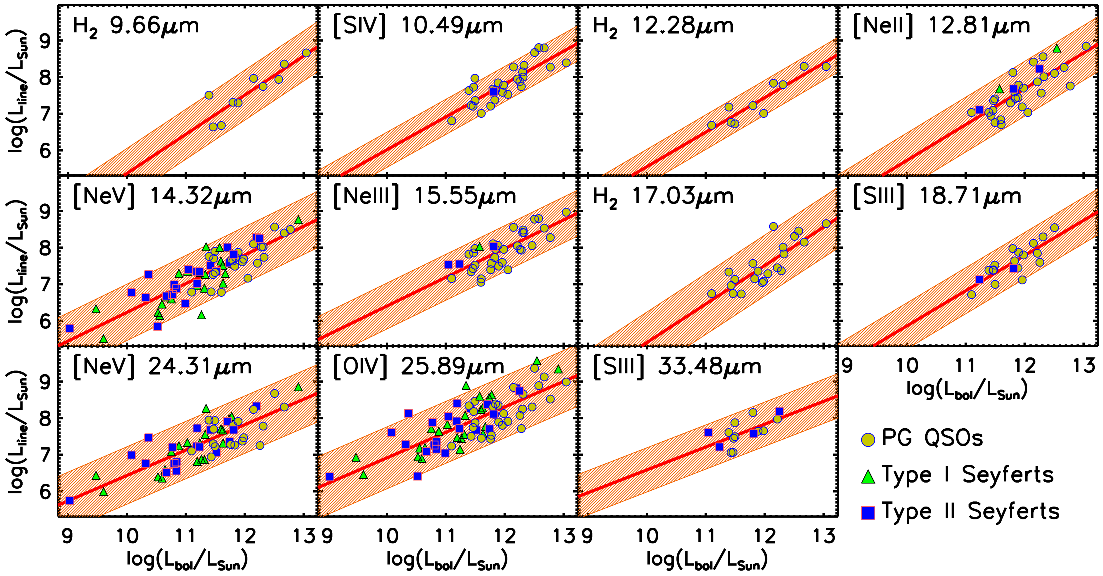

Figure 4.5: Line versus bolometric luminosity, in solar units, for AGNs. PG QSO data (yellow circles) are taken from Veilleux et al. (2009), Seyfert 1 (green triangles) and Seyfert 2 (blue squares) data from Sturm et al. (2002) and, only for the [NeV]14.32 μm, [NeV]-24.31 μm and [OIV]25.89 μm lines, also from Tommasin et al. (2008, 2010). The orange bands show the $2\,\sigma$ spread around the linear relations $\log(L_\ell) = a \cdot \log(L_{\rm bol}) + b$ (red line).

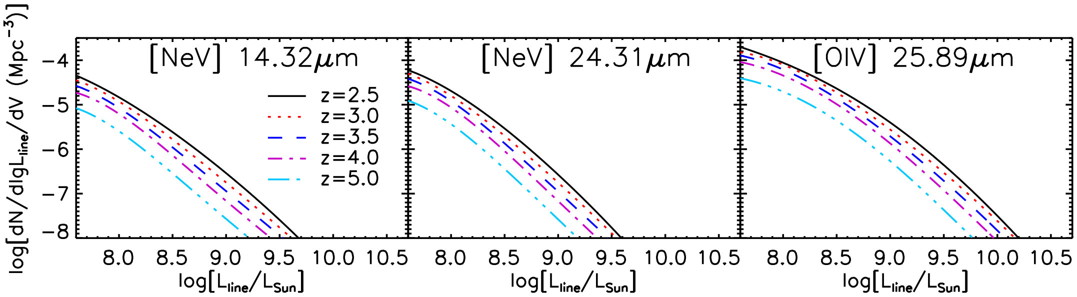

Figure 4.6: Predicted luminosity functions of the three typical AGN lines of my sample at different redshifts at which these lines can be detected by SPICA-SAFARI.

SAFARI wavelength range for the 14 IR lines of my sample are shown in Fig. 4.8.

I present predictions for a survey of 5 deg^2 with 1 hr per FoV. The survey area is 10 times larger compared to the reference survey considered in chap. 3. In fact, as discussed later on in this chapter, AGN lines are more difficult to detect than starburst lines and thus a wider/deeper survey is required to achieve a good statistics. The predicted numbers of sources detected in each line by a SPICA-SAFARI survey covering 5 deg^2 with a 1 hr integration/FoV are given in the last column of Table 4.3. The other columns detail the redshift distributions of detected sources. This SPICA-SAFARI survey will be able to detect many hundreds of AGNs (762, according to my calculations) in the strongest line ([OIV]25.89μm).

The redshift distributions of sources detected in the three AGN lines [NeV]14.32μm, [NeV]24.31μm and [OIV]25.89μm are displayed in Fig. 4.9, where the redshift ranges covered by the different bands are identified by different colours. Fig. 4.10 shows the contributions to the counts of AGNs of the various kinds.

Fig. 4.11 illustrates the luminosity and redshift distributions of sources (starburst plus AGN components) for which the SPICA-SAFARI 5 deg^2 survey will detect at least 2, 3 or 4 lines, taking into account both the spectral lines considered in this chapter and the pure starburst lines considered in chap. 3. I expect that 114903, 50817, 29492, 18412, 11555 and

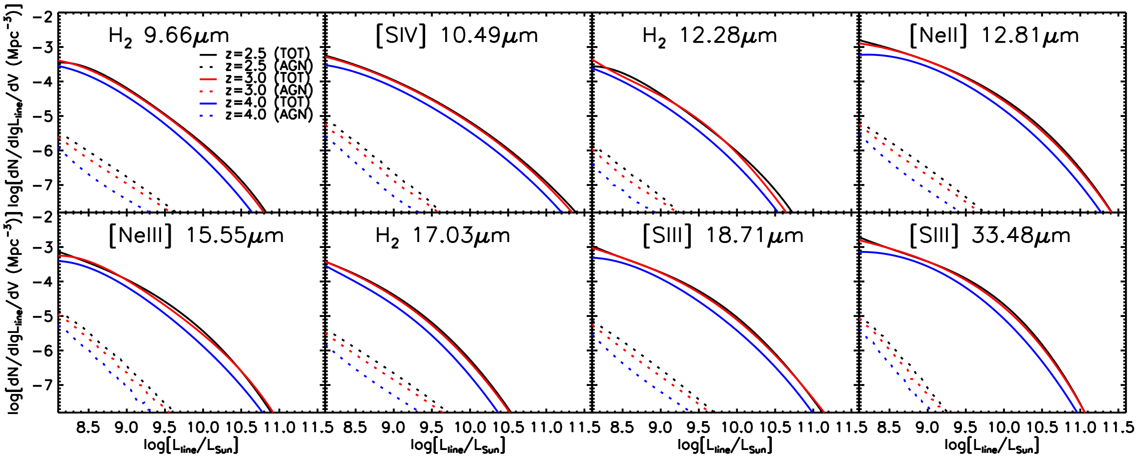

Figure 4.7: Predicted luminosity functions for the total (starburst plus AGN) emission (solid lines) and for the AGN component only (dashed lines) at different redshifts at which these lines can be detected by SPICA-SAFARI.

6930 sources will be detected in at least 1, 2, 3, 4, 5 and 6 lines, respectively. The numbers of proto-spheroidal galaxies detectable in at least 1, 2, 3, 4, 5 and 6 lines are 44335, 13854, 6149, 3151, 1749 and 907, respectively. Sources detected in at least one line include ~ 724 strongly lensed galaxies at $z > 1$; about 300 of them will be detected in at least 2 lines.

It is easily seen that these values, once rescaled to the same survey area, a factor of 10 smaller, are similar to those calculated in chap. 3 considering only star-forming galaxies: the AGN component adds a minor contribution. The reason for that is illustrated by Fig. 4.12 where the luminosity functions of the brightest AGN line ([OIV]25.89μm) are compared with those of two bright starburst lines at 2 redshifts. Two factors concur to yield a much higher space density of detectable starbursts compared to AGNs. First, AGNs are far less numerous than starburst galaxies, due to the much shorter lifetime of their bright phase. Second, many starburst lines have ratios to bolometric luminosity substantially higher than even the brightest AGN line (cf. the luminosity ratios for starbursts in Tab. 3.1 with those for AGNs in Tab. 4.2).

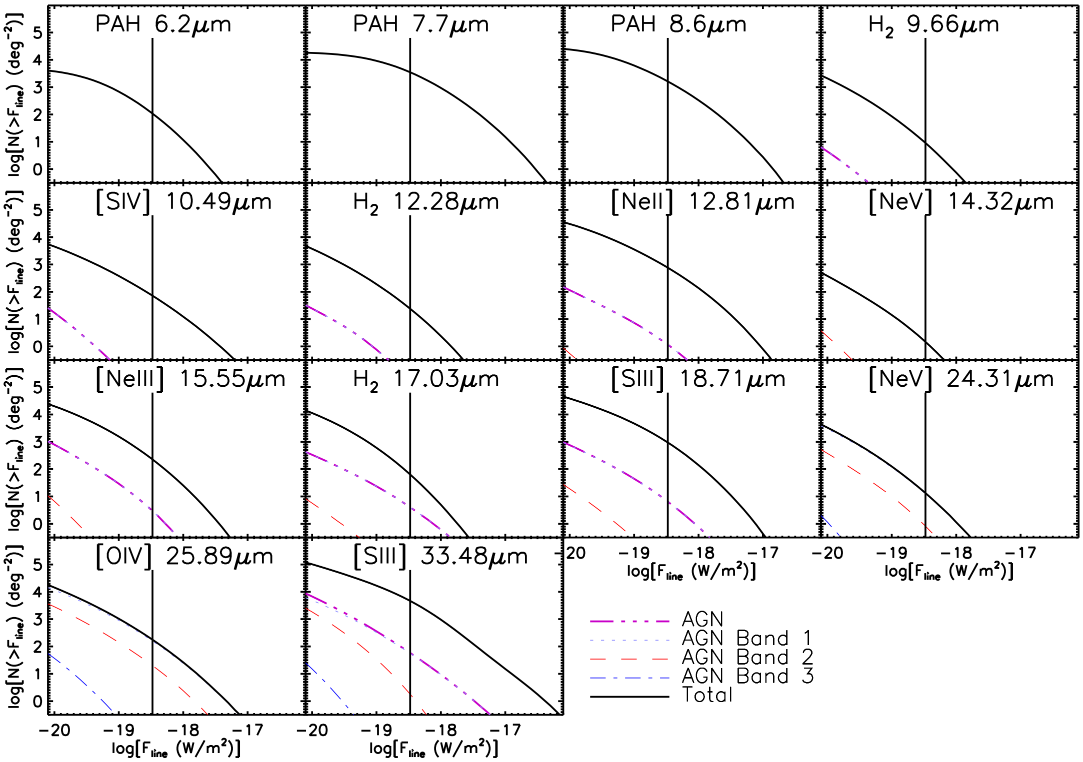

Figure 4.8: Integral counts in several lines of galaxies as a whole (starburst plus AGN components; solid black lines) and of AGNs only (dash-dotted violet lines) over the full SPICA-SAFARI wavelength range, and, for the AGNs, in each of its three bands. The vertical lines correspond to the average detection limit in the 3 bands for 1 hr integration/FoV.

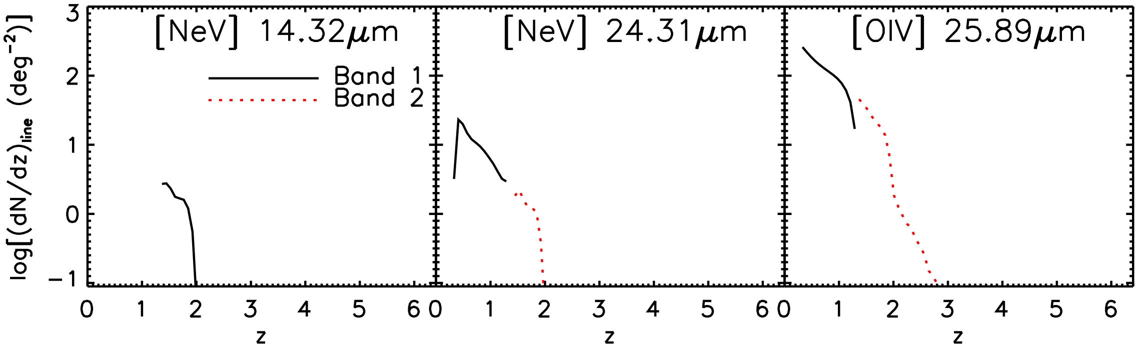

Figure 4.9: Examples of the predicted redshift distributions of AGNs detected by SPICA-SAFARI for a 1 hr exposure per FoV. The different colours identify the spectral bands.

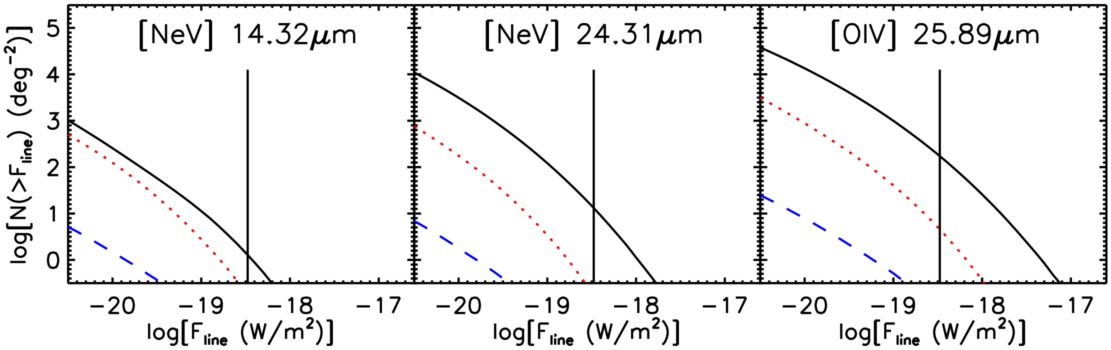

Figure 4.10: Contributions of different AGN populations to the integral counts in the [NeV]14.32μm, [NeV]24.31μm and [OIV]25.89μm lines. Solid black line: AGNs associated to late-type galaxies plus optically selected AGNs; dotted red line: AGN associated to unlensed proto-spheroids; dashed blue line: AGNs associated to strongly gravitationally lensed proto-spheroids. The vertical lines correspond to the average value of the detection limits ($3.7 \cdot 10^{-19}$ W/m^2, $3.4 \cdot 10^{-19}$ W/m^2, $2.9 \cdot 10^{-19}$ W/m^2) for the three bands ($34-60\,\mu$m, $60-110\,\mu$m, $110-210\,\mu$m) for 1-hr exposure per FoV.

4.4 Comparison with Previous Estimates

Fig. 4.13 compares my predictions for the redshift distributions of sources detected by SPICA-SAFARI with those from the 3 models used by Spinoglio et al. (2012). The total number of detections, for each line, is also summarized in Table 4.4.

The different results reflect the different approaches adopted by the authors (only very marginally the different evolutionary models used). In particular, Spinoglio et al. (2012)[1] based their estimate on empirical relations between the line luminosities and the total IR luminosity for the Seyfert galaxies of the $12\,\mu$m galaxy sample (Tommasin et al., 2008, 2010), and for the pure starburst galaxies of the sample of Bernard-Salas et al. (2009). These luminosity ratios were then used to convert the total IR luminosity functions from different evolutionary models (i.e. Valiante et al. 2009; Franceschini et al. 2010; Gruppioni

---

[1] In the calculation of the IR luminosities used to calibrate the line to continuum relations in the Spinoglio et al. (2012) paper a factor of 1.8 was inadvertently omitted, resulting in an overestimate of the line counts (see Erratum Spinoglio et al. 2014).

et al. 2011) into line luminosity functions and to derive the numbers of objects detectable by SPICA at different redshifts and luminosities. This approach - purely empirical - could be taken as an upper limit for the SPICA detections, since it applies the relations found for a sample of AGNs to all the AGN populations considered in the models, regardless of the AGN contribution to $L_{\rm IR}$, while - thanks to *Herschel* - I now know that $L_{\rm IR}$ in IR detected AGNs is typically composed by both AGN and starburst contributions (Hatziminaoglou et al., 2010) in different proportions (in large fractions of objects the AGN contributes to $L_{\rm IR}$ for <10%; see Delvecchio et al. 2014).

On the other hand the approach adopted here requires bolometric corrections, endowed with a substantial uncertanty, to derive the relationships between line and bolometric luminosities. I are now working on a semi-empirical approach, based on SED decomposition (see Berta et al. 2013; Delvecchio et al. 2014) of local (Tommasin et al., 2008, 2010) and high-z samples of AGN (from *Herschel* PACS Evolutionary Probe: Lutz et al. 2011), considering nuclear observational data in the MIR for estimating the $L_{\rm line}/L_{\rm bol}$ relations and the AGN accretion luminosity function of Delvecchio et al. (2014) to derive expected detection numbers. The results of that work will be published in a forthcoming paper (Gruppioni, Berta, Spinoglio et al. in preparation).

4.5 Observation strategy

Quantitative predictions on the number of detections of AGNs and of galaxies as a whole for a survey of $0.5\,{\rm deg}^2$ and different integration times per FoV are given in Table 4.5. As illustrated by Fig. 4.8, the integral counts have a slope flatter than 2 at and below the detection limit for 1 hr integration/FoV. This means that the number of detections at fixed observing time increases more extending the survey area than going deeper. This is particularly true for the 3 typical AGN lines (cf. Fig. 4.10), due to the fact that the AGN

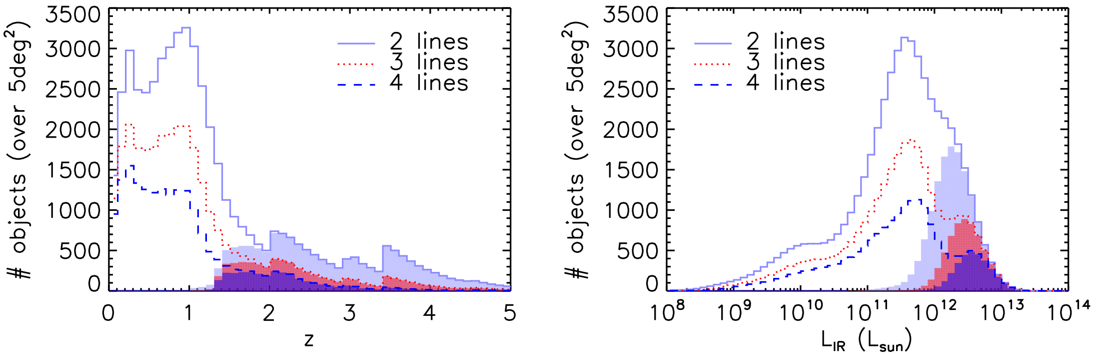

Figure 4.11: Predicted redshift (left) and total IR luminosity (right) distributions of galaxies (starburst plus AGN components) detectable in two (cyan histogram), three (red) and four (blue) spectral lines, by a SPICA-SAFARI survey covering 5 deg^2 in 1 hr integration/FoV (taking into account both the spectral lines of this sample and those presented in chap. 3). The shaded areas represent the contributions of proto-spheroids.

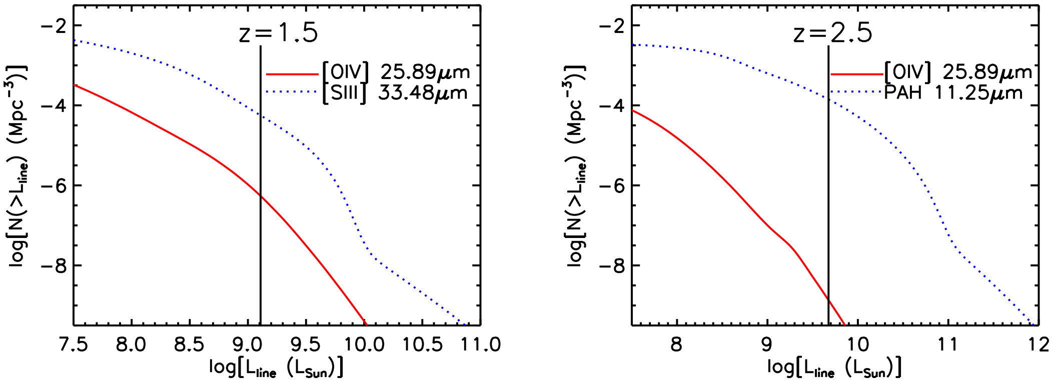

Figure 4.12: Comparison of the cumulative luminosity functions at 2 redshifts of the brightest AGN line ([OIV]25.89μm) with those of two bright starburst lines. The dotted curves show the contributions of strongly lensed sources to the total luminosity functions (solid curves). At each redshift the vertical line corresponds to the minimum luminosity detectable by a survey with 1 hr integration/FoV.

Spectral line	0.00 − 0.75	0.75 − 1.25	1.25 − 1.75	1.75 − 2.25	2.25 − 2.75	2.75 − 4.00	4.00 − 6.00	6.00 − 8.00	All z
PAH6.2μm	0 (0)	0 (0)	0 (0)	0 (0)	0 (0)	0 (0)	0 (432)	0 (19)	0 (451)
PAH7.7μm	0 (0)	0 (0)	0 (0)	0 (0)	0 (0)	0 (8750)	0 (6787)	0 (237)	0 (15775)
PAH8.6μm	0 (0)	0 (0)	0 (0)	0 (0)	0 (0)	0 (5778)	0 (1280)	0 (26)	0 (7085)
$H_2$9.66μm	0 (0)	0 (0)	0 (0)	0 (0)	0.2 (18)	0.2 (21)	0 (0.7)	0 (0)	0.4 (39)
[SIV]10.49μm	0 (0)	0 (0)	0 (0)	0 (9)	0.1 (169)	0 (119)	0 (12)	0 (0.2)	0.1 (308)
$H_2$12.28μm	0 (0)	0 (0)	0 (0)	0.3 (58)	0 (26)	0 (11)	0 (1)	0 (0)	0.3 (95)
[NeII]12.81μm	0 (0)	0 (0)	1 (490)	1 (1515)	0.4 (748)	0.3 (495)	0 (43)	0 (0.3)	3 (3293)
[NeV]14.32μm	0 (0)	0 (0)	9 (9)	2 (2)	0.4 (0.4)	0.2 (0.2)	0 (0)	0 (0)	11 (11)
[NeIII]15.55μm	0 (0)	1 (82)	10 (493)	2 (220)	0.3 (92)	0.3 (52)	0 (1)	0 (0)	13 (941)
$H_2$17.03μm	0 (0)	9 (84)	10 (100)	1 (45)	0.4 (20)	0.2 (10)	0 (0.3)	0 (0)	20 (260)
[SIII]18.71μm	0 (0)	13 (2040)	10 (1125)	1 (499)	0.4 (261)	0.1 (143)	0 (10)	0 (0.3)	25 (4078)
[NeV]24.31μm	28 (28)	19 (19)	8 (8)	1 (1)	0.3 (0.3)	0.2 (0.2)	0 (0)	0 (0)	55 (55)
[OIV]25.89μm	426 (426)	227 (227)	89 (89)	20 (20)	1 (1)	0.3 (0.3)	0 (0)	0 (0)	762 (762)
[SIII]33.48μm	235 (9876)	10 (6760)	1 (2947)	1 (1289)	0.2 (771)	0.1 (438)	0 (21)	0 (0)	248 (22104)

Table 4.3: Predicted redshift distributions of AGNs and, in parenthesis, of galaxies as a whole (starburst plus AGN components) detectable by a SPICA-SAFARI survey covering an area of 5 deg^2 in 1 h integration per FoV.

Spectral line	**This work**	Spinoglio et al. (2012)		
	Cai et al. (2013)	Franceschini et al. (2010)	Gruppioni et al. (2011)	Valiante et al. (2009)
[NeII]12.81μm	**0.3**	15	14	42
[NeV]14.32μm	**1**	0.4	1	–
[NeIII]15.55μm	**1**	41	25	179
$H_2$17.03μm	**2**	0	0.4	6
[SIII]18.71μm	**3**	3	2	6
[NeV]24.31μm	**5**	53	143	–
[OIV]25.89μm	**76**	326	623	938
[SIII]33.48μm	**25**	244	400	1103

Table 4.4: Numbers of $5\,\sigma$ AGN detections by SPICA-SAFARI for a survey covering 0.5 deg^2 in 1 hr integration/FoV, as predicted by the present model (second column, in boldface) compared with those given (only for 8 lines) by Spinoglio et al. (2012) for the 3 models used by them.

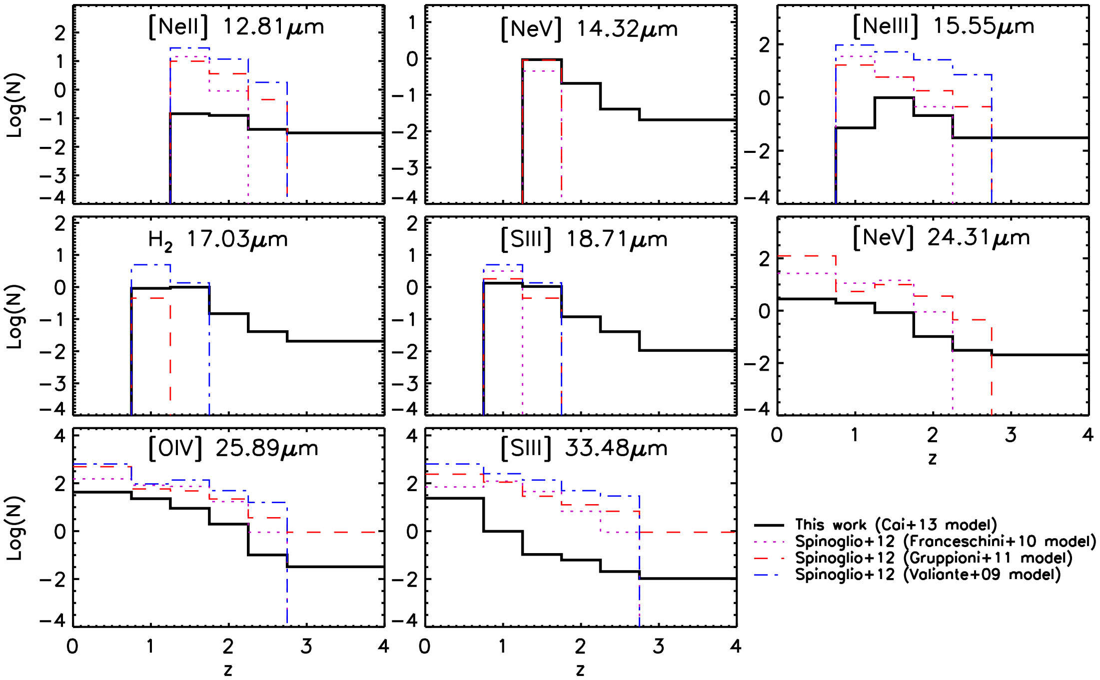

Figure 4.13: Redshift distributions of AGNs detectable in each of the 8 lines by a SPICA-SAFARI survey covering 0.5 deg^2 with 1 hr integration/FoV. The predictions of my reference model (black solid lines) are compared with those of the 3 models used by Spinoglio et al. (2012); see the legend on the bottom right.

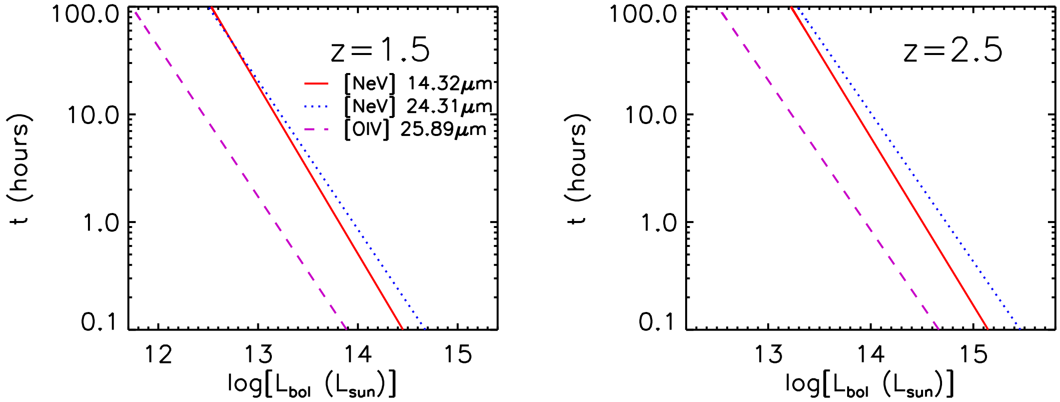

Figure 4.14: SPICA-SAFARI exposure time per FoV required for a 5σ line detection of the three typical AGN lines as a function of the AGN bolometric luminosity for $z = 1.5$ (left) and $z = 2.5$ (right).

contribution to the bolometric luminosity is higher at higher luminosities. For a survey of $0.5\,\mathrm{deg}^2$ and 1 h integration/FoV the detection rate of AGNs is quite low and the predicted redshift distributions sink down at $z \gtrsim 1$ (cf. Fig. 4.9). To investigate with sufficient statistics the galaxy–AGN co-evolution a deeper or a wider area survey is necessary. For example, a survey of 1 hr/FoV over $5\,\mathrm{deg}^2$ would yield about 760 AGN detections in the [OIV]25.89μm line, with a total observing time of 4500 hours. A deeper survey with the same observing time (exposure time of 10 hr/FoV over $0.5\,\mathrm{deg}^2$) would give 427 AGN detections (see Table 4.5).

The blind spectroscopic survey may be complemented by follow-up observations of bright high-z galaxies already discovered at (sub-)mm wavelengths over much larger areas. Fig. 4.14 shows, as an example, the SPICA-SAFARI exposure time per FoV necessary for a 5σ detection of the three typical AGN lines at $z = 1.5$ and $z = 2.5$ as a function of the AGN bolometric luminosity. When SPT and *Herschel* survey data will be fully available we will have samples of many hundreds of galaxies with either intrinsic or apparent (i.e. boosted by strong gravitational lensing; Negrello et al., 2010, 2014; Vieira et al., 2013) IR luminosities larger than $10^{13}\,L_\odot$. These IR luminosities correspond to SFR $> 10^3\,M_\odot\,\mathrm{yr}^{-1}$ (Kennicutt & Evans, 2012). Comparing the stellar with the halo mass function Lapi et al. (2011) estimated that the active star formation phase lasts for $\sim 0.7\,\mathrm{Gyr}$. Thus objects that bright are the likely progenitors of spheroidal galaxies with stellar masses $M_\star \gtrsim 7\times10^{11}/\mu\,M_\odot$, μ being the gravitational magnification factor. As shown by Fig. 4.14, SPICA-SAFARI can detect, in 10 h, the [OIV]25.89μm line from an AGN with (real or apparent) bolometric luminosity of $\simeq 3\times10^{12}\,L_\odot$ at $z = 1.5$ and of $\simeq 2\times10^{13}\,L_\odot$ at $z = 2.5$. For Eddington limited accretion these luminosities correspond to black hole masses of $\simeq 9\times10^7/\mu\,M_\odot$ and $\simeq 6\times10^8/\mu\,M_\odot$. For comparison, from the black hole/stellar mass correlation (Kormendy & Ho 2013) I get that the final black hole masses associated to spheroidal galaxies with stellar masses of $\simeq 10^{11}\,M_\odot$ and $\simeq 10^{12}\,M_\odot$ are $\simeq 5\times10^8\,M_\odot$ and $\simeq 7\times10^9\,M_\odot$, respectively.

Spectral line	$t = 1h$ $0.5\,\mathrm{deg}^2$	$t = 10\,\mathrm{h}$ $0.5\,\mathrm{deg}^2$
PAH6.2μm	0 (45)	0 (280)
PAH7.7μm	0 (1578)	0 (4183)
PAH8.6μm	0 (709)	0 (2661)
$H_2$9.66μm	4×10^{-2} (4)	0.1 (33)
[SIV]10.49μm	1×10^{-2} (31)	3×10^{-2} (156)
$H_2$12.28μm	3×10^{-2} (10)	0.1 (74)
[NeII]12.81μm	0.3 (330)	3 (1490)
[NeV]14.32μm	1 (1)	5 (5)
[NeIII]15.55μm	1 (94)	11 (627)
$H_2$17.03μm	2 (26)	9 (236)
[SIII]18.71μm	3 (409)	18 (1979)
[NeV]24.31μm	5 (5)	48 (48)
[OIV]25.89μm	76 (76)	427 (427)
[SIII]33.48μm	25 (2211)	147 (7826)

Table 4.5: AGN and total (in parenthesis) detections obtainable by SPICA-SAFARI surveys covering $0.5\,\mathrm{deg}^2$ in 1 h integration/FoV (2^{nd} column) and 10 h integration/FoV (3^{th} column).

This means that pointed SPICA-SAFARI observations can allow us to investigate early phases of the galaxy/AGN co-evolution, when the black hole mass was one or even two orders of magnitude lower than the final one.

Chapter 5

Predictions for surveys with the SPICA Mid-infrared Instrument

SPICA will be equipped with two main instruments: SAFARI (presented in chapters 3 and 4) and the SPICA Mid-infrared Instrument (SMI)[1]. In chapters 3 and 4, I have presented detailed predictions for the number counts and the redshift distributions of galaxies detectable in blind spectroscopic surveys with SAFARI, accounting for both the starburst and the Active Galactic Nucleus (AGN) components. Here I focus on the SMI.

The SMI has two basic observing modes: the wide-field imaging camera mode and the spectrometer mode with two detectors (Spec-S and Spec-L; Kataza et al., 2012). Updated technical specifications for the SMI are: R=1000 spectrometers, FoV = $150'' \times 3''$, wavelength ranges $20 - 27\,\mu$m (Spec-S) and $27 - 37\,\mu$m (Spec-L); R=20 wide field camera, FoV $= 5' \times 5'$, wavelength range $20 - 37\,\mu$m. The spatial resolution (FWHM) varies from $1.4''$ at $20\,\mu$m to $2.6''$ at $37\,\mu$m. The line detection limit (1 hr, $5\,\sigma$) is in the range $9 - 15 \times 10^{-20}\,\mathrm{W\,m^{-2}}$ for the camera, $2 - 7 \times 10^{-20}\,\mathrm{W\,m^{-2}}$ for the Spec-S and $3 - 10 \times 10^{-20}\,\mathrm{W\,m^{-2}}$ for the Spec-L. The point source continuum sensitivity (1 hr, $5\,\sigma$)

---

[1] https://home.sron.nl/files/LEA/SAFARI/spica_workshop_2014 /SMI_factsheet2.pdf
https://home.sron.nl/files/LEA/SAFARI/spica_workshop_2014 /KanedaH_SPICA_workshop_2014.pdf

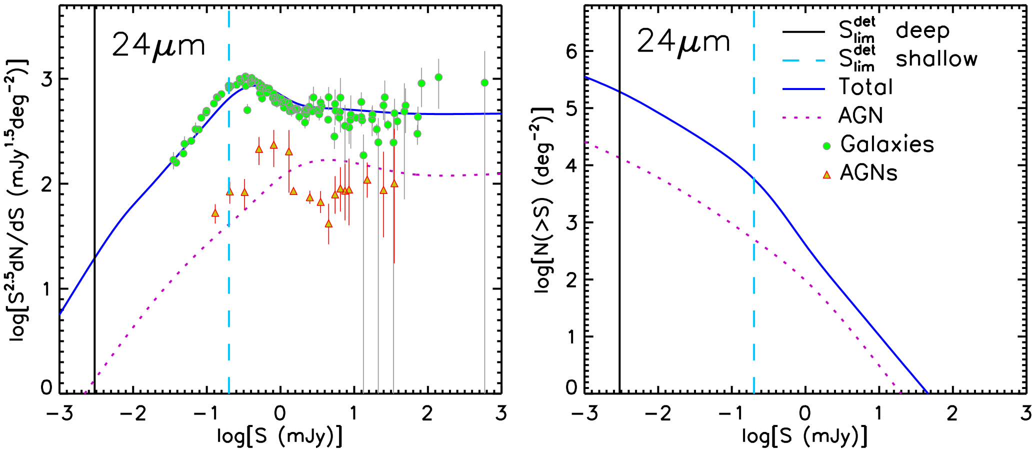

Figure 5.1: Euclidean normalized differential number counts (on the left) and integral counts (on the right) at 24 μm given by the adopted model for galaxies as a whole (starburst plus AGN components; solid blue lines) and for AGNs alone (dotted violet lines). The vertical solid black and dashed cyan lines correspond to the SMI camera detection limits for the proposed deep and shallow surveys, respectively. Counts of galaxies (filled green circles) are from Takagi et al. (2012), Clements et al. (2011), Béthermin et al. (2010), Le Floc'h et al. (2009), Shupe et al. (2008) and Papovich et al. (2004); AGN counts (filled yellow triangles) are from Treister et al. (2006) and Brown et al. (2006).

in a low background region increases from $9\,\mu$Jy at $20\,\mu$m to $50\,\mu$Jy at $37\,\mu$m; at $24\,\mu$m it is $\simeq 10.4\,\mu$Jy. The survey speed for the $5\,\sigma$ detection of a point source with a continuum flux density of $40\,\mu$Jy with the camera is $\sim 7\,\mathrm{arcmin}^2/\mathrm{hr}$; for the detection of the line flux of $2 \times 10^{-19}\,\mathrm{W\,m}^{-2}$ it is $\sim 4\,\mathrm{arcmin}^2/\mathrm{h}$ for Spec-S and $\sim 2\,\mathrm{arcmin}^2/\mathrm{h}$ for Spec-L.

The SMI instrument is crucial to enhance the outcomes of the spectroscopic surveys carried out with SAFARI. The $R = 1000$ spectrometer is needed to observe fine-structure lines with a resolution similar to SAFARI, whereas the $R = 20$ wide field camera is essential to uncover star-forming galaxies in the four broad and very bright PAH bands at 6.2, 7.7, 8.6 and 11.3μm. The SMI will also substantially improve our knowledge of source counts in the MIR region by extending the counts to much fainter flux density levels than achieved by *Spitzer* and reaching a much better statistics. The lines that will be detected can come either from star-forming regions or from nuclear activity or from both. The SMI spectroscopy will permit to exploit the rich suite of MIR diagnostic lines to trace the star formation and the accretion onto the super-massive black holes up to high redshifts through both blind spectroscopic surveys and pointed observations.

In this chapter, I use again the Cai et al. (2013) evolutionary model upgraded as discussed in chap. 4. The model deals in a self consistent way with the emission of galaxies as a whole, including both the starburst and the AGN component, and was successfully tested against a large amount of observational data.

Both type 1 and type 2 AGNs, with relative abundances, as a function of luminosity, derived by Hasinger (2008) (see Fig. 5.4 from Bianchi et al. 2012) are taken into account.

The plan of this chapter is the following. In par. 5.1 I discuss imaging observations with the wide field SMI camera. In par. 5.2 I present the relations between line and continuum luminosity for the main MIR lines. In par. 5.3 I work out our predictions for line luminosity functions, number counts and redshift distributions within the SMI wavelength coverage. In par. 5.4 I discuss possible SMI observational strategies.

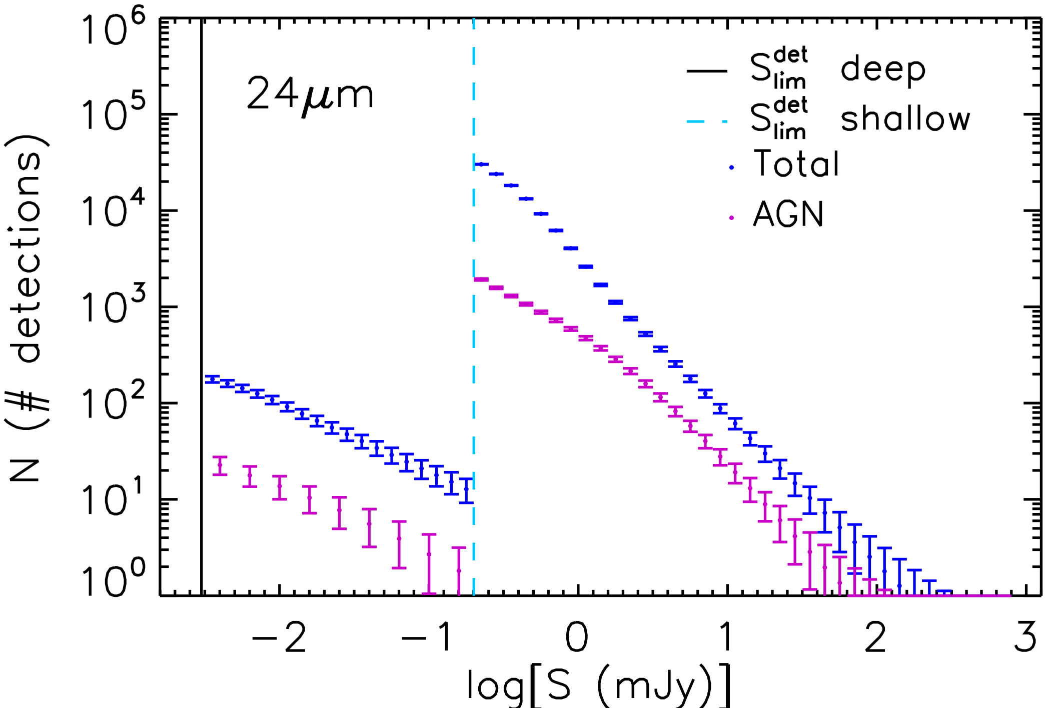

Figure 5.2: Number of predicted detections (with Poissonian error bands) of galaxies and AGNs within $\Delta \log S = 0.1$ bins ($\Delta \log S = 0.2$ bins for faint AGNs) for the proposed shallow and deep survey with the SMI camera. The vertical solid black and dashed cyan lines correspond to the survey $5\,\sigma$ detection limits.

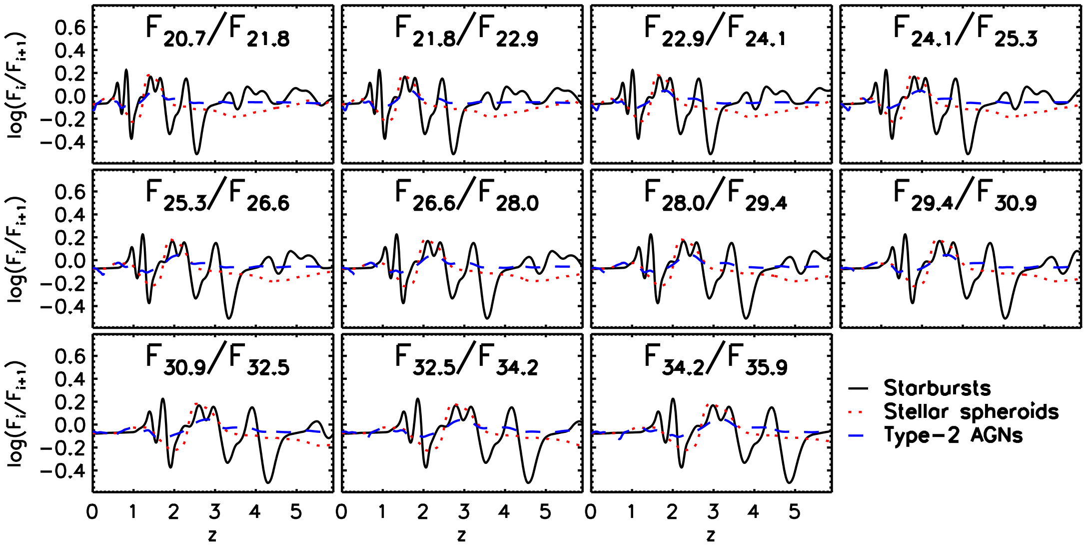

Figure 5.3: Ratios of flux densities at the central wavelengths of adjacent SMI camera filters for the three SEDs used for the model calculations: starburst galaxy (solid black lines), proto-spheroidal galaxy (dotted red lines) and type 2 AGN (dashed blue lines).

5.1 Surveys with the wide field camera

The camera can substantially extend the flux density range over which the mid-IR number counts have been measured by the *Spitzer* satellite. Using the counts yielded by the model, that are strongly constrained by observational data (see the left panel of Fig. 5.1), I find a $5\,\sigma$ confusion limit at $24\,\mu$m of 4.8×10^{-5} mJy. For comparison, the deepest *Spitzer* surveys went down to 3.5×10^{-2} mJy (Béthermin et al., 2010), but below 8.0×10^{-2} mJy the results are endowed with substantial uncertainties due either to poor statistics or to substantial corrections for incompleteness.

With the current technical specifications, reaching a $5\,\sigma$ limit of 3.0×10^{-3} mJy will require $\simeq 635$ h per FoV. Observations of a single FoV will be enough to detect hundreds of sources per 0.1 dex in flux density. A survey at this limit would resolve $\simeq 92\%$ of the background estimated using the adopted model. A determination of the source counts

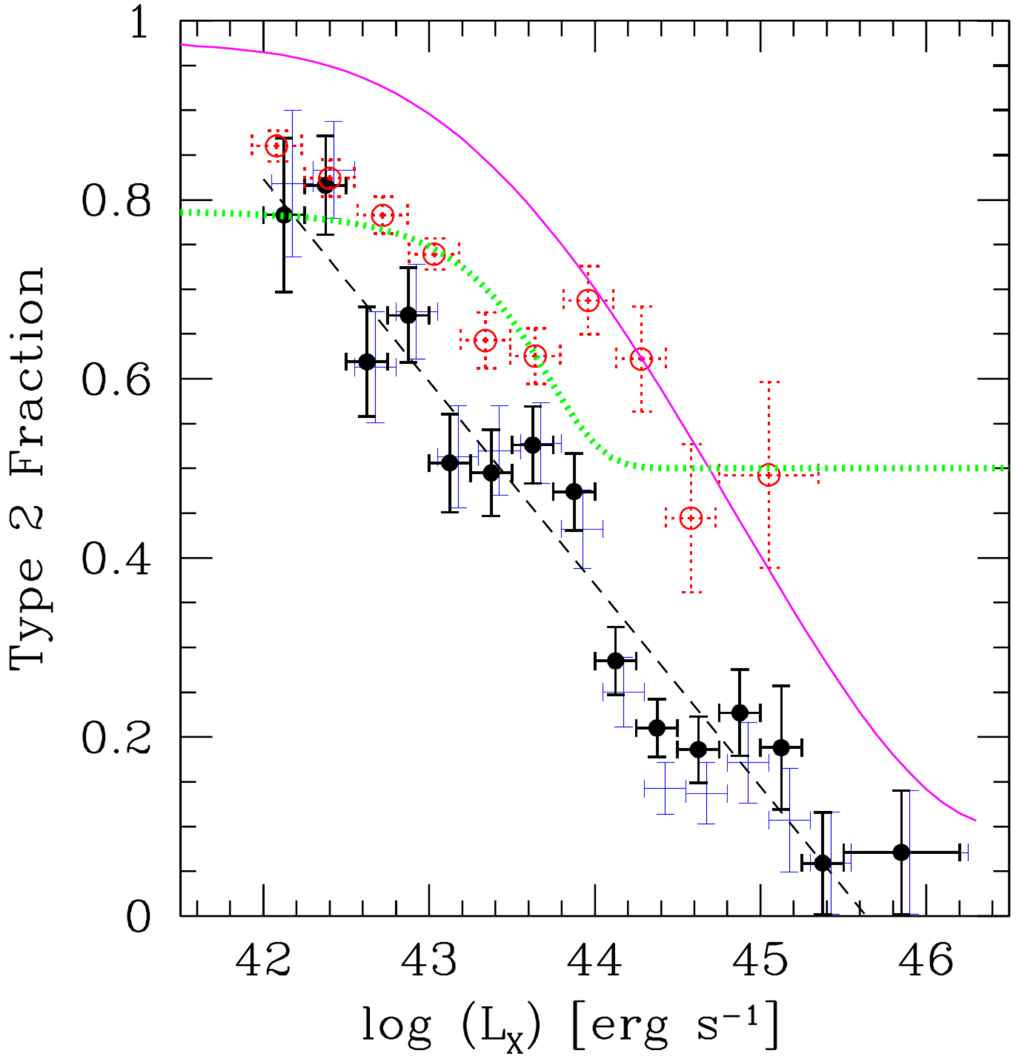

Figure 5.4: Fraction of type-2 AGN as a function of X-ray luminosity (from Hasinger 2008). The solid symbols show hard X-ray selected AGN (blue and black symbols illustrate different sub-samples in terms of redshift completeness). The red dotted symbols show optically selected AGN (from Simpson 2005). The magenta line shows the type-2 fraction inferred from the dust covering factor obtained through near/mid-IR observations (from Maiolino et al. 2007). The green dotted line shows the expected fraction of Compton-thin type-2 AGN according to the X-ray background synthesis models given in Gilli et al. (2007). (From Bianchi et al. 2012).

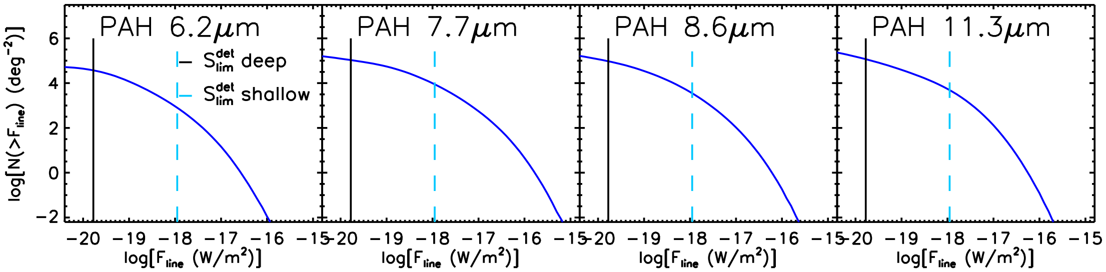

Figure 5.5: Integral counts in 4 PAH lines of star-forming galaxies over the SMI wide field camera wavelength range. The solid black and the dashed cyan vertical lines correspond to the SMI camera detection limits for the proposed deep and shallow surveys, respectively.

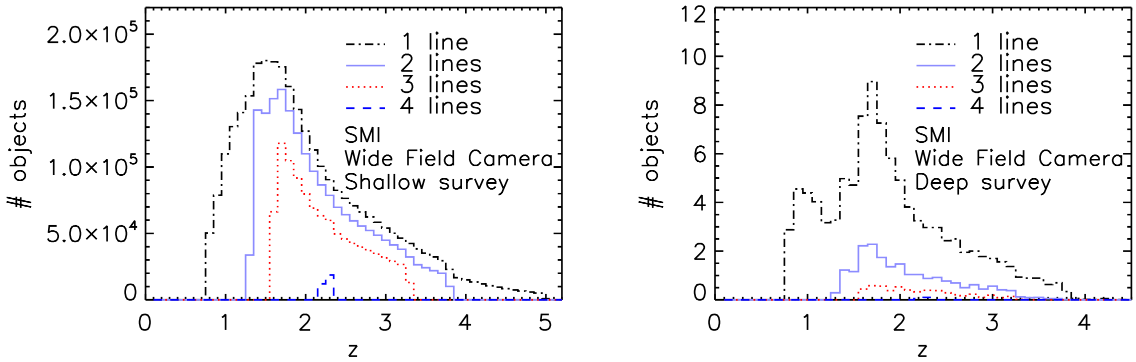

Figure 5.6: Redshift distributions of galaxies detected by the proposed shallow (left panel) and deep survey with the SMI wide-field camera.

over a very broad flux density interval can be achieved adding a shallow survey with a detection limit of 0.2 mJy, an integration time of $\sim 1.4 \times 10^{-1}$ h per FoV, covering an area of 20.0 deg^2. The global observing time (without overheads) is then 1046 h.

The right-hand panel of Fig. 5.1 shows the predicted integral counts at 24 μm of galaxies as a whole (starburst plus AGN component; solid blue lines) and of the AGNs alone (dotted violet lines). The proposed surveys are expected to detect $\simeq 1.1 \times 10^5$ galaxies and $\simeq 1.0 \times 10^4$ AGNs (shallow survey), and $\simeq 1.3 \times 10^3$ galaxies and $\simeq 94$ AGNs (deep survey).

Figure 5.2 shows the number of predicted detections (with Poissonian error bands) of galaxies and AGNs in $\Delta \log S = 0.1$ bins ($\Delta \log S = 0.2$ for AGNs in the case of the deep survey). Below 0.2 mJy, where observational data are largely absent (see Fig. 5.1), the proposed survey will detect from ~ 13 to ~ 177 galaxies per $\Delta \log S = 0.1$ bin, and from ~ 2 to ~ 23 AGNs per $\Delta \log S = 0.2$ bin. At 10 mJy, where the *Spitzer* counts have a very poor statistics, the proposed survey will detect ~ 76 galaxies and ~ 24 AGNs per $\Delta \log S = 0.1$ bin (Fig. 5.1).

A big plus of the SMI camera is its full coverage of the 20-37 μm spectral range with $R = 20$ resolution. Using the PAH emission template described in Groves et al. (2008) [their eq. (7)] and the normalized parameters of the Lorentzian components of the PAH emission band given in their Table 2, I have verified that the four PAH bands I consider fill the spectral resolution element of the camera for the whole redshift range of interest, so that their signal is not diluted. In the worst case the fraction of the PAH line flux falling within a resolution element varies from ~ 0.8 (PAH 7.7 and 8.6 μm) to ~ 1 (PAH 6.2 and 11.3 μm).

Coupling the relationships between the PAH and the IR luminosities discussed in par. 5.2 with the redshift dependent IR luminosity functions given by the model, I have computed the integral counts of galaxies in the four PAH lines over the wavelength range covered by the SMI wide field camera (see Fig. 5.5). I find that the proposed shallow survey will detect $\simeq 3.0 \times 10^6$ galaxies in at least one PAH line and $\simeq 1.9 \times 10^6$ in at least two lines; for the deep survey the number of detections are $\simeq 100$ in at least one line and $\simeq 20$ in at least two lines. The redshift distributions of galaxies detected in 1, 2, 3 and 4 lines are shown in Fig. 5.6.

In Fig. 5.3 I have split the spectral range of the camera into 12 bands, with $\Delta\lambda = \lambda/R$, centered at ∼20.7, 21.8, 22.9, 24.1, 25.3, 26.6, 28.0, 29.4, 30.9, 32.5, 34.2 and 35.9 μm, respectively. The curves show the flux ratios between adjacent bands as a function of redshift for two Spectral Energy Distributions (SEDs) of star-forming galaxies (the starburst and the proto-spheroidal galaxy SED used by Cai et al., 2013) and for the SED of the local AGN-dominated source Mrk 231, taken from the SWIRE library (Polletta et al., 2007). The figure shows that the resolution of the camera allows a good sampling of the starburst spectral features, and notably of the PAH bands. This provides quite accurate photometric redshift estimates (see e.g. Negrello et al., 2009). On the other hand, only weak constraints are provided on AGN redshifts, due to their smooth SEDs in this spectral region. But the different spectral shape between starbursts and AGNs allows us to discriminate between these populations.

Figure 5.7 shows the minimum SFR calculated using our line/$L_{\rm IR}$ relations of the sources detectable (in spectroscopy) by the proposed deep survey as a function of the redshift. Also shown, for comparison, are the SFRs associated to the minimum luminosities represented in the IR luminosity functions at several redshifts determined by Gruppioni et al. (2013) on the basis of *Herschel*/PACS and SPIRE surveys. The improvement over *Herschel* is impressive. The deep survey will sample SFRs well below those of the most efficient star formers, estimated to be $\simeq 100\, M_\odot$/yr (Förster Schreiber et al., 2006; Cai et al., 2013). It will therefore allow a full reconstruction of the dust obscured cosmic star formation history up to high redshifts.

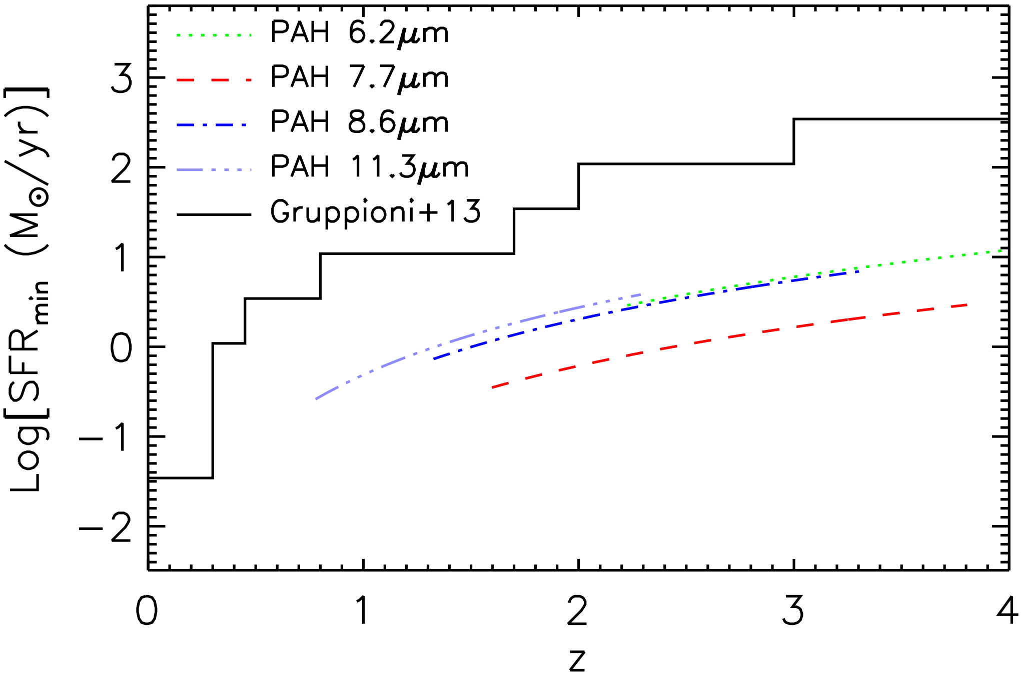

Figure 5.7: Comparison between the minimum SFR achieved by the proposed deep survey with the SMI wide field camera (through spectroscopic detections of PAH lines) and the SFR corresponding to the minimum luminosities represented in the IR luminosity functions determined by Gruppioni et al. (2013) on the basis of *Herschel*/PACS and SPIRE surveys, as a function of the redshift.

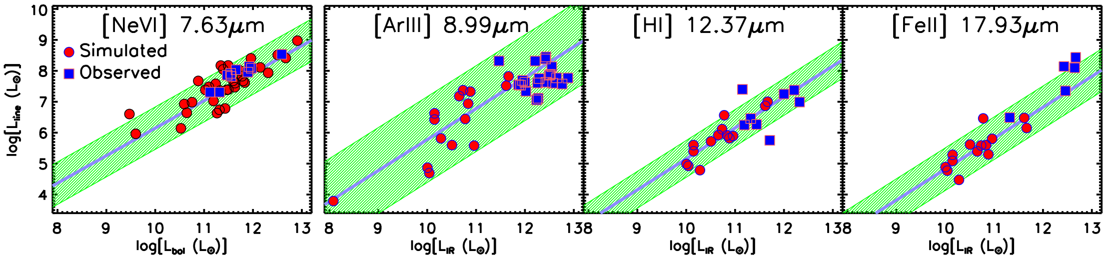

Figure 5.8: Comparison between observed (blue squares) and expected (red circles) line luminosities, obtained using ITERA (see par. 5.2 for details). The [NeVI]7.63 μm data (for AGNs) comes from the Sturm et al. (2002) and Veilleux et al. (2009) catalogues. For the other 3 lines the observed line luminosities (for star-forming galaxies) are from Willett et al. (2011). The green bands show the $\pm 2\,\sigma$ dispersion around the line to continuum luminosity relations derived with ITERA.

Spectral line	$\left\langle \log\left(\frac{L_\ell}{L_{\rm IR}}\right)\right\rangle$	σ
$H_2$5.51μm	-4.29	0.39
PAH6.2μm	-2.20	0.36
$H_2$6.91μm	-3.97	0.39
[ArII]6.98μm	-3.96	0.32
PAH7.7μm	-1.64	0.36
PAH8.6μm	-2.16	0.36
[ArIII]8.99μm	-4.22	0.69
$H_2$9.66μm	-3.96	0.52
[SIV]10.49μm	-3.95	0.69
PAH11.3μm	-2.29	0.36
$H_2$12.28μm	-4.12	0.54
[HI]12.37μm	-4.85	0.30
[NeII]12.81μm	-3.11	0.45
[ClII]14.38μm	-5.44	0.33
[NeIII]15.55μm	-3.69	0.47
$H_2$17.03μm	-4.04	0.46
[FeII]17.93μm	-5.18	0.34
[SIII]18.71μm	-3.49	0.48
[ArIII]21.82μm	-5.40	0.70
[FeIII]22.90μm	-6.56	0.33
[FeII]25.98μm	-4.29	0.44
[SIII]33.48μm	-3.05	0.31
[SiII]34.82μm	-2.91	0.28

Table 5.1: Mean values of the log of line to IR (8-1000 μm) continuum luminosities for star-forming galaxies, $\langle\log(L_\ell/L_{\rm IR})\rangle$, and associated dispersions σ.

Spectral line	a	b	disp (1σ)
[MgVIII]3.03μm	0.73	-1.65	0.60
[CaIV]3.21μm	0.89	-2.90	0.31
[SiIX]3.92μm	0.65	-1.77	0.88
[CaV]4.20μm	0.90	-4.00	0.34
[MgIV]4.49μm	0.89	-3.01	0.32
[ArVI]4.52μm	0.83	-3.36	0.34
$H_2$5.51μm	1.23	-7.01	0.40
[MgV]5.60μm	0.91	-2.94	0.34
[SiVII]6.50μm	0.83	-3.55	0.37
$H_2$6.91μm	0.80	-2.40	0.34
[ArII]6.98μm	0.84	-4.21	0.64
[NeVI]7.63μm	0.79	-1.48	0.42
[ArV]7.90μm	0.87	-3.85	0.32
[ArIII]8.99μm	0.98	-4.15	0.37
$H_2$9.66μm	1.07	-5.32	0.34
[SIV]10.49μm	0.90	-2.96	0.24
[CaV]11.48μm	0.90	-5.12	0.34
$H_2$12.28μm	0.94	-3.88	0.24
[HI]12.37μm	0.86	-3.84	0.34
[NeII]12.81μm	0.98	-4.06	0.37
[ArV]13.09μm	0.87	-3.85	0.32
[MgV]13.50μm	0.91	-4.01	0.34
[NeV]14.32μm	0.78	-1.61	0.39
[ClII]14.38μm	0.85	-4.83	0.57
[NeIII]15.55μm	0.78	-1.44	0.31
$H_2$17.03μm	1.05	-5.10	0.42
[FeII]17.93μm	0.84	-3.80	0.54
[SIII]18.71μm	0.96	-3.75	0.31
[ArIII]21.82μm	0.98	-5.34	0.36
[FeIII]22.90μm	0.79	-4.85	0.60
[NeV]24.31μm	0.69	-0.50	0.39
[OIV]25.89μm	0.70	-0.04	0.42
[FeII]25.98μm	0.87	-3.71	0.55
[SIII]33.48μm	0.62	0.35	0.30
[SiII]34.82μm	0.89	-3.14	0.52

Table 5.2: Coefficients of the best-fit linear relations between line and AGN bolometric luminosities, $\log(L_\ell) = a \cdot \log(L_{\rm bol}) + b$, and 1σ dispersions associated to the relations.

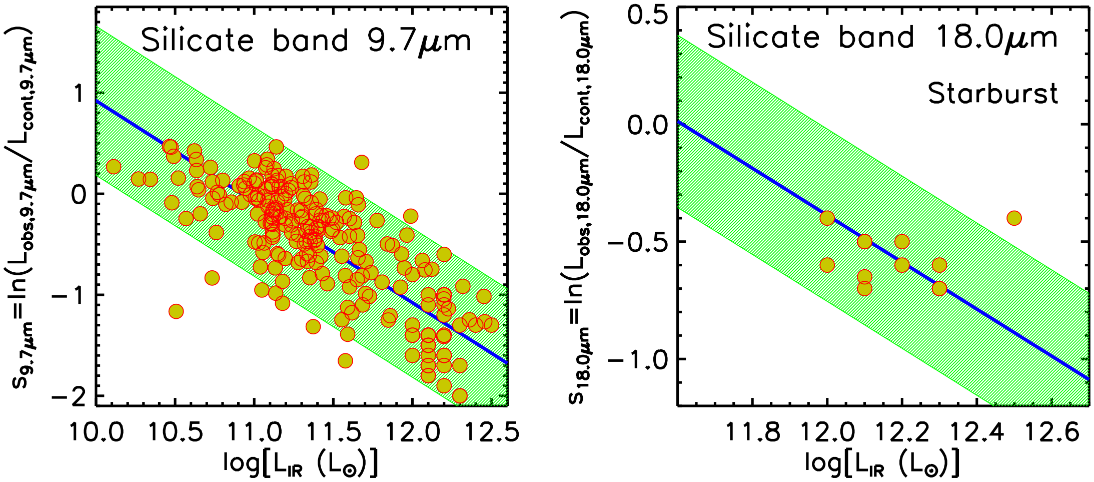

Figure 5.9: Strength of the 9.7 and 18.0 μm silicate bands, as a function of the IR luminosity, for star-forming galaxies. Data from Stierwalt et al. (2013), Imanishi et al. (2007), Imanishi (2009), and Imanishi et al. (2010). The green bands show the $2\,\sigma$ intervals around the mean linear relations $s_\lambda = -\log(L_{\rm IR}) + c$.

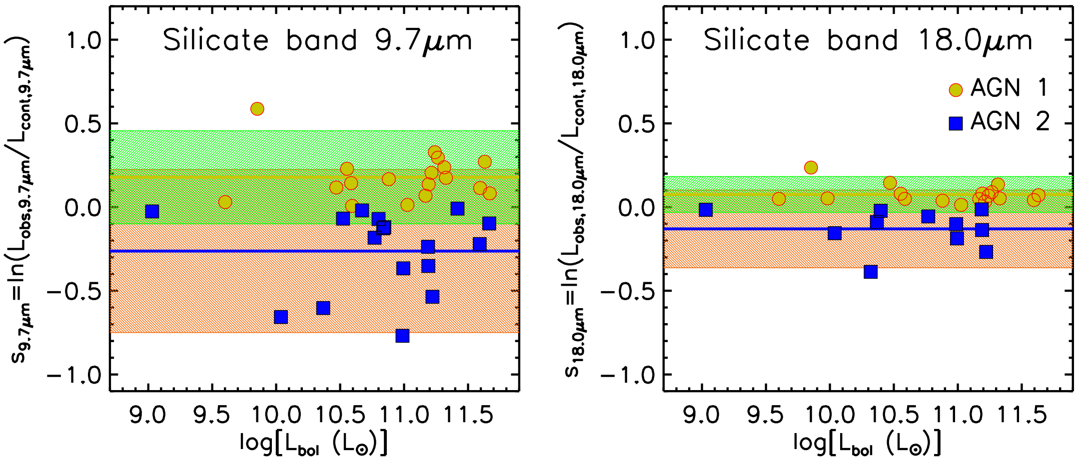

Figure 5.10: Strength of the 9.7 and 18.0 μm silicate bands as a function of the bolometric luminosity for type 1 (circles) and type 2 (squares) AGNs from the Gallimore et al. (2010) sample. The green or orange bands show the $2\,\sigma$ spreads around the mean strength for type 1's (yellow lines) or type 2's (blue lines), respectively.

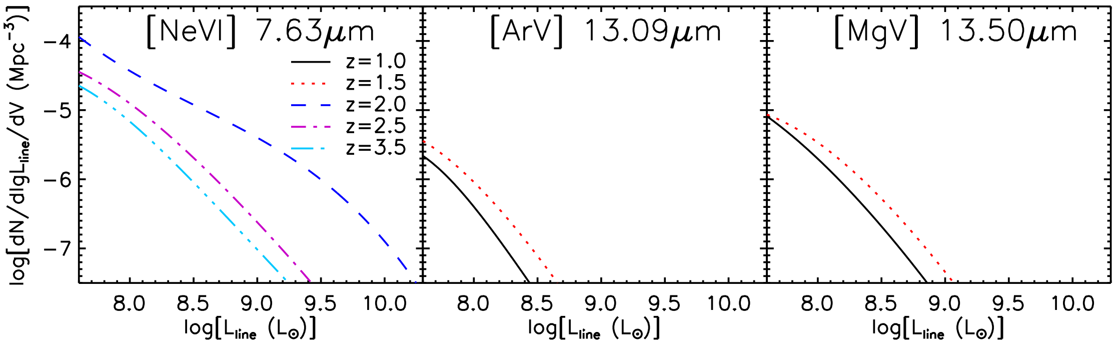

Figure 5.11: Predicted luminosity functions of the AGN lines [NeVI] 7.63, [ArV] 13.09, and [MgV] 13.50 μm at different redshifts at which these lines can be detected by the SMI spectrometers.

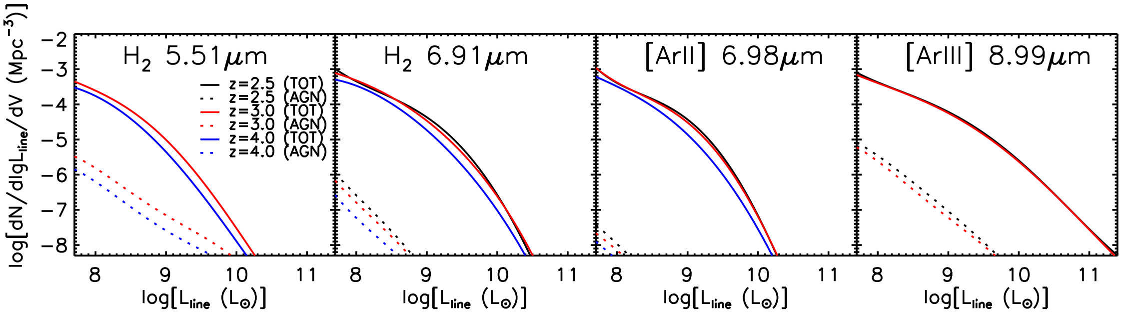

Figure 5.12: Examples of predicted luminosity functions for the total (starburst plus AGN) emission (solid lines) and for the AGN component only (dotted lines) of some lines of my sample, at different redshifts at which these lines can be detected by the SMI spectrometers.

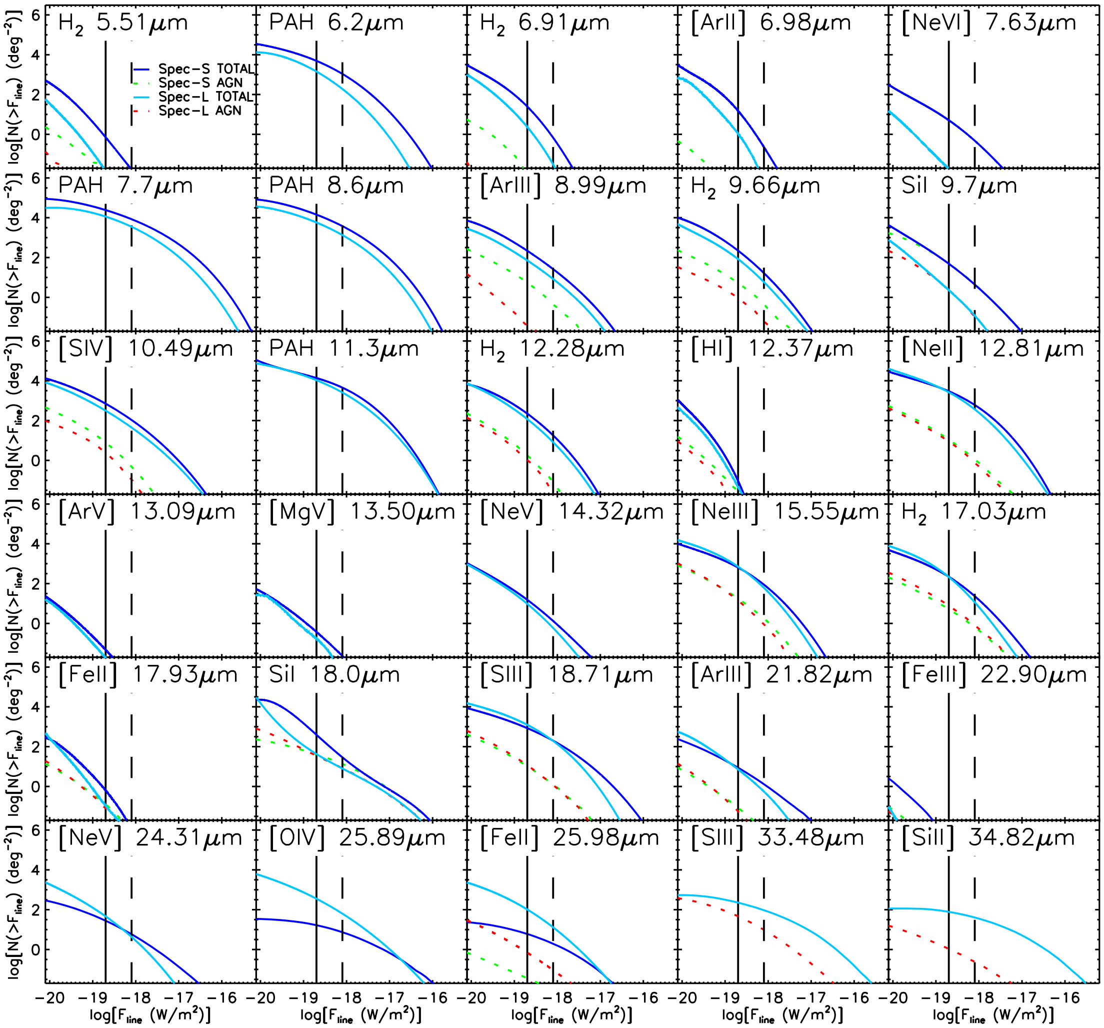

Figure 5.13: Integral counts in 30 MIR lines of galaxies as a whole (starburst plus AGN components; solid blue lines for Spec-S and solid cyan lines for Spec-L) and of AGNs only (dotted green lines for Spec-S and dotted red lines for Spec-L). The vertical lines correspond to the detection limits for 1 h integration/FoV (solid black lines for Spec-S and dashed black lines for Spec-L).

5.2 Line versus IR luminosity

To estimate the counts of galaxy and AGN line detections by SMI surveys I coupled the redshift dependent IR (in the case of galaxies) or bolometric (in the case of AGNs) luminosity functions of the source populations with relationships between line and IR or bolometric luminosities. I have considered the following set of 41 IR lines:

- 3 coronal region lines: [MgVIII]3.03, [SiIX]3.92 and [SiVII]6.50 μm;
- 13 AGN fine-structure emission lines: [CaIV]3.21, [CaV]4.20, [MgIV]4.49, [ArVI]4.52, [MgV]5.60, [NeVI]7.63, [ArV]7.90, [CaV]11.48, [ArV]13.09, [MgV]13.50, [NeV]14.32, [NeV]24.31 and [OIV]25.89 μm;
- 19 fine-structure emission lines that can also be produced in star formation regions:
  - 10 stellar/HII region lines: [ArII]6.98, [ArIII]8.99, [SIV]10.49, [HI]12.37, [NeII]-12.81, [ClII]14.38, [NeIII]15.55, [SIII]18.71, [ArIII]21.82 and [SIII]33.48 μm;
  - 4 lines from photodissociation regions: [FeII]17.93, [FeIII]22.90, [FeII]25.98 and [SiII]34.82 μm;
  - 5 molecular hydrogen lines: H_2 5.51, H_2 6.91, H_2 9.66, H_2 12.28 and H_2 17.03 μm;
- 4 Polycyclic Aromatic Hydrocarbon (PAH) lines at 6.2, 7.7, 8.6 and 11.3 μm;
- the 2 emission and absorption silicate bands at 9.7 and 18.0 μm.

For the PAH 6.2, PAH 7.7, PAH 8.6, PAH 11.3, H_2 9.66, [SIV]10.49, H_2 12.28, [NeII]12.81, [NeV]14.32, [NeIII]15.55, H_2 17.03, [SIII]18.71, [NeV]24.31, [OIV]25.89, [SIII]33.48 and [SiII]34.82 μm lines I have used the relationships derived in chapters 3 and 4 on the basis of observations collected from the literature. The results are summarized in Table 5.1 for star-forming lines and in Table 5.2 for AGN lines.

For all the other lines, with either missing or insufficient data, the line to continuum luminosity relations were derived using ITERA[2] written by Brent Groves. ITERA uses the library of published photoionization and shock models for line emission of astrophysical plasmas produced by the MAPPINGS III code.

Among the options offered by ITERA I have chosen the Dopita et al. (2006) starburst models, the dust free isochoric AGN narrow line region (NLR) models of Groves et al. (2004) for type 1 AGNs, and the dusty radiation-pressure dominated AGN NLR models of Groves et al. (2004) for type 2 AGNs. The chosen models are those which provide the best overall fit (minimum χ^2) to the observed line ratios of local starbursts in the Bernard-Salas et al. (2009) catalogue and of AGNs in the sample built, as discussed in chap. 4, combining sources from the Tommasin et al. (2008, 2010), Sturm et al. (2002), and Veilleux et al. (2009) catalogues.

As an example I compare, in Fig. 5.8, the line luminosities as a function of IR luminosities obtained using ITERA with the observed ones (the majority of which were published after the Groves et al. 2004 and Dopita et al. 2006 models) for [NeVI]7.63, [ArIII]8.99, [HI]12.37 and [FeII]17.93 μm.

The data on starburst galaxies are consistent with a direct proportionality between line and IR luminosity. The mean line to IR luminosity ratios, $\langle\log(L_\ell/L_{\rm IR})\rangle$, and the dispersions, σ, around them are listed in Tab. 5.1. In the case of AGNs the data are described by linear mean relations $\log(L_\ell) = a \cdot \log(L_{\rm bol}) + b$. The coefficients of such relations and the dispersions around them are listed in Tab. 5.2.

For the 9.7 and 18.0 μm silicate bands I have used the observed correlations between the IR luminosity and the relative strength of the features, defined (see, e.g., Spoon et al., 2007) as the natural logarithm of the ratio between the observed flux density at the center

---

[2] http://home.strw.leidenuniv.nl/ brent/itera.html

of the silicate feature, $F_{\mathrm{obs},\lambda_f(1+z)}$, and the local continuum flux density, $F_{\mathrm{cont},\lambda_f(1+z)}$,

$$s_{\lambda_f} = \ln \frac{F_{\mathrm{obs},\lambda_f(1+z)}}{F_{cont,\lambda_f(1+z)}} = \ln \frac{L_{\mathrm{obs},\lambda_f}}{L_{\mathrm{cont},\lambda_f}} \tag{5.1}$$

where λ_f is the rest-frame wavelength of the feature (i.e. 9.7 or 18 μm), while $L_{\mathrm{obs},\lambda_f}$ and $L_{\mathrm{cont},\lambda_f}$ are the corresponding (monochromatic) luminosities at that wavelength.

To calibrate the relationships between the silicate band strength and the IR luminosity for the starburst component I have used data from Stierwalt et al. (2013, only for 9.7μm silicate band), excluding the objects with low 6.2 μm PAH equivalent widths ($\mathrm{EQW}_{6.2\mu\mathrm{m}} <$ 0.27μm) whose MIR emission is likely to be substantially contaminated by an AGN, and the starburst dominated galaxies from Imanishi et al. (2007), Imanishi (2009), and Imanishi et al. (2010) catalogues (these authors actually provide optical depths, $\tau_\lambda = -s_\lambda$).

As illustrated by Fig. 5.9, the 9.7 μm strength of starburst galaxies shows a clear linear correlation with the log of the IR (8-1000μm) luminosity. The very few data on the 18.0 μm strength do not allow me to establish whether it also correlates with L_{IR}. However, in analogy to the 9.7 μm strength, I assume also for the 18.0 μm one a relation of the form $s_\lambda = -\log L_{IR} + c$. Fits of the data yield mean values of c, $\langle c \rangle = 10.92$ for the 9.7μm band and $\langle c \rangle = 11.61$ for the 18.0μm band, with dispersions of 0.37 and of 0.18, respectively.

For AGNs I have used the Gallimore et al. (2010) sample, neglecting the silicate absorption for type 1's and the emission for type 2's. As illustrated by Fig. 5.10 the silicate strengths of AGNs appear to be uncorrelated with the bolometric luminosities. I have therefore adopted Gaussian distributions of s_λ around mean values, $\langle s_\lambda \rangle$, independent of L_{bol}. I have obtained: $\langle s_{9.7\mu\mathrm{m}} \rangle_{\mathrm{AGN\,1}} = 0.18$, $\langle s_{9.7\mu\mathrm{m}} \rangle_{\mathrm{AGN\,2}} = -0.26$, $\langle s_{18.0\mu\mathrm{m}} \rangle_{\mathrm{AGN\,1}} = 0.08$ and $\langle s_{18.0\mu\mathrm{m}} \rangle_{\mathrm{AGN\,2}} = -0.13$ with dispersions of 0.14, 0.24, 0.05, and 0.12, respectively.

The line luminosity functions have been computed starting from the redshift-dependent IR luminosity functions given by the evolutionary model, including both the starburst and the AGN component. To properly take into account the dispersion in the relationships

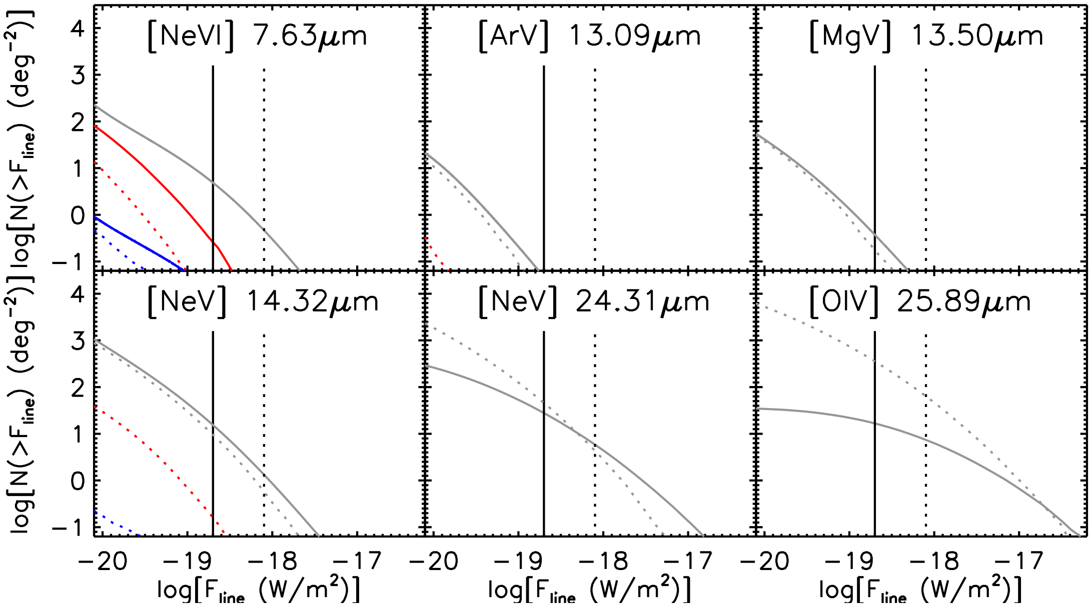

Figure 5.14: Contributions of different AGN populations to the SMI Spec-S (solid lines) and Spec-L (dotted lines) integral counts in 6 AGN lines ([NeVI]7.63, [ArV]13.09, [MgV]-13.50, [NeV]14.32, [NeV]24.31 and [OIV]25.89 μm). Grey lines: AGNs associated to late-type galaxies plus optically selected AGNs; red lines: AGNs associated to unlensed proto-spheroids; blue lines: AGNs associated to strongly gravitationally lensed proto-spheroids. The vertical lines correspond to the detection limits ($2.0 \cdot 10^{-19}$ W/m^2 for Spec-S and $8.0 \cdot 10^{-19}$ W/m^2 for Spec-L) for 1-h exposure per FoV.

between line and continuum luminosities I have used the Monte Carlo approach described in chap. 4. Examples of line luminosity functions at various redshifts are shown in Figs. 5.11 and 5.12.

5.3 Line luminosity functions and number counts

Our predictions for the integral counts in both the Spec-S and the Spec-L channels, for 30 lines are shown in Fig. 5.13. The predicted redshift distributions of sources detected per square degree in a number of lines by the Spec-S and the Spec-L for exposures of 1 h per FoV are presented in Tables 5.3 and 5.4, respectively. In 1 h integration per FoV,

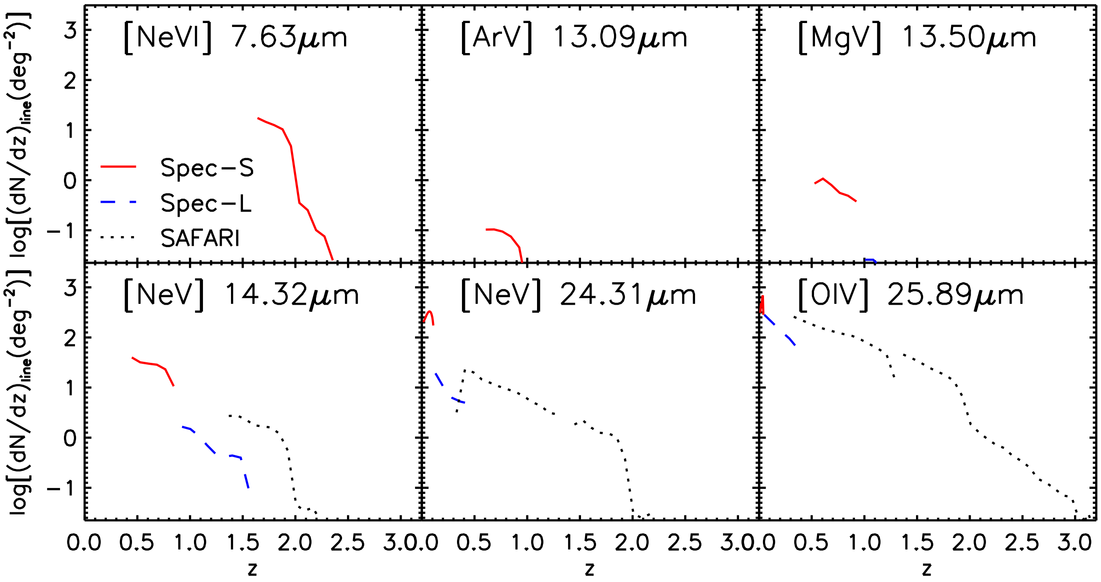

Figure 5.15: Predicted redshift distributions of AGNs detected in 6 lines ([NeVI]7.63, [ArV]-13.09, [MgV]13.50, [NeV]14.32, [NeV]24.31 and [OIV]25.89 μm) detected by SMI Spec-S (solid red lines) and Spec-L (dashed blue lines), compared, for three of them ([NeV]14.32, [NeV]24.31 and [OIV]25.89 μm), with those obtained for SPICA-SAFARI (dotted black lines), for a 1 h exposure per FoV.

the Spec-S will obtain the detection of ~ 70 AGN lines per square degree, primarily of the [NeV]24.31 μm line ($\sim 40\%$ of detections); the Spec-L will detect mostly the [OIV]25.89 μm line (over 90% of the ~ 70 AGN line detections). The $\simeq 140$ lines are produced by $\simeq 110$ individual AGNs.

Figure 5.14 shows the contributions of AGNs associated to different galaxy populations to the SMI Spec-S and Spec-L counts in six AGN lines. The redshift distributions of AGNs detected in each of these lines in 1 h integration/FoV are displayed in Fig. 5.15. For three of the lines ([NeV]14.32, [NeV]24.31 and [OIV]25.89 μm) I also show, for comparison, the redshift distributions obtained for a SPICA-SAFARI survey (again for a 1 h exposure per FoV). The two instruments cover nicely complementary redshift intervals.

Figure 5.16 illustrates the redshift distributions of sources for which the SMI spectrometers will detect at least 1, 2, 3 or 4 lines in 1 h integration per FoV over an area of 1 deg^2. The corresponding numbers of detected lines are about 53,000, 16,000, 3,100, 360, 55 and 8, respectively. Sources detected in at least one line include ~ 200 strongly lensed galaxies at $z > 1$.

Some multiple line detections can be due to different galaxies seen by chance within the same resolution element. We have estimated this confusion effect adopting a typical FWHM of $2''$ and assuming a random galaxy distribution (negligible clustersing effects). The fractions of two line detections due to confusion by the SMI camera and by the SMI spectrometers are shown as a function of the integration time per FoV in Fig. 5.17. The confused fraction is always small (in particular in the SMI spectrometers case). For example, with an integration time of 1 hr two line detections due to confusion are $\simeq 1.5\%$ (for the camera survey) and $\simeq 0.2\%$ (for the spectrometers survey). The number of confusion cases grows almost linearly with the integration time. Therefore the confused fraction grows as we go to fainter fluxes, where the number counts are flatter, but it is still only $\simeq 3.6\%$ (camera) and $\simeq 0.7\%$ (spectrometers) for an integration time of 10 h per FoV.

The difference between the AGN and the galaxy SEDs in the SMI range implies that the equivalent widths (EQWs) of the brightest spectral lines excited by star formation are useful indicators of the AGN contribution. This is illustrated by Fig. 5.18 which shows the variation of the EQWs of the most prominent star formation lines ($\log(\mathrm{EQW}) > -1.5$) with the fractional AGN contribution to the total (starburst plus AGN) L_{IR}(8-1000μm). The PAH lines are particularly effective for this purpose.

The predicted redshift distributions of sources detected per square degree in the four PAH lines by the camera in surveys with the SMI of 1 hr per FoV are presented in Table 5.5. The wide field camera will detect, again in 1 h integration per FoV, $\sim 1.4 \times 10^5$ PAH lines per square degree, produced by $\sim 8.8 \times 10^4$ different star-forming galaxies. Of these about 55,000 (including ~ 390 strongly lensed galaxies) are $z > 1$ proto-spheroids. About 35,000, 13,000 and 320 sources will be detected in at least 2, 3 and 4 PAH lines, respectively.

5.4 Observing strategy

As illustrated by Fig. 5.13, the integral counts for both SMI spectrometers have a slope flatter than 2 at and below the detection limit for 1 h integration/FoV for the majority of the lines. Counts of PAH lines with the SMI camera show a similar behaviour (Fig. 5.5). This means that the number of detections for a fixed observing time generally increases more by extending the survey area than by going deeper, as also found in chapters 3 and 4 for blind spectroscopic surveys with SPICA-SAFARI.

As mentioned in par. 5.3, I expect that a survey of 1 deg^2 with 1 h integration/FoV will detect $\simeq 110$ AGNs. Therefore, to investigate the AGN evolution with sufficient statistics we need a much wider-area.

Also, the blind SMI spectroscopic survey may be usefully complemented by follow-up observations of bright high-z galaxies already discovered at (sub-)mm wavelengths over

Spectral line	0.00 − 0.75	0.75 − 1.25	1.25 − 1.75	1.75 − 2.25	2.25 − 2.75	2.75 − 4.00	4.00 − 6.00	All z
H$_2$5.51μm	0 (0)	0 (0)	0 (0)	0 (0)	2×10^{-1} (5×10^{-2})	2×10^{-1} (4×10^{-2})	0 (0)	4×10^{-1} (1×10^{-1})
PAH6.2μm	0 (0)	0 (0)	0 (0)	157 (0)	2622 (0)	1927 (0)	0 (0)	4706 (0)
H$_2$6.91μm	0 (0)	0 (0)	0 (0)	14 (5×10^{-2})	8 (0)	2 (0)	0 (0)	25 (5×10^{-2})
[ArII]6.98μm	0 (0)	0 (0)	0 (0)	9 (5×10^{-2})	4 (0)	2×10^{-1} (0)	0 (0)	14 (5×10^{-2})
[NeVI]7.63μm	0 (0)	0 (0)	2 (2)	2 (2)	5×10^{-2} (5×10^{-2})	0 (0)	0 (0)	5 (5)
PAH7.7μm	0 (0)	0 (0)	6871 (0)	14292 (0)	4182 (0)	0 (0)	0 (0)	25345 (0)
PAH8.6μm	0 (0)	0 (0)	9953 (0)	4809 (0)	0 (0)	0 (0)	0 (0)	14761 (0)
[ArIII]8.99μm	0 (0)	11 (1×10^{-1})	171 (4)	45 (2)	0 (0)	0 (0)	0 (0)	227 (6)
H$_2$9.66μm	0 (0)	79 (2)	141 (4)	8 (1×10^{-1})	0 (0)	0 (0)	0 (0)	227 (6)
Sil9.7μm	0 (0)	23 (24)	24 (24)	5×10^{-1} (2)	0 (0)	0 (0)	0 (0)	47 (50)
[SIV]10.49μm	0 (0)	435 (5)	280 (2)	0 (0)	0 (0)	0 (0)	0 (0)	716 (7)
PAH11.3μm	0 (0)	9751 (0)	3185 (0)	0 (0)	0 (0)	0 (0)	0 (0)	12936 (0)
H$_2$12.28μm	57 (2×10^{-1})	174 (2)	0 (0)	0 (0)	0 (0)	0 (0)	0 (0)	231 (2)
[HI]12.37μm	1×10^{-1} (5×10^{-2})	1×10^{-1} (4×10^{-2})	0 (0)	0 (0)	0 (0)	0 (0)	0 (0)	3×10^{-1} (1×10^{-1})
[NeII]12.81μm	993 (4)	2011 (6)	0 (0)	0 (0)	0 (0)	0 (0)	0 (0)	3004 (10)
[ArV]13.09μm	6×10^{-2} (6×10^{-2})	6×10^{-2} (6×10^{-2})	0 (0)	0 (0)	0 (0)	0 (0)	0 (0)	1×10^{-1} (1×10^{-1})
[MgV]13.50μm	1×10^{-1} (1×10^{-1})	1×10^{-1} (1×10^{-1})	0 (0)	0 (0)	0 (0)	0 (0)	0 (0)	2×10^{-1} (2×10^{-1})
[NeV]14.32μm	13 (13)	4 (4)	0 (0)	0 (0)	0 (0)	0 (0)	0 (0)	16 (16)
[NeIII]15.55μm	655 (17)	0 (0)	0 (0)	0 (0)	0 (0)	0 (0)	0 (0)	655 (17)
H$_2$17.03μm	222 (5)	0 (0)	0 (0)	0 (0)	0 (0)	0 (0)	0 (0)	222 (5)
[FeII]17.93μm	4×10^{-1} (1×10^{-1})	0 (0)	0 (0)	0 (0)	0 (0)	0 (0)	0 (0)	4×10^{-1} (1×10^{-1})
Sil18.0μm	468 (41)	0 (0)	0 (0)	0 (0)	0 (0)	0 (0)	0 (0)	468 (41)
[SIII]18.71μm	852 (10)	0 (0)	0 (0)	0 (0)	0 (0)	0 (0)	0 (0)	852 (10)
[ArIII]21.82μm	9 (1×10^{-1})	0 (0)	0 (0)	0 (0)	0 (0)	0 (0)	0 (0)	9 (1×10^{-1})
[FeIII]22.90μm	6×10^{-2} (3×10^{-2})	0 (0)	0 (0)	0 (0)	0 (0)	0 (0)	0 (0)	6×10^{-2} (3×10^{-2})
[NeV]24.31μm	28 (28)	0 (0)	0 (0)	0 (0)	0 (0)	0 (0)	0 (0)	28 (28)
[OIV]25.89μm	17 (17)	0 (0)	0 (0)	0 (0)	0 (0)	0 (0)	0 (0)	17 (17)
[FeII]25.98μm	6 (1×10^{-1})	0 (0)	0 (0)	0 (0)	0 (0)	0 (0)	0 (0)	6 (1×10^{-1})

Table 5.3: Predicted redshift distributions of galaxies as a whole (starburst plus AGN components) and, in parenthesis, of AGNs, detectable by a SMI/Spec-S survey covering an area of 1 deg^2 in 1 h integration per FoV. [SIII]33.48μm and [SiII]34.82μm lines are not shown because outside the Spec-S spectral coverage.

much larger areas. Figure 5.19 shows the SMI spectrometer exposure time per FoV needed to achieve a 5σ detection of typical AGN lines at $z = 1$ and $z = 1.5$ as a function of the bolometric luminosity. We can see, for example, that the [NeV]14.32 μm line can be detected in 10 h from an AGN with (real or apparent) bolometric luminosity of $\simeq 10^{13}\,L_\odot$ at $z = 1$ and $\simeq 4 \times 10^{13}\,L_\odot$ at $z = 1.5$. When the SPT and the *Herschel* survey data will be fully available we will have samples of many hundreds of galaxies with either intrinsic or apparent (i.e. boosted by strong gravitational lensing; Negrello et al., 2010, 2014; Vieira et al., 2013) IR luminosities larger than $10^{13}\,L_\odot$. As explained in chap. 4, pointed observations of those sources can allow us to investigate early phases of the galaxy/AGN co-evolution.

Spectral line	0.00 − 0.75	0.75 − 1.25	1.25 − 1.75	1.75 − 2.25	2.25 − 2.75	2.75 − 4.00	4.00 − 6.00	All z
PAH6.2μm	0 (0)	0 (0)	0 (0)	0 (0)	0 (0)	144 (0)	48 (0)	192 (0)
H$_2$6.91μm	0 (0)	0 (0)	0 (0)	0 (0)	0 (0)	6×10^{-2} (0)	0 (0)	6×10^{-2} (0)
[ArII]6.98μm	0 (0)	0 (0)	0 (0)	0 (0)	0 (0)	5×10^{-2} (0)	0 (0)	5×10^{-2} (0)
[NeVI]7.63μm	0 (0)	0 (0)	0 (0)	0 (0)	0 (0)	3×10^{-2} (3×10^{-2})	0 (0)	3×10^{-2} (3×10^{-2})
PAH7.7μm	0 (0)	0 (0)	0 (0)	0 (0)	1050 (0)	2438 (0)	0 (0)	3487 (0)
PAH8.6μm	0 (0)	0 (0)	0 (0)	212 (0)	710 (0)	404 (0)	0 (0)	1325 (0)
[ArIII]8.99μm	0 (0)	0 (0)	0 (0)	4 (0)	4 (5×10^{-2})	2 (0)	0 (0)	10 (5×10^{-2})
H$_2$9.66μm	0 (0)	0 (0)	0 (0)	4 (7×10^{-2})	2 (0)	1×10^{-1} (0)	0 (0)	6 (7×10^{-2})
Sil9.7μm	0 (0)	0 (0)	0 (0)	1×10^{-1} (1×10^{-1})	5×10^{-2} (5×10^{-2})	0 (0)	0 (0)	2×10^{-1} (2×10^{-1})
[SIV]10.49μm	0 (0)	0 (0)	15 (1×10^{-1})	23 (6×10^{-2})	7 (0)	0 (0)	0 (0)	45 (2×10^{-1})
PAH11.3μm	0 (0)	0 (0)	1538 (0)	951 (0)	49 (0)	0 (0)	0 (0)	2538 (0)
H$_2$12.28μm	0 (0)	2×10^{-1} (5×10^{-2})	6 (5×10^{-2})	2 (4×10^{-2})	0 (0)	0 (0)	0 (0)	8 (2×10^{-1})
[NeII]12.81μm	0 (0)	96 (2×10^{-1})	224 (2×10^{-1})	36 (1×10^{-1})	0 (0)	0 (0)	0 (0)	356 (6×10^{-1})
[MgV]13.50μm	0 (0)	5×10^{-2} (5×10^{-2})	0 (0)	0 (0)	0 (0)	0 (0)	0 (0)	5×10^{-2} (5×10^{-2})
[NeV]14.32μm	0 (0)	2×10^{-1} (2×10^{-1})	1×10^{-1} (1×10^{-1})	0 (0)	0 (0)	0 (0)	0 (0)	4×10^{-1} (4×10^{-1})
[NeIII]15.55μm	2 (6×10^{-2})	52 (3×10^{-1})	6 (7×10^{-2})	0 (0)	0 (0)	0 (0)	0 (0)	59 (4×10^{-1})
H$_2$17.03μm	4 (2×10^{-1})	7 (2×10^{-1})	0 (0)	0 (0)	0 (0)	0 (0)	0 (0)	11 (5×10^{-1})
[FeII]17.93μm	5×10^{-2} (5×10^{-2})	0 (0)	0 (0)	0 (0)	0 (0)	0 (0)	0 (0)	5×10^{-2} (5×10^{-2})
Sil18.0μm	8 (8)	3×10^{-1} (3×10^{-1})	0 (0)	0 (0)	0 (0)	0 (0)	0 (0)	8 (8)
[SIII]18.71μm	118 (3×10^{-1})	75 (1×10^{-1})	0 (0)	0 (0)	0 (0)	0 (0)	0 (0)	193 (4×10^{-1})
[ArIII]21.82μm	2×10^{-1} (5×10^{-2})	0 (0)	0 (0)	0 (0)	0 (0)	0 (0)	0 (0)	2×10^{-1} (5×10^{-2})
[NeV]24.31μm	4 (4)	0 (0)	0 (0)	0 (0)	0 (0)	0 (0)	0 (0)	4 (4)
[OIV]25.89μm	64 (64)	0 (0)	0 (0)	0 (0)	0 (0)	0 (0)	0 (0)	64 (64)
[FeII]25.98μm	13 (7×10^{-2})	0 (0)	0 (0)	0 (0)	0 (0)	0 (0)	0 (0)	13 (7×10^{-2})
[SIII]33.48μm	94 (9)	0 (0)	0 (0)	0 (0)	0 (0)	0 (0)	0 (0)	94 (9)
[SiII]34.82μm	40 (2×10^{-1})	0 (0)	0 (0)	0 (0)	0 (0)	0 (0)	0 (0)	40 (2×10^{-1})

Table 5.4: Predicted redshift distributions of galaxies as a whole (starburst plus AGN components) and, in parenthesis, of AGNs, detectable by a SMI/Spec-L survey covering an area of 1 deg^2 in 1 h integration per FoV. H$_2$5.51μm, [HI]12.37μm, [ArV]13.09μm and [FeIII]22.90μm lines are not shown because I don't expect any detection.

Spectral line	0.00 − 0.75	0.75 − 1.25	1.25 − 1.75	1.75 − 2.25	2.25 − 2.75	2.75 − 4.00	4.00 − 6.00	All z
PAH6.2μm	0	0	0	280	4.57×10^{3}	5.45×10^{3}	1.07×10^{3}	1.14×10^{4}
PAH7.7μm	0	0	9.66×10^{3}	2.05×10^{4}	1.10×10^{4}	1.27×10^{4}	0	5.38×10^{4}
PAH8.6μm	0	0	1.54×10^{4}	9.71×10^{3}	4.92×10^{3}	3.54×10^{3}	0	3.36×10^{4}
PAH11.3μm	0	1.47×10^{4}	1.52×10^{4}	7.64×10^{3}	362	0	0	3.79×10^{4}

Table 5.5: Predicted redshift distributions of star-forming galaxies detectable by a survey with the SMI wide field camera covering an area of 1 deg^2 in 1 h integration per FoV.

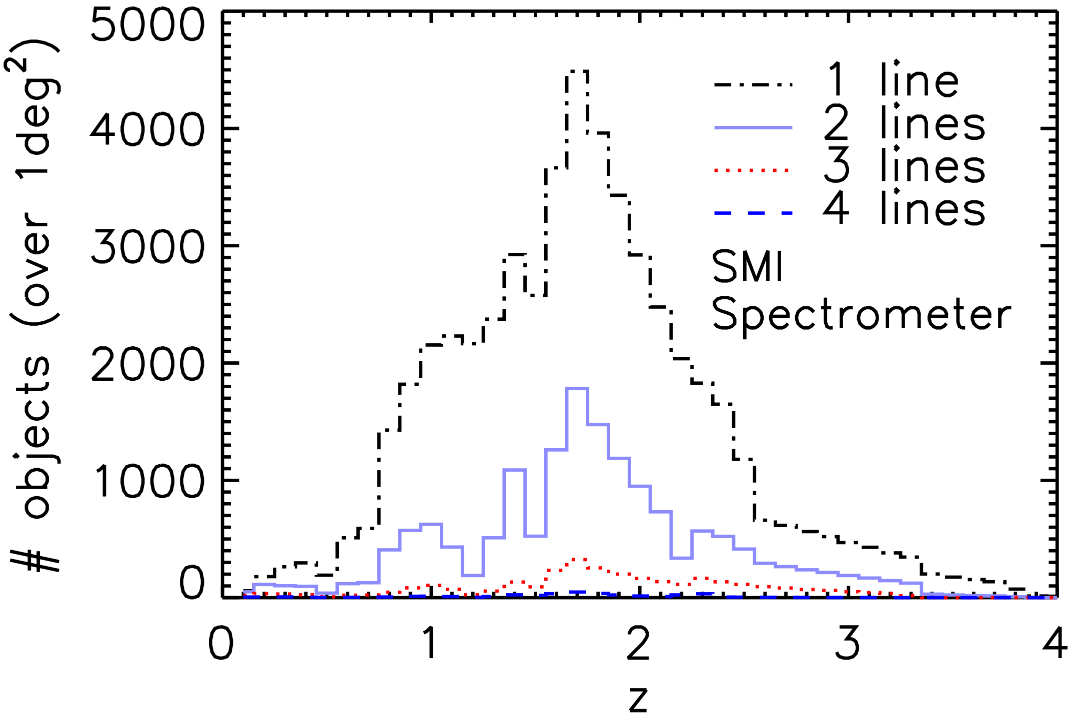

Figure 5.16: Predicted redshift distributions of galaxies (starburst plus AGN components) detectable in one (black histogram), two (cyan), three (red) and four (blue) spectral lines, by a SPICA SMI spectrometer (Spec-S plus Spec-L) survey covering 1 deg^2 in 1 h integration/FoV.

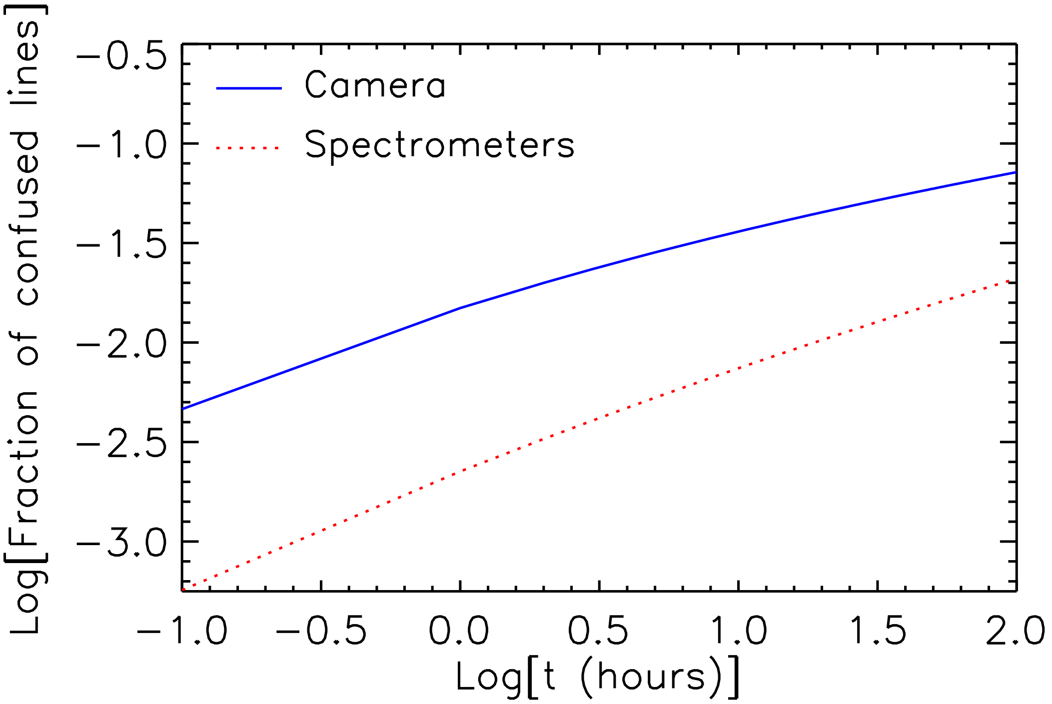

Figure 5.17: Detection of multiple spectral lines produced by galaxies at different redshifts falling within the same resolution element: the fraction of cases of confused lines is shown as a function of the integration time per FoV, for a SMI camera (solid blue line) and for a SMI spectrometers (dotted red line) survey.

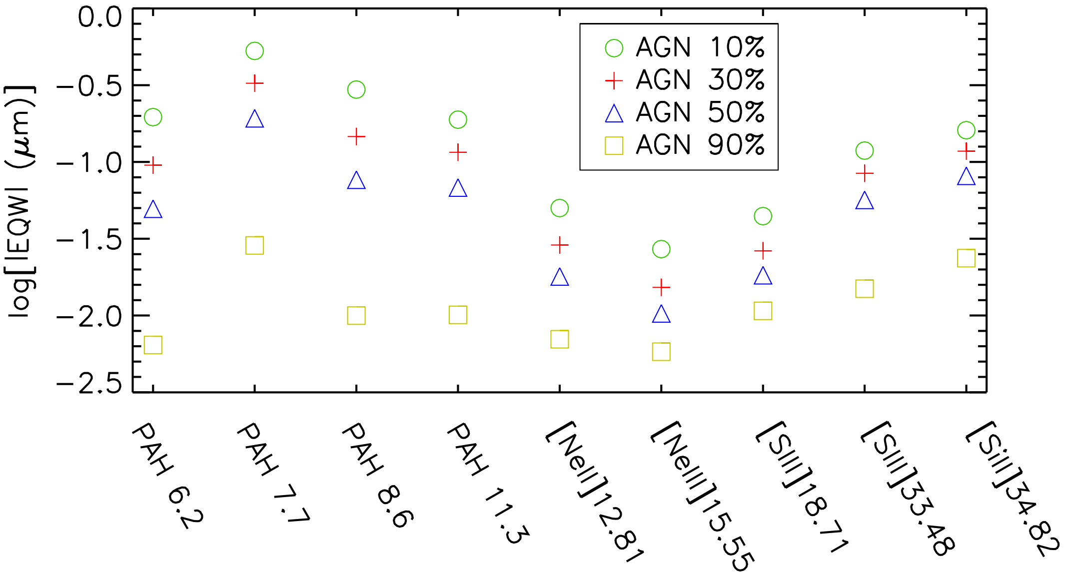

Figure 5.18: Equivalent widths (EQW) of the brightest spectral lines in my sample for a galaxy with a fixed total (star-forming plus AGN) IR luminosity of $10^{13} L_{\odot}$ and varying fractions of AGN IR luminosity.

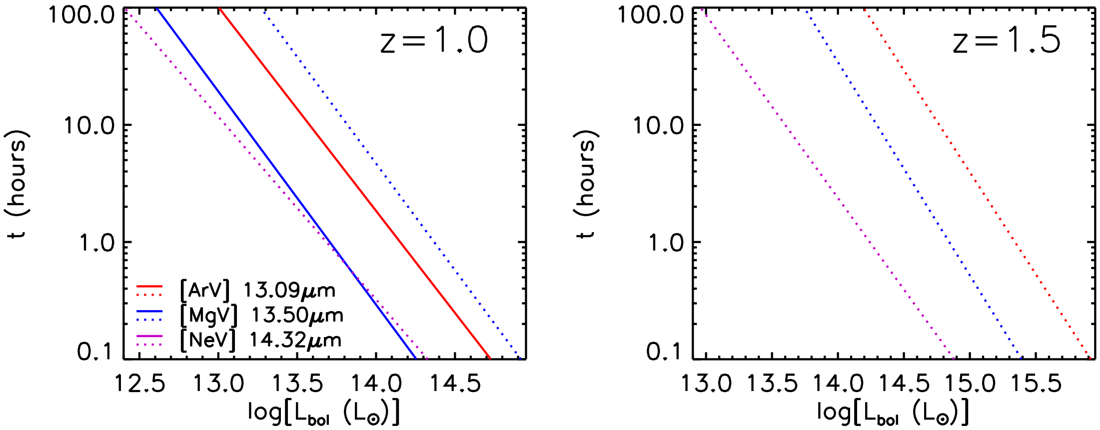

Figure 5.19: SPICA SMI Spec-S (solid lines) and Spec-L (dotted lines) exposure time per FoV required for a 5σ line detection of 3 typical AGN lines ([ArV]13.09, [MgV]13.50 and [NeV]14.32μm) as a function of the AGN bolometric luminosity for $z = 1.0$ (left) and $z = 1.5$ (right).

Spectral line	$t = 10\,\mathrm{h}$ $1.0\,\mathrm{deg}^2$
$H_2$5.51μm	13 (1)
PAH6.2μm	12413 (0)
$H_2$6.91μm	210 (2×10^{-1})
[ArII]6.98μm	167 (1×10^{-1})
[NeVI]7.63μm	23 (23)
PAH7.7μm	45830 (0)
PAH8.6μm	32630 (0)
[ArIII]8.99μm	1004 (27)
$H_2$9.66μm	1240 (25)
Sil9.7μm	395 (375)
[SIV]10.49μm	2510 (46)
PAH11.3μm	27333 (0)
$H_2$12.28μm	1116 (14)
[HI]12.37μm	6 (9×10^{-1})
[NeII]12.81μm	7249 (53)
[ArV]13.09μm	1 (1)
[MgV]13.50μm	3 (3)
[NeV]14.32μm	82 (82)
[NeIII]15.55μm	2084 (84)
$H_2$17.03μm	855 (22)
[FeII]17.93μm	11 (1)
Sil18.0μm	3465 (87)
[SIII]18.71μm	2200 (47)
[ArIII]21.82μm	35 (9×10^{-1})
[FeIII]22.90μm	3×10^{-1} (1×10^{-1})
[NeV]24.31μm	83 (83)
[OIV]25.89μm	34 (34)
[FeII]25.98μm	12 (5×10^{-1})

Table 5.6: Total and AGN (in parenthesis) detections obtainable by SPICA SMI Spec-S survey covering $1.0\,\mathrm{deg}^2$ in 10 h integration/FoV. [SIII]33.48μm and [SiII]34.82μm lines are not shown because outside the Spec-S spectral coverage.

Spectral line	$t = 10\,\mathrm{h}$ $1.0\,\mathrm{deg}^2$
PAH6.2μm	1082 (0)
$H_2$6.91μm	1 (0)
[ArII]6.98μm	9×10^{-1} (0)
[NeVI]7.63μm	8×10^{-2} (8×10^{-2})
PAH7.7μm	9817 (0)
PAH8.6μm	4534 (0)
[ArIII]8.99μm	54 (8×10^{-2})
$H_2$9.66μm	55 (1)
Sil9.7μm	4×10^{-1} (5×10^{-1})
[SIV]10.49μm	236 (2)
PAH11.3μm	8722 (0)
$H_2$12.28μm	79 (1)
[NeII]12.81μm	1934 (6)
[ArV]13.09μm	3×10^{-2} (3×10^{-2})
[MgV]13.50μm	2×10^{-1} (2×10^{-1})
[NeV]14.32μm	7 (7)
[NeIII]15.55μm	501 (9)
$H_2$17.03μm	137 (5)
[FeII]17.93μm	9×10^{-2} (9×10^{-2})
Sil18.0μm	22 (22)
[SIII]18.71μm	990 (8)
[ArIII]21.82μm	5 (1×10^{-1})
[NeV]24.31μm	31 (31)
[OIV]25.89μm	273 (273)
[FeII]25.98μm	76 (9×10^{-1})
[SIII]33.48μm	205 (38)
[SiII]34.82μm	77 (1)

Table 5.7: Total and AGN (in parenthesis) detections obtainable by SPICA SMI Spec-L survey covering $1.0\,\mathrm{deg}^2$ in $10\,\mathrm{h}$ integration/FoV. $H_2$5.51μm, [HI]12.37μm and [FeIII]22.90μm lines are not shown because having null detections at all redshift intervals.

Spectral line	$t = 10\,\mathrm{h}$ $1.0\,\mathrm{deg}^2$
PAH6.2μm	2.66×10^4
PAH7.7μm	8.63×10^4
PAH8.6μm	6.84×10^4
PAH11.3μm	7.98×10^4

Table 5.8: Detections of star-forming galaxies obtainable by SPICA wide field camera survey covering $1.0\,\mathrm{deg}^2$ in $10\,\mathrm{h}$ integration/FoV.

Chapter 6

Conclusions

Our understanding of the cosmological evolution of IR galaxies has dramatically improved in recent years. Observational determinations of their IR luminosity functions up to $z \simeq 4$ are now available. A major step forward will be the characterization of their physical properties, such as the intensity of their interstellar radiation fields, their chemical abundances, the temperatures and densities of their ISM. This will be made possible by the IR spectroscopy provided by forthcoming facilities and in particular by the SAFARI and SMI instruments on SPICA and by CCAT. To optimize the survey strategy and to understand the redshift and galaxy luminosity ranges that can be measured it is necessary to have detailed predictions of the line luminosity functions as a function of redshift and of the corresponding number counts as a function of line flux.

A key ingredient to make such predictions is the relationship between line and total IR luminosity, that will allow us to take advantage of the wealth of information on the evolution of the IR luminosity function. A difficulty in this respect is that reliable measurements of both IR continuum and line luminosities are available for limited and generally heterogeneous samples of galaxies. To account for possible biases in these sample due, e.g., to variable attenuation of the lines by dust, I have carried out extensive simulations exploiting the public library of line luminosities compiled by Panuzzo et al. (2003). This library provides line luminosities for ranges of gas density, gas metallicity and gas filling factor fully adequate to describe the emission properties of the majority of star-forming galaxies. To estimate the distribution of the line-to-IR luminosity ratios I first simulated the spectral SEDs of dust-free star-forming galaxies and then added in a self-consistent way the effect of dust extinction distributed over a realistic range. The results are consistent with line luminosities being proportional to the total IR luminosities. An exception to this proportionality is observationally found in the case of low-z ULIRGs for lines originated outside the stellar birth clouds. In these objects such lines are apparently uncorrelated with $L_{\rm IR}$ and are fainter than expected from the correlation holding for the other sources. In this case, I have adopted a Gaussian distribution of line luminosities around the global mean value.

The distributions of line luminosities have then been exploited to estimate the redshift dependent line luminosity functions starting from the IR continuum luminosity functions. Again, simulations have been made to take fully into account the effect of the dispersions in the line to continuum luminosity ratios. The effect of the dispersion was found to be strong because of the steepness of the bright portion of the IR luminosity function.

In the first part of this work, I have worked out, for SPICA-SAFARI, predictions for the source counts in 14 mid/far-IR emission lines associated to star formation and discussed the expected outcome of a survey covering $0.5\,\rm deg^2$ with a 1 hr integration/FoV. I find that the number of detections in a single line ranges from a few to thousands. In total I expect that more than 21,000 lines will be detected. About 4600, 2800, 1800, 1100 and 700 sources will be detected in at least 2, 3, 4, 5 and 6 lines, respectively. This means that the number of spectroscopically detected individual galaxies is $\simeq 9700$. Sources detected in at least one line include $\simeq 40$ strongly lensed galaxies at $z > 1$.

The slopes of the predicted integral counts below the detection limits of the SPICA-

SAFARI survey (5σ, 1h) are found to be < 2 for most (11 out of 14) of the considered lines. Thus, should more survey time be available, extending the area will produce more detections than going deeper. The SPICA-SAFARI survey covering $0.5\,\mathrm{deg}^2$ with a 1 hr integration/FoV is found to maximize both the number of total detections and of detections at $z > 3$, compared to deeper surveys, at fixed observing time (450 hours).

Follow-up SPICA-SAFARI observations of about 10 h per FoV will detect in two lines essentially all the $z \geq 2$ galaxies discovered by the *Herschel*/PACS and SPIRE surveys used by Gruppioni et al. (2013) to build their redshift-dependent IR luminosity functions. Only a small fraction of these galaxies have spectroscopic redshifts.

I have also presented predictions, for the 7 longer wavelength lines in my set, of the number detections by a CCAT survey of 1000 hours, covering areas ranging from 1 to $1000\,\mathrm{deg}^2$ with exposure times per FoV (assumed to be $1\,\mathrm{deg}^2$) correspondingly ranging from 1 to 1000 h. As in the SPICA-SAFARI case, I find that, at fixed observing time, it is more advantageous to cover larger areas than to go deeper. The number of detected galaxies in a survey of 1000 h with an exposure of 1 h per FoV ranges from some tens to more than ten million. In particular I expect $\simeq 10^7$ detections in the [CII]157.7μm line, including $\simeq 2.4 \times 10^6$ galaxies at $z > 3$ and about 4.9×10^5 unlensed and 1.2×10^4 strongly lensed galaxies at $z > 5$.

A comparison with the predicted numbers of SPICA-SAFARI detections for the survey covering $0.5\,\mathrm{deg}^2$ with a 1 hr integration/FoV worked out by Spinoglio et al. (2012) based on 3 models, substantially different from the one used here, shows that differences are in most cases within a factor of two, although occasionally are much larger. The discrepancies with the Spinoglio et al. (2012) predictions are more substantial in the case of CCAT, except in the case of the [CII]157.7 μm line.

In the second step of this work, I have improved over earlier estimates of redshift-dependent luminosity functions of IR lines detectable by SPICA-SAFARI by building a model that deals in a self consistent way with emission of galaxies as a whole, including both the starburst and the AGN component. For proto-spheroidal galaxies, that dominate the cosmic star formation rate at $z \gtrsim 1.5$, I have derived analytic formulae giving the probability that an object at redshift z has a starburst luminosity L_* or an AGN luminosity $L_\bullet$ given the total luminosity of $L_{\rm tot} = L_* + L_\bullet$. Each proto-spheroid of luminosity $L_{\rm tot}$ was assigned IR luminosities of the starburst and of the AGN component based on the above probability distributions. The association of the AGN component to late-type galaxies was made on the basis of the observed correlation between SFR and accretion rate.

The relationships between line and IR luminosities of the starburst component previously derived have been updated whenever new data have become available in the meantime and additional lines have been taken into account. New relationships between line and AGN bolometric luminosities have been derived.

These ingredients were used to work out predictions for the source counts in 11 mid/far-IR emission lines partially or entirely excited by AGN activity, as well as in the 6.2, 7.7 and 8.6μm PAH lines. The expected outcome of a survey covering $5\,{\rm deg}^2$ with a $1\,{\rm hr}$ integration/FoV is specifically discussed. Taking into account a total of 23 IR lines, I have estimated the number of objects detectable in at least 2, 3, 4, 5 and 6 lines. I estimate that such survey will yield about 760 AGN detections in the [OIV]25.89μm line. A deeper survey ($10\,{\rm hr}$/FoV over $0.5\,{\rm deg}^2$) requiring the same observing time (4500 hours) will yield about ~ 430 detections in the same line.

The AGN contribution to the detectability of galaxies as a whole is minor. I show that this is due to the combination of two factors: the rarity of bright AGNs, due to their short lifetime, and the relatively low (compared to starbursts) line to bolometric luminosity ratios.

Also in this case, I recommend pointed observations of the brightest (either because are endowed with extreme SFRs or because luminosities are strongly magnified by gravitational lensing) galaxies previously detected by large area surveys such as those by *Herschel* and by the SPT. Such observations will allow us to investigate early phases of the galaxy/AGN co-evolution when the black hole mass was much lower than the final one, given by the present day correlation with the stellar mass.

In the third part of this work, I have worked out predictions for surveys with the SPICA-SMI wide field camera and spectrometers.

The combination of a shallow and of a deep survey with the camera, requiring a total observing time of $\simeq 1046\,$h, will allow an accurate definition of MIR source counts of both galaxies and AGNs over about five decades in flux density, down to $\simeq 3.0\,\mu$Jy, i.e. more than one order of magnitude fainter than the deepest *Spitzer* surveys at $24\,\mu$m. This amounts to resolving almost entirely the MIR extragalactic background. The spectral resolution of the camera is optimally suited to detect PAH lines, yielding redshift measurements. The redshift information will allow us to derive the SFR function down to SFRs hundreds of times lower than was possible using *Herschel* surveys and well below the SFRs of typical star-forming galaxies. The cosmic dust obscured star formation history will then be accurately determined at least up to $z \simeq 4$.

On the spectroscopic side I have considered 41 MIR lines, 6 of which are predominantly excited by AGN activity while the others are primarily associated to star formation. Relationships between the line luminosity and the IR (for the starburst component) and/or the bolometric luminosity (for the AGN component) are presented.

Using these relationships I computed the expected number counts for the 30 brightest lines. I found that the SMI spectrometers will detect, with an integration time of 1 h/FoV, about 52,000 galaxies per square degree in at least one line and about 16,000 in at least two lines. About 200 of galaxies detected in at least one line will be strongly lensed.

The number of expected AGN detections is far lower. For the same integration time (1 h/FoV) I expect to detect, per square degree, $\simeq 140$ AGN lines, from $\simeq 110$ AGNs. Thus a larger area is necessary to investigate the AGN evolution with good statistics.

Also in this case, given the low surface density of AGNs detectable by SMI spectrometers, an efficient way to investigate early phases of the galaxy/AGN co-evolution are pointed observations of the brightest galaxies detected by large area surveys such as those by *Herschel* and by the SPT.

Chapter 7

Future perspectives

My analysis, tools and codes, which until now have been mainly focused on IR atomic lines, can be easily extended to atomic and molecular lines at mm and sub-mm wavelengths.

Molecular emission lines are a very useful tool to investigate the chemical, physical and dynamical conditions of the denser gas regions like active star-forming regions typically associated with PDRs, and X-ray dominated region (XDR) associated to AGNs.

In the coming years, large astronomical facilities, such as ALMA, LMT and CCAT, will become fully operational. ALMA is already playing a key role with its unprecedented sensitivity and high angular resolution in the (sub-)mm, as well as LMT, the world's largest and most sensitive single-aperture telescope in its frequency range, whereas the 25-meter telescope CCAT will combine high sensitivity, a wide FoV, and a broad wavelength range to provide an unprecedented capability for deep, large-area, multicolor submillimeter surveys.

Here I present possible applications of my tools to ALMA, but similar implementations can be designed also for the LMT and CCAT.

In the ALMA bands, CO emission is detectable from sources located at various distances across the Universe, with nearly continuous coverage in redshift. In Fig. 7.1 the redshifted frequencies of molecular and atomic lines observable in the ALMA bands are shown. While

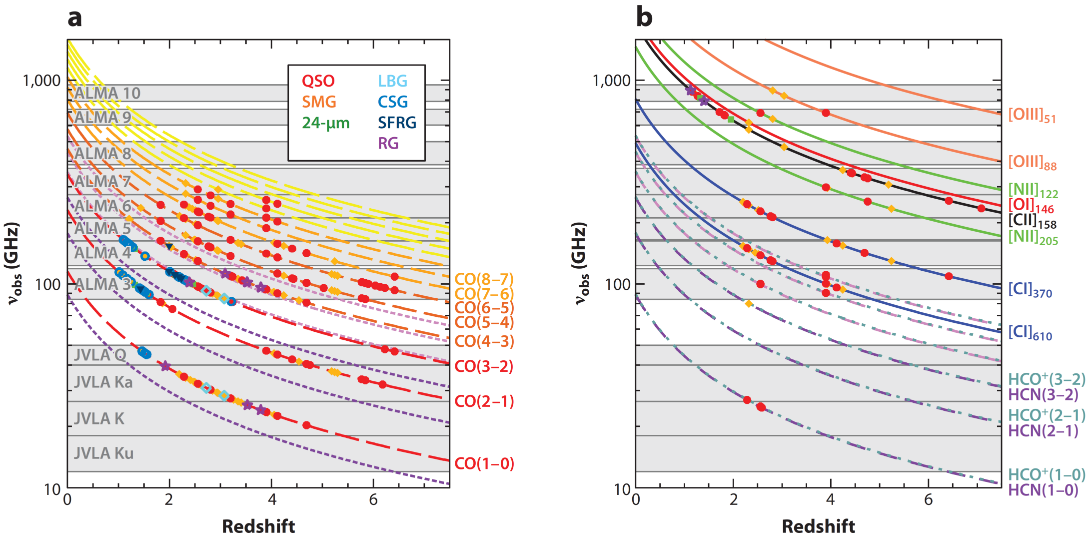

Figure 7.1: Redshifted frequencies of molecular and atomic lines observable in the ALMA bands. The filled circles correspond to lines detected at the time of publication. The color of the points refer to the different source types, as explained in the legend in panel a). Abbreviations: 24-μm, 24-μm galaxy; CSG, color-selected star-forming galaxy; LBG, Lyman-break galaxy; QSO, quasi-stellar object; RG, radio galaxy; SFRG, star-forming radio galaxy; SMG, submillimeter galaxy. (From Carilli & Walter 2013).

the lowest-J CO line is redshifted out of ALMA Band 3 for z>0.37, higher-J rotational CO lines are detectable across a large redshift range. The very high-J rotational CO lines, observed with the *Herschel* satellite in nearby sources, can be detected by ALMA for high-z galaxies. These lines, characterized by high ionization potentials, are useful indicators of nuclear activity in galaxies, as well as being important tools for the study of the physical properties of the molecular gas in these sources.

Molecular gas emission lines in the sub-millimeter and millimeter wavelength ranges are a potentially effective tool for probing the distinction between star-forming galaxies and buried AGN in high-z galaxies, because the effects of dust extinction are so small in these wavelength ranges that signatures of AGNs deeply buried in gas and dust are detectable, while they are typically obscured at shorter wavelength. The observation of high-z galaxies can be eased by gravitational lensing. Negrello et al. (2010) demonstrated that sub-mm flux density selections are efficient to detect lensed galaxies in large area surveys.

As shown in Fig. 7.2, different source populations (starforming versus AGN dominated) have different low-J to high-J CO line luminosities ratios, due to the different excitation mechanisms, and the different conditions of the molecular gas, in particular its temperature and density (Carilli & Walter 2013). For this reason the very high-J rotational CO lines observable with ALMA can be used to identify the presence of low-luminosity, heavily-obscured AGNs in high redshift infrared galaxies.

ALMA (cycle 0 and cycle 1) archive data on high-J rotational CO lines of high-z galaxies can be complemented with measures (when available) on low-J rotational CO lines of the same sources, in order to build their CO SLEDs, from the presence of an AGN can be deduced. When low-J rotational CO lines are not available for a certain source, the same indication can be provided by the ratio between continuum luminosity and high-J CO luminosity, comparing it with calibrations previously obtained empirically (on different local galaxy populations) or theoretically (using the photoionization models already available).

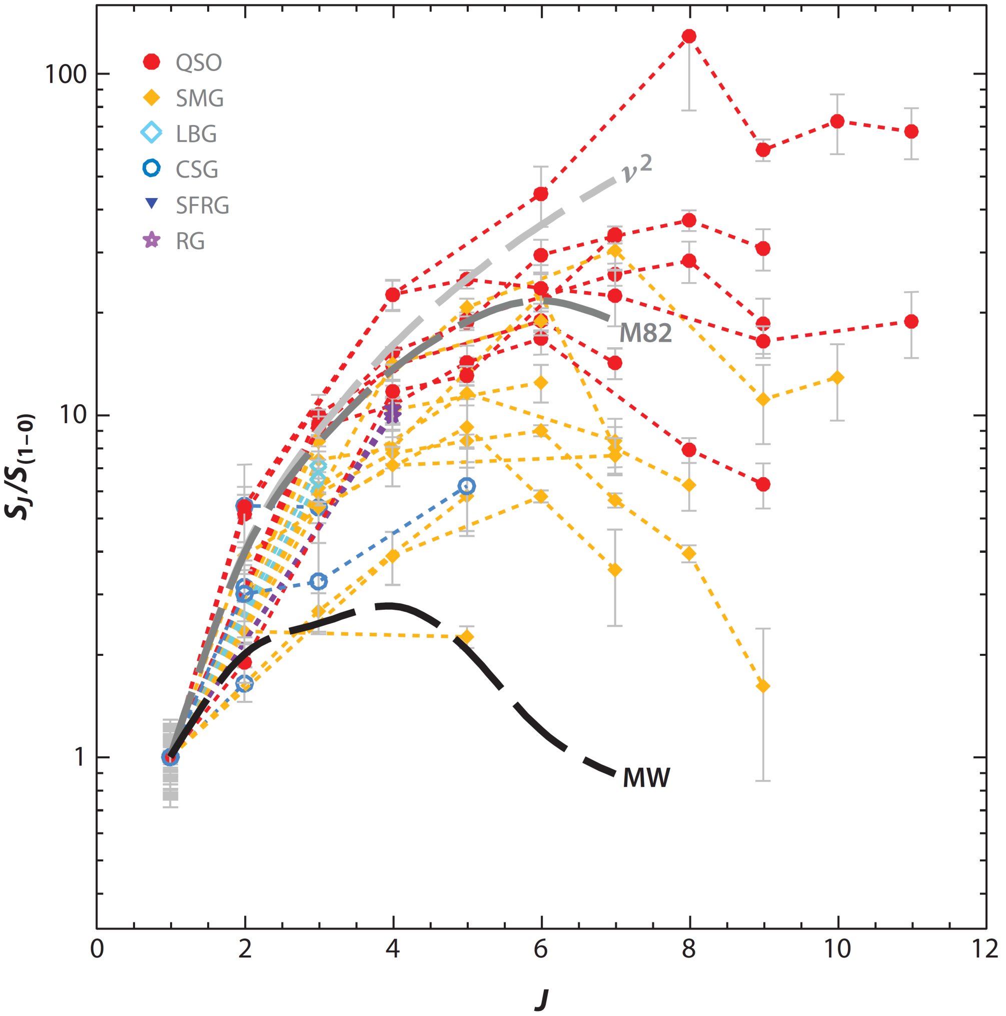

Figure 7.2: CO excitation ladder of sources where the CO(1-0) line has been measured. The CO line flux is shown as a function of rotational quantum number, and the colors indicate the different source types. Measurements for individual sources are connected by a dashed line. The line fluxes have been normalized to the CO(1-0) line. The QSOs are the most excited systems found, with an average peak of the CO ladder at around J∼6. This is consistent with the high star formation rate and compact emission regions in their host galaxies. The SMGs are slightly less excited on average, and their CO excitation ladders peak around J∼5. The dashed thick lines indicate template CO excitation ladders for the Milky Way (MW; black) and M82 (gray). The few multi-transition measurements of CSGs show CO excitation lower than SMGs on average, but higher than the Milky Way. The dashed dark gray line shows constant brightness temperature on the Rayleigh-Jeans scale, i.e., S∼ ν^2 (note that this approximation is not valid for high J). (From Carilli & Walter 2013).

The same objective can be achieved by using, instead of CO lines, other indicators of nuclear activity. Models from Maloney et al. (1996), for example, indicate that HCO+ may be preferentially destroyed in XDRs, while more recent simulations from Meijerink & Spaans (2005) find that the abundance of HNC relative to HCN may increase in the presence of an XDR.

As mentioned previously, *Herschel* surveys have provided samples of hundreds of high-z powerful SMGs, interpreted as massive proto-spheroidal galaxies in the process of forming most of their stellar mass. As explained in par. 2.1, the "OAPD/SISSA" scenario envisages for these sources a well-defined sequence of evolutionary events (that govern the relationship between SF and AGN activities): (1) virialization of DM haloes; (2) vigorous and rapidly dust-enshrouded SF activity, during which a central SMBH grows; (3) QSO phase halting star formation; (4) essentially passive evolution of stellar populations. Comparing the stellar with the halo mass function Lapi et al. (2011) estimated that the active star formation phase lasts for $\sim 0.7\,\mathrm{Gyr}$. In the framework of this scenario, there is only a weak correlation between SFR and accretion rate onto the black hole, and the correlation has a large dispersion, consistent with observational data (Lutz et al. 2010, their Fig.6; Rosario et al. 2013, their Fig.5). However, following the statistical approach described in par. 4.1, for a high-z SMG with a given z and L_{IR}, the model is able to provide a probability distribution of luminosities associated to its central AGN. ALMA observations of high-z SMGs already discovered by *Herschel* can provide evidences of or constraints on the presence of the AGN and so about the precise phase in which these proto-spheroids are.

Using the probability distributions obtained from the model, it is possible to calculate, for ALMA pointed observations of high-z luminous infrared galaxies, the probability of identifying their heavily-obscured AGNs, as a function of the exposure time per FoV, and therefore the depth and the number of observations necessary for the detection of an AGN in its initial phase.

To this end it is necessary to previously estimate relationships between continuum luminosity and the atomic/molecular AGN lines detectable by ALMA.

Regarding ALMA blind spectroscopic surveys, my tools are able to predict, for example, the number of AGN detections in proto-spheroids as a function of areal coverage and integration time per FoV.

Then the comparison between the fraction of the high-z SMGs, observed by ALMA, that show an AGN evidence with those predicted by my probability distributions will constitute a test of the co-evolution of galaxies and AGNs.

Obviously, all the ALMA archive data on molecular and atomic emission measurements, for different redshifts and galaxy populations, can be used to compare the corresponding galaxy counts with those predicted by my reference model, in order to test it by these new observations.

Bibliography

Alexander D. M., Hickox R. C., 2012, NewAR, 56, 93

Amblard A., Cooray A., Serra P., Altieri B., Arumugam V., Aussel H., Blain A., Bock J., Boselli A., Buat V., et al. 2011, Nature, 470, 510

Armus L., Charmandaris V., Bernard-Salas J., Spoon H. W. W., Marshall J. A., Higdon S. J. U., Desai V., Teplitz H. I., Hao L., et al. 2007, ApJ, 656, 148

Baugh C. M., Lacey C. G., Frenk C. S., Granato G. L., Silva L., Bressan A., Benson A. J., Cole S., 2005, MNRAS, 356, 1191

Bernard-Salas J., Spoon H. W. W., Charmandaris V., Lebouteiller V., Farrah D., Devost D., Brandl B. R., Wu Y., Armus L., Hao L., Sloan G. C., Weedman D., Houck J. R., 2009, ApJS, 184, 230

Bernardi M., Shankar F., Hyde J. B., Mei S., Marulli F., Sheth R. K., 2010, MNRAS, 404, 2087

Berta S., Lutz D., Santini P., Wuyts S., Rosario D., Brisbin D., Cooray A., Franceschini A., Gruppioni C., et al. 2013, A&A, 551, A100

Berta S., Magnelli B., Nordon R., Lutz D., Wuyts S., Altieri B., Andreani P., Aussel H., Castañeda H., et al. 2011, A&A, 532, A49

Bertelli G., Bressan A., Chiosi C., Fagotto F., Nasi E., 1994, A&AS, 106, 275

Béthermin M., Dole H., Beelen A., Aussel H., 2010, A&A, 512, A78

Béthermin M., Le Floc'h E., Ilbert O., Conley A., Lagache G., Amblard A., Arumugam V., Aussel H., Berta S., et al. 2012, A&A, 542, A58

Bianchi S., Maiolino R., Risaliti G., 2012, Advances in Astronomy, 2012, 17

Brandl B. R., Bernard-Salas J., Spoon H. W. W., Devost D., Sloan G. C., Guilles S., Wu Y., Houck J. R., Weedman D. W., Armus L., Appleton P. N., Soifer B. T., Charmandaris V., Hao L., Higdon J. A., Marshall S. J., Herter T. L., 2006, ApJ, 653, 1129

Brandl B. R., Snijders L., den Brok M., Whelan D. G., Groves B., van der Werf P., Charmandaris V., Smith J. D., Armus L., Kennicutt Jr. R. C., Houck J. R., 2009, ApJ, 699, 1982

Brauher J. R., Dale D. A., Helou G., 2008, ApJS, 178, 280

Bressan A., Chiosi C., Fagotto F., 1994, ApJS, 94, 63

Brown M. J. I., Brand K., Dey A., Jannuzi B. T., Cool R., Le Floc'h E., Kochanek C. S., Armus L., Bian C., Higdon J., Higdon S., Papovich C., Rieke G., Rieke M., Smith J. D., Soifer B. T., Weedman D., 2006, ApJ, 638, 88

Bruzual G., Charlot S., 2003, MNRAS, 344, 1000

Burgarella D., Buat V., Gruppioni C., Cucciati O., Heinis S., Berta S., Béthermin M., Bock J., Cooray A., et al. 2013, A&A, 554, A70

Cai Z.-Y., Lapi A., Xia J.-Q., De Zotti G., Negrello M., Gruppioni C., Rigby E., Castex G., Delabrouille J., Danese L., 2013, ApJ, 768, 21

Carilli C. L., Walter F., 2013, ARA&A, 51, 105

Carral P., Hollenbach D. J., Lord S. D., Colgan S. W. J., Haas M. R., Rubin R. H., Erickson E. F., 1994, ApJ, 423, 223

Chabrier G., 2003, PASP, 115, 763

Chapman S. C., Blain A. W., Smail I., Ivison R. J., 2005, ApJ, 622, 772

Charlot S., Fall S. M., 2000, ApJ, 539, 718

Chen C.-T. J., Hickox R. C., 2014, in IAU Symposium Vol. 304 of IAU Symposium, A correlation between star formation rate and average black hole accretion rate in star forming galaxies. pp 302–306

Chen C.-T. J., Hickox R. C., Alberts S., Brodwin M., Jones C., Murray S. S., Alexander D. M., Assef R. J., Brown M. J. I., Dey A., Forman W. R., Gorjian V., Goulding A. D., Le Floc'h E., Jannuzi B. T., Mullaney J. R., Pope A., 2013, ApJ, 773, 3

Clements D. L., Bendo G., Pearson C., Khan S. A., Matsuura S., Shirahata M., 2011, MNRAS, 411, 373

Colbert J. W., Malkan M. A., Clegg P. E., Cox P., Fischer J., Lord S. D., Luhman M., Satyapal S., Smith H. A., Spinoglio L., Stacey G., Unger S. J., 1999, ApJ, 511, 721

Cooray A., Amblard A., Wang L., Arumugam V., Auld R., Aussel H., Babbedge T., Blain A., Bock J. e. a., 2010, A&A, 518, L22

Coppin K. E. K., Danielson A. L. R., Geach J. E., Hodge J. A., Swinbank A. M., Wardlow J. L., Bertoldi F., Biggs A., Brandt W. N., et al. 2012, MNRAS, 427, 520

Cormier D., Lebouteiller V., Madden S. C., Abel N., Hony S., Galliano F., Baes M., Barlow M. J., Cooray A., De Looze I., Galametz M., Karczewski O. Ł., Parkin T. J., Rémy A., Sauvage M., Spinoglio L., Wilson C. D., Wu R., 2012, A&A, 548, A20

Cox P., Krips M., Neri R., Omont A., Güsten R., Menten K. M., Wyrowski F., Weiß A., Beelen A., et al. 2011, ApJ, 740, 63

Croom S. M., Richards G. T., Shanks T., Boyle B. J., Strauss M. A., Myers A. D., Nichol R. C., Pimbblet K. A., Ross N. P., Schneider D. P., Sharp R. G., Wake D. A., 2009, MNRAS, 399, 1755

da Cunha E., Charlot S., Elbaz D., 2008, MNRAS, 388, 1595

da Cunha E., Charmandaris V., Díaz-Santos T., Armus L., Marshall J. A., Elbaz D., 2010, A&A, 523, A78

Dasyra K. M., Ho L. C., Armus L., Ogle P., Helou G., Peterson B. M., Lutz D., Netzer H., Sturm E., 2008, ApJ, 674, L9

Dasyra K. M., Ho L. C., Netzer H., Combes F., Trakhtenbrot B., Sturm E., Armus L., Elbaz D., 2011, ApJ, 740, 94

Davé R., Finlator K., Oppenheimer B. D., Fardal M., Katz N., Kereš D., Weinberg D. H., 2010, MNRAS, 404, 1355

De Breuck C., Maiolino R., Caselli P., Coppin K., Hailey-Dunsheath S., Nagao T., 2011, A&A, 530, L8

Delvecchio I., Gruppioni C., Pozzi F., Berta S., Zamorani G., Cimatti A., Lutz D., Scott D., Vignali C., et al. 2014, MNRAS, 439, 2736

Devost D., Brandl B. R., Armus L., Barry D. J., Sloan G. C., Charmandaris V., Spoon H., Bernard-Salas J., Houck J. R., 2004, ApJS, 154, 242

Diamond-Stanic A. M., Rieke G. H., 2012, ApJ, 746, 168

Dopita M. A., Fischera J., Sutherland R. S., Kewley L. J., Leitherer C., Tuffs R. J., Popescu C. C., van Breugel W., Groves B. A., 2006, ApJS, 167, 177

Dudik R. P., Satyapal S., Marcu D., 2009, ApJ, 691, 1501

Elbaz D., Dickinson M., Hwang H. S., Díaz-Santos T., Magdis G., Magnelli B., Le Borgne D., Galliano F., Pannella M., et al. 2011, A&A, 533, A119

Farrah D., Bernard-Salas J., Spoon H. W. W., Soifer B. T., Armus L., Brandl B., Charmandaris V., Desai V., Higdon S., Devost D., Houck J., 2007, ApJ, 667, 149

Ferland G. L., 2001, Hazy, a brief introduction to CLOUDY, University of Kentucky, Department of Physics and Astronomy Internal Report

Ferrarese L., Ford H., 2005, Space Sci. Rev., 116, 523

Fiolet N., Omont A., Lagache G., Bertincourt B., Fadda D., Baker A. J., Beelen A., Berta S., Boulanger F., Farrah D., Kovács A., Lonsdale C., Owen F., Polletta M., Shupe D., Yan L., 2010, A&A, 524, A33

Fischer J., Sturm E., González-Alfonso E., Graciá-Carpio J., Hailey-Dunsheath S., Poglitsch A., Contursi A., Lutz D., Genzel R., Sternberg A., Verma A., Tacconi L., 2010a, A&A, 518, L41

Fischer J., Sturm E., González-Alfonso E., Graciá-Carpio J., Hailey-Dunsheath S., Poglitsch A., Contursi A., Lutz D., Genzel R., Sternberg A., Verma A., Tacconi L., 2010b, A&A, 518, L41

Förster Schreiber N. M., Genzel R., Lehnert M. D., Bouché N., Verma A., Erb D. K., Shapley A. E., Steidel C. C., Davies R., et al. 2006, ApJ, 645, 1062

Franceschini A., Rodighiero G., Vaccari M., Berta S., Marchetti L., Mainetti G., 2010, A&A, 517, A74

Fu H., Cooray A., Feruglio C., Ivison R. J., Riechers D. A., Gurwell M., Bussmann R. S., Harris A. I., Altieri B., et al. 2013, Nature, 498, 338

Galliano F., 2006, ArXiv Astrophysics e-prints

Gallimore J. F., Yzaguirre A., Jakoboski J., Stevenosky M. J., Axon D. J., Baum S. A., Buchanan C. L., Elitzur M., Elvis M., O'Dea C. P., Robinson A., 2010, ApJS, 187, 172

Gandhi P., Horst H., Smette A., Hönig S., Comastri A., Gilli R., Vignali C., Duschl W., 2009, A&A, 502, 457

Genzel R., Lutz D., Sturm E., Egami E., Kunze D., Moorwood A. F. M., Rigopoulou D., Spoon H. W. W., Sternberg A., et al. 1998, ApJ, 498, 579

George R. D., Ivison R. J., Hopwood R., Riechers D. A., Bussmann R. S., Cox P., Dye S., Krips M., Negrello M., et al. 2013a, MNRAS, 436, L99

George R. D., Ivison R. J., Hopwood R., Riechers D. A., Bussmann R. S., Cox P., Dye S., Krips M., Negrello M., et al. 2013b, MNRAS, 436, L99

Gilli R., Comastri A., Hasinger G., 2007, A&A, 463, 79

Glenn J., 2012, http://www.ccatobservatory.org/docs/pdfs/CCAT_Science_Requirements_R1.pdf

Goicoechea J. R., Rodríguez-Fernández N. J., Cernicharo J., 2004, ApJ, 600, 214

González-Nuevo J., Lapi A., Fleuren S., Bressan S., Danese L., De Zotti G., Negrello M., Cai Z.-Y., Fan L., et al. 2012, ApJ, 749, 65

Gorjian V., Werner M. W., Jarrett T. H., Cole D. M., Ressler M. E., 2004, ApJ, 605, 156

Goulding A. D., Alexander D. M., 2009, MNRAS, 398, 1165

Graciá-Carpio J., García-Burillo S., Planesas P., Fuente A., Usero A., 2008, A&A, 479, 703

Graciá-Carpio J., Sturm E., Hailey-Dunsheath S., Fischer J., Contursi A., Poglitsch A., Genzel R., González-Alfonso E., Sternberg A., et al. 2011, ApJ, 728, L7

Granato G. L., De Zotti G., Silva L., Bressan A., Danese L., 2004, ApJ, 600, 580

Greve T. R., Vieira J. D., Weiß A., Aguirre J. E., Aird K. A., Ashby M. L. N., Benson B. A., Bleem L. E., Bradford C. M., et al. 2012, ApJ, 756, 101

Groves B., Dopita M. A., Sutherland R. S., Kewley L. J., Fischera J., Leitherer C., Brandl B., van Breugel W., 2008, ApJS, 176, 438

Groves B. A., Dopita M. A., Sutherland R. S., 2004, ApJS, 153, 75

Gruppioni C., Pozzi F., Rodighiero G., Delvecchio I., Berta S., Pozzetti L., Zamorani G., Andreani P., Cimatti A., et al. 2013, MNRAS, 432, 23

Gruppioni C., Pozzi F., Zamorani G., Vignali C., 2011, MNRAS, 416, 70

Hailey-Dunsheath S., Nikola T., Stacey G. J., Oberst T. E., Parshley S. C., Benford D. J., Staguhn J. G., Tucker C. E., 2010, ApJ, 714, L162

Hao L., Wu Y., Charmandaris V., Spoon H. W. W., Bernard-Salas J., Devost D., Lebouteiller V., Houck J. R., 2009, ApJ, 704, 1159

Hasinger G., 2008, A&A, 490, 905

Hatziminaoglou E., Omont A., Stevens J. A., Amblard A., Arumugam V., Auld R., Aussel H., Babbedge T., Blain A., et al. 2010, A&A, 518, L33

Hickox R. C., Mullaney J. R., Alexander D. M., Chen C.-T. J., Civano F. M., Goulding A. D., Hainline K. N., 2014, ApJ, 782, 9

Higdon S. J. U., Armus L., Higdon J. L., Soifer B. T., Spoon H. W. W., 2006, ApJ, 648, 323

Hill A. R., Gallagher S. C., Deo R. P., Peeters E., Richards G. T., 2014, MNRAS, 438, 2317

Hönig S. F., Kishimoto M., Gandhi P., Smette A., Asmus D., Duschl W., Polletta M., Weigelt G., 2010, A&A, 515, A23

Hyde J. B., Bernardi M., 2009, MNRAS, 394, 1978

Imanishi M., 2009, ApJ, 694, 751

Imanishi M., Dudley C. C., Maiolino R., Maloney P. R., Nakagawa T., Risaliti G., 2007, ApJS, 171, 72

Imanishi M., Maiolino R., Nakagawa T., 2010, ApJ, 709, 801

Ivison R. J., Swinbank A. M., Smail I., Harris A. I., Bussmann R. S., Cooray A., Cox P., Fu H., Kovács A., et al. 2013, ApJ, 772, 137

Ivison R. J., Swinbank A. M., Swinyard B., Smail I., Pearson C. P., Rigopoulou D., Polehampton E., Baluteau J.-P., Barlow M. J., et al. 2010, A&A, 518, L35

Karim A., Swinbank A. M., Hodge J. A., Smail I. R., Walter F., Biggs A. D., Simpson J. M., Danielson A. L. R., Alexander D. M., et al. 2013, MNRAS, 432, 2

Kataza H., Wada T., Sakon I., Kobayashi N., Sarugaku Y., Fujishiro N., Ikeda Y., Oyabu S., 2012, in Society of Photo-Optical Instrumentation Engineers (SPIE) Conference Series Vol. 8442 of Society of Photo-Optical Instrumentation Engineers (SPIE) Conference Series, Mid-infrared camera and spectrometer on board SPICA. p. 0

Kaufman M. J., Wolfire M. G., Hollenbach D. J., Luhman M. L., 1999, ApJ, 527, 795

Kennicutt R. C., Evans N. J., 2012, ARA&A, 50, 531

Kormendy J., Ho L. C., 2013, ARA&A, 51, 511

Lacey C. G., Baugh C. M., Frenk C. S., Benson A. J., Orsi A., Silva L., Granato G. L., Bressan A., 2010, MNRAS, 405, 2

Lapi A., Cavaliere A., 2011, ApJ, 743, 127

Lapi A., González-Nuevo J., Fan L., Bressan A., De Zotti G., Danese L., Negrello M., Dunne L., Eales S., et al. 2011, ApJ, 742, 24

Lapi A., Negrello M., González-Nuevo J., Cai Z.-Y., De Zotti G., Danese L., 2012, ApJ, 755, 46

Lapi A., Raimundo S., Aversa R., Cai Z.-Y., Negrello M., Celotti A., De Zotti G., Danese L., 2014, ApJ, 782, 69

Le Floc'h E., Aussel H., Ilbert O., Riguccini L., Frayer D. T., Salvato M., Arnouts S., Surace J., Feruglio C., et al. 2009, ApJ, 703, 222

Lehmer B. D., Alexander D. M., Bauer F. E., Brandt W. N., Goulding A. D., Jenkins L. P., Ptak A., Roberts T. P., 2010, ApJ, 724, 559

Luhman M. L., Satyapal S., Fischer J., Wolfire M. G., Cox P., Lord S. D., Smith H. A., Stacey G. J., Unger S. J., 1998, ApJ, 504, L11

Luhman M. L., Satyapal S., Fischer J., Wolfire M. G., Sturm E., Dudley C. C., Lutz D., Genzel R., 2003, ApJ, 594, 758

Lutz D., Mainieri V., Rafferty D., Shao L., Hasinger G., Weiß A., Walter F., Smail I., Alexander D. M., et al. 2010, ApJ, 712, 1287

Lutz D., Poglitsch A., Altieri B., Andreani P., Aussel H., Berta S., Bongiovanni A., Brisbin D., Cava A., et al. 2011, A&A, 532, A90

Lutz D., Sturm E., Tacconi L. J., Valiante E., Schweitzer M., Netzer H., Maiolino R., Andreani P., Shemmer O., Veilleux S., 2008, ApJ, 684, 853

Madau P., Dickinson M., 2014, ARA&A, 52, 415

Maddox S. J., Dunne L., Rigby E., Eales S., Cooray A., Scott D., Peacock J. A., Negrello M., Smith D. J. B., et al. 2010, A&A, 518, L11

Maiolino R., Caselli P., Nagao T., Walmsley M., De Breuck C., Meneghetti M., 2009, A&A, 500, L1

Maiolino R., Gallerani S., Neri R., Cicone C., Ferrara A., Genzel R., Lutz D., Sturm E., Tacconi L. J., Walter F., Feruglio C., Fiore F., Piconcelli E., 2012, MNRAS, 425, L66

Maiolino R., Shemmer O., Imanishi M., Netzer H., Oliva E., Lutz D., Sturm E., 2007, A&A, 468, 979

Malhotra S., Kaufman M. J., Hollenbach D., Helou G., Rubin R. H., Brauher J., Dale D., Lu N. Y., Lord S., Stacey G., Contursi A., Hunter D. A., Dinerstein H., 2001, ApJ, 561, 766

Maloney P. R., Hollenbach D. J., Tielens A. G. G. M., 1996, ApJ, 466, 561

Marconi A., Risaliti G., Gilli R., Hunt L. K., Maiolino R., Salvati M., 2004, MNRAS, 351, 169

Meijerink R., Spaans M., 2005, A&A, 436, 397

Meléndez M., Kraemer S. B., Armentrout B. K., Deo R. P., Crenshaw D. M., Schmitt H. R., Mushotzky R. F., Tueller J., Markwardt C. B., Winter L., 2008, ApJ, 682, 94

Merloni A., Bongiorno A., Bolzonella M., Brusa M., Civano F., Comastri A., Elvis M., Fiore F., Gilli R., et al. 2010, ApJ, 708, 137

Mocanu L. M., Crawford T. M., Vieira J. D., Aird K. A., Aravena M., Austermann J. E., Benson B. A., Béthermin M., Bleem L. E., et al. 2013, ApJ, 779, 61

Mullaney J. R., Alexander D. M., Goulding A. D., Hickox R. C., 2011, MNRAS, 414, 1082

Mullaney J. R., Daddi E., Béthermin M., Elbaz D., Juneau S., Pannella M., Sargent M. T., Alexander D. M., Hickox R. C., 2012, ApJ, 753, L30

Negishi T., Onaka T., Chan K.-W., Roellig T. L., 2001, A&A, 375, 566

Negrello M., Hopwood R., De Zotti G., Cooray A., Verma A., Bock J., Frayer D. T., Gurwell M. A., Omont A., et al. 2010, Science, 330, 800

Negrello M., Hopwood R., Dye S., Cunha E. d., Serjeant S., Fritz J., Rowlands K., Fleuren S., Bussmann R. S., et al. 2014, MNRAS, 440, 1999

Negrello M., Perrotta F., González-Nuevo J., Silva L., de Zotti G., Granato G. L., Baccigalupi C., Danese L., 2007, MNRAS, 377, 1557

Negrello M., Serjeant S., Pearson C., Takagi T., Efstathiou A., Goto T., Burgarella D., Jeong W.-S., Im M., et al. 2009, MNRAS, 394, 375

Netzer H., Lutz D., Schweitzer M., Contursi A., Sturm E., Tacconi L. J., Veilleux S., Kim D.-C., Rupke D., Baker A. J., Dasyra K., Mazzarella J., Lord S., 2007, ApJ, 666, 806

O'Dowd M. J., Schiminovich D., Johnson B. D., Treyer M. A., Martin C. D., Wyder T. K., Charlot S., Heckman T. M., Martins L. P., Seibert M., van der Hulst J. M., 2009, ApJ, 705, 885

O'Dowd M. J., Schiminovich D., Johnson B. D., Treyer M. A., Martin C. D., Wyder T. K., Charlot S., Heckman T. M., Martins L. P., Seibert M., van der Hulst J. M., 2011, ApJ, 741, 79

Oliver S. J., Bock J., Altieri B., Amblard A., Arumugam V., Aussel H., Babbedge T., Beelen A., Béthermin M., et al. 2012, MNRAS, 424, 1614

Panuzzo P., Bressan A., Granato G. L., Silva L., Danese L., 2003, A&A, 409, 99

Papovich C., Dole H., Egami E., Le Floc'h E., Pérez-González P. G., Alonso-Herrero A., Bai L., Beichman C. A., Blaylock M., et al. 2004, ApJS, 154, 70

Pereira-Santaella M., Alonso-Herrero A., Rieke G. H., Colina L., Díaz-Santos T., Smith J.-D. T., Pérez-González P. G., Engelbracht C. W., 2010, ApJS, 188, 447

Planck Collaboration Ade P. A. R., Aghanim N., Armitage-Caplan C., Arnaud M., Ashdown M., Atrio-Barandela F., Aumont J., Baccigalupi C., Banday A. J., et al. 2014, A&A, 571, A16

Planck Collaboration Ade P. A. R., Aghanim N., Arnaud M., Ashdown M., Aumont J., Baccigalupi C., Balbi A., Banday A. J., Barreiro R. B., et al. 2011, A&A, 536, A18

Polehampton E. T., Baluteau J.-P., Swinyard B. M., Goicoechea J. R., Brown J. M., White G. J., Cernicharo J., Grundy T. W., 2007, MNRAS, 377, 1122

Polletta M., Tajer M., Maraschi L., Trinchieri G., Lonsdale C. J., Chiappetti L., Andreon S., Pierre M., Le Fèvre O., et al. 2007, ApJ, 663, 81

Pope A., Chary R.-R., Alexander D. M., Armus L., Dickinson M., Elbaz D., Frayer D., Scott D., Teplitz H., 2008, ApJ, 675, 1171

Puget J. L., Leger A., 1989, ARA&A, 27, 161

Renzini A., 2006, ARA&A, 44, 141

Richards G. T., Lacy M., Storrie-Lombardi L. J., Hall P. B., Gallagher S. C., Hines D. C., Fan X., Papovich C., Vanden Berk D. E., Trammell G. B., Schneider D. P., Vestergaard M., York D. G., Jester S., Anderson S. F., Budavári T., Szalay A. S., 2006, ApJS, 166, 470

Riechers D. A., Bradford C. M., Clements D. L., Dowell C. D., Pérez-Fournon I., Ivison R. J., Bridge C., Conley A., Fu H., et al. 2013, Nature, 496, 329

Rodighiero G., Vaccari M., Franceschini A., Tresse L., Le Fevre O., Le Brun V., Mancini C., Matute I., Cimatti A., et al. 2010, A&A, 515, A8

Roelfsema P., Giard M., Najarro F., Wafelbakker K., Jellema W., Jackson B., Swinyard B., Audard M., Doi Y., et al. 2012, in Society of Photo-Optical Instrumentation Engineers (SPIE) Conference Series Vol. 8442 of Society of Photo-Optical Instrumentation Engineers (SPIE) Conference Series, The SAFARI imaging spectrometer for the SPICA space observatory. p. 0

Rosario D. J., Santini P., Lutz D., Netzer H., Bauer F. E., Berta S., Magnelli B., Popesso P., Alexander D. M., et al. 2013, ApJ, 771, 63

Rosario D. J., Santini P., Lutz D., Shao L., Maiolino R., Alexander D. M., Altieri B., Andreani P., Aussel H., et al. 2012, A&A, 545, A45

Rosenthal D., Bertoldi F., Drapatz S., 2000, A&A, 356, 705

Roussel H., Helou G., Smith J. D., Draine B. T., Hollenbach D. J., Moustakas J., Spoon H. W., Kennicutt R. C., Rieke G. H., Walter F., Armus L., Dale D. A., Sheth K., Bendo G. J., Engelbracht C. W., Gordon K. D., Meyer M. J., Regan M. W., Murphy E. J., 2006, ApJ, 646, 841

Rubin R. H., Simpson J. P., Lord S. D., Colgan S. W. J., Erickson E. F., Haas M. R., 1994, ApJ, 420, 772

Sajina A., Yan L., Armus L., Choi P., Fadda D., Helou G., Spoon H., 2007, ApJ, 664, 713

Sanders D. B., Mirabel I. F., 1996, ARA&A, 34, 749

Sani E., Lutz D., Risaliti G., Netzer H., Gallo L. C., Trakhtenbrot B., Sturm E., Boller T., 2010, MNRAS, 403, 1246

Satyapal S., Böker T., Mcalpine W., Gliozzi M., Abel N. P., Heckman T., 2009, ApJ, 704, 439

Satyapal S., Vega D., Dudik R. P., Abel N. P., Heckman T., 2008, ApJ, 677, 926

Saunders W., Rowan-Robinson M., Lawrence A., Efstathiou G., Kaiser N., Ellis R. S., Frenk C. S., 1990, MNRAS, 242, 318

Schweitzer M., Lutz D., Sturm E., Contursi A., Tacconi L. J., Lehnert M. D., Dasyra K. M., Genzel R., Veilleux S., Rupke D., Kim D.-C., Baker A. J., Netzer H., Sternberg A., Mazzarella J., Lord S., 2006, ApJ, 649, 79

Serjeant S., Hatziminaoglou E., 2009, MNRAS, 397, 265

Sheth R. K., Tormen G., 1999, MNRAS, 308, 119

Shi Y., Rieke G. H., Hines D. C., Gorjian V., Werner M. W., Cleary K., Low F. J., Smith P. S., Bouwman J., 2006, ApJ, 653, 127

Shupe D. L., Rowan-Robinson M., Lonsdale C. J., Masci F., Evans T., Fang F., Oliver S., Vaccari M., Rodighiero G., et al. 2008, AJ, 135, 1050

Silva L., Granato G. L., Bressan A., Danese L., 1998, ApJ, 509, 103

Simpson C., 2005, MNRAS, 360, 565

Smith J. D. T., Draine B. T., Dale D. A., Moustakas J., Kennicutt Jr. R. C., Helou G., Armus L., Roussel H., Sheth K., et al. 2007, ApJ, 656, 770

Spinoglio L., Dasyra K. M., Franceschini A., Gruppioni C., Valiante E., Isaak K., 2012, ApJ, 745, 171

Spinoglio L., Dasyra K. M., Franceschini A., Gruppioni C., Valiante E., Isaak K., 2014, ApJ, 791, 138

Spinoglio L., Malkan M. A., 1992, ApJ, 399, 504

Spinoglio L., Malkan M. A., Smith H. A., Fischer J., 2003, in Collin S., Combes F., Shlosman I., eds, Active Galactic Nuclei: From Central Engine to Host Galaxy Vol. 290 of Astronomical Society of the Pacific Conference Series, Mid- and far-infrared spectroscopy of Seyfert galaxies. p. 557

Spoon H. W. W., Marshall J. A., Houck J. R., Elitzur M., Hao L., Armus L., Brandl B. R., Charmandaris V., 2007, ApJ, 654, L49

Stacey G. J., Hailey-Dunsheath S., Ferkinhoff C., Nikola T., Parshley S. C., Benford D. J., Staguhn J. G., Fiolet N., 2010, ApJ, 724, 957

Stierwalt S., Armus L., Surace J. A., Inami H., Petric A. O., Diaz-Santos T., Haan S., Charmandaris V., Howell J., et al. 2013, ApJS, 206, 1

Sturm E., Lutz D., Verma A., Netzer H., Sternberg A., Moorwood A. F. M., Oliva E., Genzel R., 2002, A&A, 393, 821

Sturm E., Verma A., Graciá-Carpio J., Hailey-Dunsheath S., Contursi A., Fischer J., González-Alfonso E., Poglitsch A., et al. 2010, A&A, 518, L36

Swinbank A. M., Karim A., Smail I., Hodge J., Walter F., Bertoldi F., Biggs A. D., de Breuck C., Chapman S. C., et al. 2012, MNRAS, 427, 1066

Symeonidis M., Georgakakis A., Seymour N., Auld R., Bock J., Brisbin D., Buat V., Burgarella D., Chanial P., et al. 2011, MNRAS, 417, 2239

Takagi T., Matsuhara H., Goto T., Hanami H., Im M., Imai K., Ishigaki T., Lee H. M., Lee M. G., Malkan M., Ohyama Y., Oyabu S., Pearson C. P., Serjeant S., Wada T., White G. J., 2012, A&A, 537, A24

Thornley M. D., Schreiber N. M. F., Lutz D., Genzel R., Spoon H. W. W., Kunze D., Sternberg A., 2000, ApJ, 539, 641

Tielens A. G. G. M., 2008, ARA&A, 46, 289

Tommasin S., Spinoglio L., Malkan M. A., Fazio G., 2010, ApJ, 709, 1257

Tommasin S., Spinoglio L., Malkan M. A., Smith H., González-Alfonso E., Charmandaris V., 2008, ApJ, 676, 836

Treister E., Urry C. M., Van Duyne J., Dickinson M., Chary R.-R., Alexander D. M., Bauer F., Natarajan P., Lira P., Grogin N. A., 2006, ApJ, 640, 603

Unger S. J., Clegg P. E., Stacey G. J., Cox P., Fischer J., Greenhouse M., Lord S. D., Luhman M. L., Satyapal S., Smith H. A., Spinoglio L., Wolfire M., 2000, A&A, 355, 885

Valiante E., Lutz D., Sturm E., Genzel R., Chapin E. L., 2009, ApJ, 701, 1814

Vega O., Clemens M. S., Bressan A., Granato G. L., Silva L., Panuzzo P., 2008, A&A, 484, 631

Veilleux S., Rupke D. S. N., Kim D.-C., Genzel R., Sturm E., Lutz D., Contursi A., Schweitzer M., Tacconi L. J., Netzer H., Sternberg A., Mihos J. C., Baker A. J., Mazzarella J. M., Lord S., Sanders D. B., Stockton A., Joseph R. D., Barnes J. E., 2009, ApJS, 182, 628

Vieira J. D., Crawford T. M., Switzer E. R., Ade P. A. R., Aird K. A., Ashby M. L. N., Benson B. A., Bleem L. E., Brodwin M., et al. 2010, ApJ, 719, 763

Vieira J. D., Marrone D. P., Chapman S. C., De Breuck C., Hezaveh Y. D., Weiβ A., Aguirre J. E., Aird K. A., Aravena M., et al. 2013, Nature, 495, 344

Viero M. P., Wang L., Zemcov M., Addison G., Amblard A., Arumugam V., Aussel H., Béthermin M., Bock J., et al. 2013, ApJ, 772, 77

Wagg J., Carilli C. L., Wilner D. J., Cox P., De Breuck C., Menten K., Riechers D. A., Walter F., 2010, A&A, 519, L1

Walter F., Decarli R., Carilli C., Bertoldi F., Cox P., da Cunha E., Daddi E., Dickinson M., Downes D., et al. 2012, Nature, 486, 233

Wang J., Navarro J. F., Frenk C. S., White S. D. M., Springel V., Jenkins A., Helmi A., Ludlow A., Vogelsberger M., 2011, MNRAS, 413, 1373

Wardlow J. L., Cooray A., De Bernardis F., Amblard A., Arumugam V., Aussel H., Baker A. J., Béthermin M., et al. 2013, ApJ, 762, 59

Weaver K. A., Meléndez M., Mushotzky R. F., Kraemer S., Engle K., Malumuth E., Tueller J., Markwardt C., Berghea C. T., Dudik R. P., Winter L. M., Armus L., 2010, ApJ, 716, 1151

Weiß A., De Breuck C., Marrone D. P., Vieira J. D., Aguirre J. E., Aird K. A., Aravena M., Ashby M. L. N., Bayliss M., et al. 2013, ApJ, 767, 88

Weiß A., Kovács A., Coppin K., Greve T. R., Walter F., Smail I., Dunlop J. S., Knudsen K. K., Alexander D. M., et al. 2009, ApJ, 707, 1201

Willett K. W., Darling J., Spoon H. W. W., Charmandaris V., Armus L., 2011, ApJS, 193, 18

Woody D., Padin S., Chauvin E., Clavel B., Cortes G., Kissil A., Lou J., Rasmussen P., Redding D., Zolwoker J., 2012, in Society of Photo-Optical Instrumentation Engineers (SPIE) Conference Series Vol. 8444 of Society of Photo-Optical Instrumentation Engineers (SPIE) Conference Series, The CCAT 25m diameter submillimeter-wave telescope. p. 2

Wu Y., Helou G., Armus L., Cormier D., Shi Y., Dale D., Dasyra K., Smith J. D., Papovich C., et al. 2010, ApJ, 723, 895

Xia J.-Q., Negrello M., Lapi A., De Zotti G., Danese L., Viel M., 2012, MNRAS, 422, 1324

Yan L., Chary R., Armus L., Teplitz H., Helou G., Frayer D., Fadda D., Surace J., Choi P., 2005, ApJ, 628, 604

Yan L., Sajina A., Fadda D., Choi P., Armus L., Helou G., Teplitz H., Frayer D., Surace J., 2007, ApJ, 658, 778

Yun M. S., Scott K. S., Guo Y., Aretxaga I., Giavalisco M., Austermann J. E., Capak P., Chen Y., Ezawa H., et al. 2012, MNRAS, 420, 957

Zhao D. H., Jing Y. P., Mo H. J., Börner G., 2003, ApJ, 597, L9

Ringraziamenti

Sono molte le persone che devo ringraziare per aver raggiunto questo traguardo.

Iniziando dal mondo accademico, ringrazio innanzitutto il Prof. De Zotti e Mattia, perchè tutto quello che ho imparato in questi anni di Dottorato l'ho imparato da loro. Ho avuto la fortuna di poter stare nel loro ufficio per più di due anni e questo mi ha permesso di arricchirmi molto, non solo dal punto di vista scientifico. Ringrazio il Prof. per la disponibilità e la generosità che mi ha dimostrato nel trasmettermi il suo sapere. L'onestà, la correttezza e l'efficienza con cui lavora sono per me un esempio dell'uomo di scienza che vorrei un giorno essere. Ringrazio Mattia per la sua gentilezza, la sua pazienza e la sua simpatia.

Ringrazio il Prof. Secco, mio maestro di vita ed amico. Il suo sostegno non mi è mai mancato. Ho avuto il privilegio di conoscerlo e di imparare molto da lui, dalla sua coerenza e dagli altri valori umani di cui è ricco.

Ringrazio il Prof. Zampieri, la Prof.ssa Marigo, il Prof. Rafanelli ed Anna Sponselli, che mi hanno aiutato e protetto quando una tempesta cieca e irrazionale si era abbattuta su di me.

Ringrazio il Prof. Bressan e tutti i coautori dei miei articoli, con i quali ho mosso i primi passi nel mondo della ricerca.

Ma anche al di fuori del mondo accademico sono tante le persone a cui voglio dire il mio grazie.

Ringrazio particolarmente Giusy, per il suo amore, il suo sostegno, il suo aiuto, la sua fiducia, che non sono mai mancati: è soprattutto grazie a lei se sono riuscito a raggiungere questo successo. Ringrazio la mia piccola cucciola Aurora, che, quando sono al lavoro non vedo di tornare a casa per riabbracciare.

Un grazie speciale ai miei genitori, per il loro amore e il loro esempio: è grazie a loro se sono diventato l'uomo che sono. Ringrazio mia sorella e il mio nipotino Mattia per il loro affetto.

Ringrazio tutti i miei amici, che hanno reso la mia vita molto più piacevole: il Grande Fabius (fratè), Sergione, Carmine, Luca Arcangels, il Checco, Marco Parmisan, Luca Santorum, il Savio, Danilo, Sulliman, il Pego, il Lorentz, Diego, Ivano, Pietro... Ringrazio i colleghi e amici "affamati", i compagni de ilmeteo.it, la squadra di calcio più scarsa e litigiosa del mondo, i miei suoceri (non solo per i pranzi che mi hanno generosamente preparato).

Ringrazio Don Giuseppe e Don Alberto, miei modelli luminosi, per avermi guidato in questi anni, con grande saggezza e affetto, e ringrazio tutti gli amici della scuola SISRI e del centro DISF.

Grazie di cuore a tutti!